

Diplomarbeit

Establishing Microscopic Assays for Long-Term Live-Cell Imaging of Growth and Proliferation Processes in Cell Populations

eingereicht von

FELIX DANIEL KARSTEN

Geburtstag: 10.09.1986

zur Erlangung des akademischen Grades

***Doktor der gesamten Heilkunde
(Dr.med.univ.)***

an der

Medizinischen Universität Graz

ausgeführt am

Institut für Molekularbiologie und Biochemie

unter Anleitung von

Assoz. Prof. Dr. ROLAND MALLI & Univ. Prof. Dr. WOLFGANG GRAIER

Graz, December 19, 2013

FELIX KARSTEN

Eidesstattliche Erklärung

Ich erkläre ehrenwörtlich, dass ich die vorliegende Arbeit selbstständig und ohne fremde Hilfe verfasst habe, andere als die angegebenen Quellen nicht verwendet habe und die den benutzten Quellen wörtlich oder inhaltlich entnommenen Stellen als solche kenntlich gemacht habe.

Graz, am December 19, 2013

FELIX DANIEL KARSTEN

Acknowledgments

First of all, I would like to thank all my current and former lab members for such a great atmosphere and all the useful advices and thrilling discussions during the last two and a half years! This is one of the main reasons why I like to remain in science for the next couple of years.

Thank you, Roland, Jadoon, Rizzi, Neel, Claire, Lukas, Andras, Sandra, Markus, Sasha, Rene, Corina, Nici, Sonja, Christiane, Warisara, Therese, Andreas, Jan, Michi.

For their help and organization of the cell culture I would like to thank Dr. Rene Rost, Therese Macher, and Florian Enzinger.

Of course, my special appreciation belongs to my supervisors, Prof. Roland Malli and Prof. Wolfgang F. Graier for giving me the opportunity to work independently on sophisticated devices and to prepare my own experiments without much scientific background in the beginning, while still supporting me when I asked for help and advices.

I highly acknowledge the opportunity to use the Cell-IQ system. Prof. Berthold Huppertz and Monika Siwetz from the Institute of Cell Biology, Histology, and Embryology for the availability of their Cell-IQ, and Werner Bürgler (HVD Life Sciences) for the loan unit of the Cell-IQ and his help during my first attempts of analysis.

Last but not least, I would like to express my gratitude to my family for all their love and support during my whole life, and in recent years to my girlfriend!

Contents

Eidesstattliche Erklärung	I
Acknowledgments	II
Table of Contents	II
Abbreviations	VII
List of Figures	XI
List of Tables	XIII
Zusammenfassung	XIV
Abstract	XV
I. Introduction	1
1 Live Cell Imaging	1
1.1 Phase Contrast Microscopy	1
1.2 Combination with an Incubator	2
1.3 Fluorescence Microscopy	3
1.3.1 Confocal Microscopy	4
1.3.2 Super-Resolution Imaging	5
1.3.3 Resonance Energy Transfer Microscopy	6
2 Aims of this Diploma Thesis	8
II. Material and Methods	9
1 Materials	9
1.1 Chemicals	9
1.2 Plates and Dishes	9
1.3 Cell Culture Media and Buffers	9
2 Cell Culture	11
3 Loading Cells with Chemicals	12
4 Transfection	12
4.1 Overexpression	12
4.2 RNA interference	13
5 Cell Viability Assay	13
5.1 MTT	13
5.2 Morphological Analysis	14
6 Microscopy	14
6.1 Microscopes	14
6.2 Time-lapse Imaging	15
6.3 Intracellular Ca ²⁺ and ATP measurements	15

7	Image Analysis	16
8	Data and Statistical Analyses	16
III. Results		17
1	Establishment of Life-Cell Imaging Assays	17
1.1	Confluency	17
1.1.1	Correlation between Endothelial Cell Confluency and Cell Number	18
1.1.2	ATP Sensor-Transfected HeLa Cells Proliferate Slower than Ca ²⁺ Sensor-Transfected HeLa Cells	19
1.2	Proliferation	20
1.3	Division	20
1.4	Cell Death and Viability	21
1.5	Migration	22
1.6	Caveats	25
1.6.1	Contamination	25
1.6.2	Various pH Buffers do not Influence Cell Proliferation	26
1.6.3	Choice of Cell Culture Dishes or Plates	27
1.6.4	Intense Light Reduces Endothelial Cell Migration	28
1.7	Establishment of Analysis Techniques	30
1.7.1	Morphology Analysis	30
1.7.2	Intensity Analysis	33
1.7.3	Conclusion	35
1.7.4	Migration Analysis	37
1.7.5	Estimated Pace of Migration Depends on Applied Analysis	39
2	Morphological Peculiarities	41
2.1	Multi-Nucleated Cells and Merging Cells	41
2.2	Atypical Cell Divisions	42
2.3	Vacuoles Occur Transiently upon Treatment with the PI3K In- hibitor Wortmannin after 15 Minutes	43
2.4	Crateagus Extract WS-1442 induces Strong, Light-Intensity-Dependent Phototoxicity and Vacuolization	45
3	Effect of Growth Factor and Nutrient Deprivation	48
3.1	Endothelial Cells reduce Viability in Absence of Serum	48
3.1.1	Upon Serum-Starvation Sub-Confluent Endothelial Cells Change their Morphology and Appear Elongated	48
3.1.2	Serum-Starvation Induced Viability Decrease cannot be Rescued by Addition of Single Growth Factors	49

3.2	Serum-Starvation of HeLa Cells does not Alter Their Proliferation Rate for 12 Hours	51
3.2.1	Prolonged Serum-Starvation of HeLa Cells Reduces Proliferation Rate and can be Rescued even after 94 Hours of Starvation	52
3.3	Endothelial Cells reduce Migration in Response to Serum and Nutrient Starvation	53
3.3.1	Endothelial Cell Migration Requires Serum irrespective of the Concentration	53
3.3.2	Glucose Starvation has only Minor Influence on Endothelial Cell Migration	54
3.3.3	Previous Starvation of Primary EC decreases Migration Velocity	54
3.4	Various Cell Lines respond differently to Serum and Nutrient Starvation	55
3.4.1	Glucose-Starved HeLa Cells Decrease Viability after 29 Hours	56
3.4.2	Serum-Starvation of HeLa Cells does not Alter Viability but Diminishes Proliferation	57
3.4.3	Endothelial Cells Proliferate Less than HeLa Cells in all Conditions and are more Sensitive to Starvation	58
3.4.4	Galactose Promotes more Cell Growth in Absence of Serum	58
3.4.5	Pancreatic β -Cells are more Susceptible to Starvation than HeLa and Endothelial Cells	59
3.4.6	Re-addition of Glucose Rescues Starved HeLa Cells and Transiently Enhances their Division Rate	61
4	Effect of Altering the Mitochondrial Ca^{2+} Uptake Machinery	63
4.1	Stable Knockdown of MCU does not influence Viability or Proliferation of HeLa Cells	63
4.2	Transient Knockdown of MICU1 Makes HeLa Cells Less Susceptible to Apoptotic Cell Death	66
4.3	Transient Knockdown of MICU1 Does not Influence Endothelial Cell Migration	66
4.4	Annexin A5 Knockdown Does not Influence Proliferation of HeLa Cells	67
4.4.1	ANXA V KD HeLa Cells Have an Increased Proliferation Rate Compared to MCU KD HeLa Cells	69

4.4.2	Transient UCP3 Overexpression Increases Proliferation in Stable MCU Knockdown HeLa Cells	69
5	Correlation with Intracellular Measurement Assays	70
5.1	Higher Proliferative HeLa Cells Have an Elevated Metabolic Rate and $[ATP]_{ER}$ Increase upon Ca^{2+} Mobilisation	70
5.2	Glucose Starvation Reduces the Ca^{2+} -Coupled $[ATP]_{ER}$ Increase and is Restored after 4 Hours	72
5.3	Inhibition of AMP-activated Protein Kinase Reduces Cell Viability and the Ca^{2+} -Coupled $[ATP]_{ER}$ Increase	74
5.4	Serum Starvation makes HeLa Cells more Susceptible to the Ca^{2+} -Coupled $[ATP]_{ER}$ Increase	78
IV.	Discussion	79
1	Long-Term Live-Cell Imaging Shows the Kinetics of Assays	79
2	Proliferation Determined by Cell Count Analysis is more Sensitive than Confluency Analysis	80
3	Analysis of Cell Exclusion Insert Assays is more Straightforward than of Scratch Assays	82
References		XVI
Addendum		XXXI
Scheme of Experiments		XXXI
Publications		XL
Presentations		XL
Prize		XL

Abbreviations

[...]	concentration
Δ	delta, relative change
μ	micro (10^{-6})
ACLSM	array confocal laser scanning microscope
AEA	anandamide
AMP	adenosine monophosphate
AMPK	5' adenosine monophosphate-activated protein kinase
ANOVA	Analysis of variance
ANXA V	Annexin A5
AT1.03	cytosolic FRET-based ATP sensor
ATP	adenosine triphosphate
BSA	bovine serum albumin
Ca ²⁺	Calcium
CAD	Caspase-Activated DNase
CC	Compound C
CCD	charged-coupled device
CO ₂	carbondioxide
D1ER	second generation cameleon (calcium sensor) targeted to ER
DAPI	4',6-diamidino-2-phenylindole
DIC	differential interference contrast
DMEM	Dulbecco's Modified Eagle Medium
DMSO	Dimethyl sulfoxide
DNA	desoxyribonucleic acid

EA.hy926	endothelial cell line
ECGS	endothelial cell growth supplement
EGF	epidermal growth factor
ER	endoplasmic reticulum
ERAT4.01	FRET-based ATP sensor targeted to the ER
FCS	fetal calf serum
FGF	fibroblast growth factor
FRET	<i>Förster</i> resonance energy transfer
g	gram
GF	growth factor
h	hour
HeLa	human cervical cancer cell line, derived from Henrietta Lacks
HEPES	2-[4-(2-hydroxyethyl)piperazin-1-yl]ethanesulfonic acid
HUVEC	human umbilical vein endothelial cell
INS-1	rat insulinoma cell line
KD	knockdown
LED	light-emitting diode
M	molar
m	meter
m	milli (10^{-3})
M13	Skeletal Muscle Myosin Light Chain Kinase
MCU	Mitochondrial Calcium Uniporter
MEM	Minimal Essential Medium
MICU1	Mitochondrial Calcium Uptake 1
mRNA	messenger ribonucleic acid

MTT	3-(4,5-dimethylthiazol-2-yl)-2,5-diphenyltetrazolium bromide
n	nano (10^{-9})
NADH	Nicotinamide adenine dinucleotide
NADPH	Nicotinamide adenine dinucleotide phosphate
OA	oleic acid
oe	overexpression
PA	palmitic acid
PAEC	porcine aortal endothelial cell
PALM	photo activated localization microscopy
PAM	programmable array microscopy
PBS	phosphate buffered saline
pH	acidity
PI	propidium iodide
PI3K	Phosphoinositide 3-kinase
pKa	acid dissociation constant
RNA	ribonucleic acid
RNAi	RNA interference
ROI	region of interest
rpm	revolutions per minute
RPMI	Roswell Park Memorial Institute
s	second
shRNA	short hairpin ribonucleic acid
siRNA	small interfering ribonucleic acid
SSIM	saturated structured illumination microscopy
STED	stimulated emission depletion

STORM	stochastic optical reconstruction microscopy
TP	timepoint
TUNEL	terminal deoxynucleotidyl transferase dUTP nick end labeling
UCP3	Uncoupling Protein 3
VEGF	vascular endothelial growth factor
WM	wortmannin

List of Figures

1	Phase Contrast Microscopy	2
2	Imaging setup for simultaneous recording of two fluorescent probes	3
3	Double Staining	4
4	<i>Förster</i> resonance energy transfer (FRET)	7
5	Cell lines used	11
6	Confluency of EA.hy926 cells	18
7	Confluency of HeLa cells	19
8	Dead cells	22
9	Examples of migration assays	23
10	Cell Exclusion Zone Insert	24
11	Example of incubation contamination	26
12	Growth of cells is partially dependent on the buffer	27
13	Examples of cell culture plates and dishes	28
14	Influence of light in migration of EC	29
15	Cell-Counter of Cell-IQ Analyser	31
16	Sample library of Cell-IQ Analyser	31
17	Cell type recognition with Cell-IQ Analyser	32
18	Viability analysis	33
19	Examples of Intensity Analysis	34
20	Comparison of intensity and morphology analysis	35
21	Migration analysis	38
22	Migration analysis II	38
23	Percentage bias of migration analysis	40
24	Examples of multi-nucleated cells	42
25	Example of a cell fusion after division	42
26	Example of triplicate division of a primary endothelial cell	43
27	Analysis of vacuole appearance	44
28	Phototoxic effect of <i>Crateagus</i> extract WS-1442	46
29	Effect of serum starvation on sub-confluent cells	49
30	Effect of serum starvation on confluent cells	50
31	Growth of HeLa cells in response to serum starvation	52
32	Migration stimulation	53
33	Effect of glucose starvation on cell migration	54
34	Effect of starvation on primary endothelial cells	55

35	Glucose starvation decreases viability in cell culture medium	56
36	Glucose starvation decreases viability in cell culture medium II	57
37	Glucose starvation decreases viability in experimental buffer	61
38	Re-addition of nutrients rescues HeLa cells	62
39	Viability assay of MCU KD and control HeLa cells	64
40	Proliferation assay of MCU KD and control HeLa cells	65
41	Viability assay of siMICU1 and control HeLa cells	66
42	Migration assay of siMICU1 and control HeLa cells	67
43	Proliferation assay of MCU KD, ANXA V KD, and control HeLa cells . . .	68
44	Correlation of proliferation with intracellular ATP signals	71
45	Intracellular Calcium and ATP signals of high and low proliferating cells .	73
46	Correlation of viability and intracellular Calcium and ATP signals upon glucose starvation	74
47	Effect of pharmacological activation of inhibition of AMPK	75
48	AMPK is activated by glucose starvation	76
49	Correlation of viability and intracellular Calcium and ATP signals upon FCS starvation	78

List of Tables

1	Buffers and Media used	10
2	Experimental Buffers	16
3	Conditions used in the experiment presented in Figure 30	51
4	Conditions and results from the experiment presented in Figures 35 and 36	59
5	Conditions used in the experiment presented in Figures 43	69
6	Conditions used in the experiment presented in Figures 47	76

Zusammenfassung

Langfristige Echtzeitaufnahmen von Zellpopulationen können sich als sehr nützlich erweisen um die Viabilität, Proliferation und Migration zu bestimmen. Fortschritte innerhalb der letzten Jahrzehnte haben die Beobachtung von Zellkulturen - potenziell kombiniert mit Fluoreszenz - über Tage ermöglicht, indem Zellinkubatoren mit Mikroskopen kombiniert wurden.

Ich habe mikroskopische Verfahren zur Bestimmung der Viabilität, Proliferation und Migration an einem Zeiss[®] Axiovert Observer Mikroskop etabliert und es mit dem innovativen, speziell für diese Anwendungen entwickelten Cell-IQ[®] System verglichen. Drei Zelllinien wurden mit diesen Techniken untersucht, die endothelialen EA.hy926, die Zervixkarzinom HeLa und die pankreatischen β (INS-1) Zellen. Während die INS-1 Zellen Serum- oder Nährstoffentzug nicht allzu lang tolerierten, konnten sowohl die EA.hy926 als auch die HeLa Zellen für bis zu 4 Tage in Entbehrung überleben. Dabei trat eine Wachstumseinschränkung auf, welche jederzeit durch Hinzugabe der jeweiligen limitierten Resource rückgängig gemacht werden konnte.

Stabiler Knockdown des Mitochondrial Ca^{2+} Uniporter (MCU) oder Annexin A5 in HeLa Zellen hatten keinen Einfluss auf die Viabilität oder Proliferation. Transienter Knockdown von Mitochondrial Ca^{2+} Uptake 1 (MICU1) hatte keinen Einfluss auf die Migration der EA.hy926 Zellen, weder im Scratch noch im Cell Exclusion Zone Insert Assay.

Schließlich korrelierte ich intrazelluläre Signale von *Förster* Resonanz Energie Transfer (FRET)-Sensoren mit der Viabilität und Proliferation von Zellen. Ca^{2+} wurde aus dem Lumen des Endoplasmatischen Reticulums (ER) entlassen, was von einem Anstieg des ATP in dieser Organelle begleitet wurde, wie kürzlich von uns gezeigt wurde.

Ich konnte zeigen, dass solche HeLa Zellen mit einer schnelleren Proliferation einen signifikant erhöhten Ca^{2+} -bezogenen $[\text{ATP}]_{\text{ER}}$ Anstieg im Vergleich zu langsamer proliferierenden Zellen aufweisen. Außerdem hatten HeLa Zellen unter Glukoseentzug einen drastisch reduzierten Ca^{2+} -bezogenen $[\text{ATP}]_{\text{ER}}$ Anstieg innerhalb von Minuten, welcher sich von alleine nach etwa 4 Stunden erholte. In dieser Zeitspanne konnte ich keinen Unterschied in der Viabilität feststellen.

In meiner Diplomarbeit habe ich verschiedene Analysetechniken verglichen: die Intensitäts- und die morphologische Analyse für die Viabilität, die Konfluenz- und Zellzahlbestimmung für die Proliferation und die manuelle oder die automatische Analyse für die Migration. Zellen konnten semiautomatisch anhand ihrer Morphologie erfolgreich unterschieden werden, z.B. in viable, tote oder sich teilende. Meine Ergebnisse zeigen, dass sich alle diese Techniken für High-Throughput-Analysen eignen.

Abstract

Long-term live-cell imaging can be a powerful tool to assess viability, proliferation, and migration of cell populations. Advances over the past couple of decades brought an incubator to the microscope, enabling the observation of cell cultures over days, potentially in combination with fluorescence.

I established microscopic viability, proliferation, and migration assays on a Zeiss® Axiovert Observer and compared it with a cutting-edge system specifically dedicated for those purposes, a Cell-IQ®. Three cell lines were tested in those assays, endothelial EA.hy926, cervical cancer HeLa, and pancreatic β (INS-1) cells, respectively. While the INS-1 cells did not tolerate serum or nutrient deprivation very long, both the EA.hy926 and HeLa cells remained viable in austerity for up to 4 days. This was accompanied by a growth arrest, which could be rescued by re-applying the respective scarce resource after any tested period.

Stable knockdown of the Mitochondrial Ca^{2+} Uniporter (MCU) or Annexin A5 did not influence viability or proliferation of HeLa cells. Transient knockdown of Mitochondrial Ca^{2+} Uptake 1 (MICU1) did not influence EA.hy926 migration, neither in a scratch nor a cell exclusion zone insert assay.

Finally, I correlated intracellular signals determined by *Förster* Resonance Energy Transfer (FRET)-based sensors with the viability and proliferation of cells. Ca^{2+} was released from the lumen of the Endoplasmic Reticulum (ER), which was recently shown to correlate with an immediate rise of ATP in this organelle by us.

By inducing HeLa cells to proliferate fast or slow by means of cell culture treatments, I found, that the highly proliferative HeLa cells had a significantly elevated Ca^{2+} -coupled $[\text{ATP}]_{\text{ER}}$ increase compared to the slowly proliferating HeLa cells. Furthermore, glucose-starved HeLa cells had a drastically diminished Ca^{2+} -coupled $[\text{ATP}]_{\text{ER}}$ increase within minutes, which was restored after about 4 hours of starvation without further treatment. During this time, no change in viability was observed.

In my diploma thesis, I compared various analysis techniques, intensity or morphological analysis for viability-, confluency or cell count determination for proliferation-, and manual or automatic migration-assay analysis. Different types of cells, i.e. viable, dead, dividing, and even vacuolized cells could semi-automatically be differentiated by morphological analysis. Based on my results, I conclude that all those assays are feasible for high-throughput analysis.

I. Introduction

1. Live Cell Imaging

In live cell imaging, living cells are studied by means of time-lapse microscopy. The pioneering attempts of this method, at first termed microcinematography (commented in (Landecker, 2009)), were performed in the first decade of the 20th century to visualize cell division (Comandon, 1909; Ries, 1909; Talbot, 1913). Prior to the development of the time-lapse microscopy, the observation of cellular processes was mainly limited to the use of chemical dyes to stain fixed samples. On the one hand, this led to the possible observation of structures that were hidden from perception by pure light microscopy (Ehrlich, 1877), on the other hand the staining process included fixation of samples, thus only static, devitalized structures were perceived. Additionally, only those structures that were stainable could catch attention.

Microcinematography added live and plasticity to these static structures, thereby widening the scope of biological research. By this method, various cell types and processes could be observed, e.g. the developing rabbit egg cells (Lewis and Gregory, 1929) or migration of lymphocytes (Lewis and Webster, 1921; Lewis and Lewis, 1939). Soon, its value was also appreciated in the medical sciences (Rosenberger, 1929).

However, with the simplest form of light microscopy, i.e. bright-field microscopy, most of the details within a sample remain invisible.

1.1. Phase Contrast Microscopy

A breakthrough in optical visualization of living, unstained samples was made with the invention of phase contrast microscopy by Frits Zernike in the 1930's (Zernike, 1942; Zernike, 1955).

Phase refers to a particular point in the cycle of a sinusoidal wave, such as light. When light passes through one medium, it is characterized by a phase, amplitude, and frequency. Transition of light from one medium to another with diverging refractive indices (e.g. liquid to air) leads to a change in phase and amplitude. While differences in amplitude are recognized by the human eye and standard photography as brightness shifts, phase shifts are invisible without the help of special equipment. Those changes are typically invisible for the human eye, yet might reveal worthwhile information. This technique enables a researcher to rectify structures, that would otherwise remain in the blind spot of optical microscopy, only observable through *ex vivo* staining. In phase contrast microscopy, changes in the phase of the light are visualized by separating the illumination background light from the specimen scattered light. Essentially, this improves the contrast of an image

enabling visualization of previously invisible structures.

This technique was further developed by Georges Nomerski to differential interference contrast (DIC) microscopy (Françon, 1964), and Robert Hoffman to Hoffman modulation contrast microscopy (Hoffman, 1977). More recently with the advent of digital photography in the 1990's quantitative phase contrast microscopy methods were developed, that increase the contrast by creating a second image with different phase and interfering those with each other, as e.g. in ptychography (Marrison et al., 2013).

Use of phase contrast microscopy enabled the descriptive basis of the current view of cell migration (Abercrombie and Heaysman, 1953).

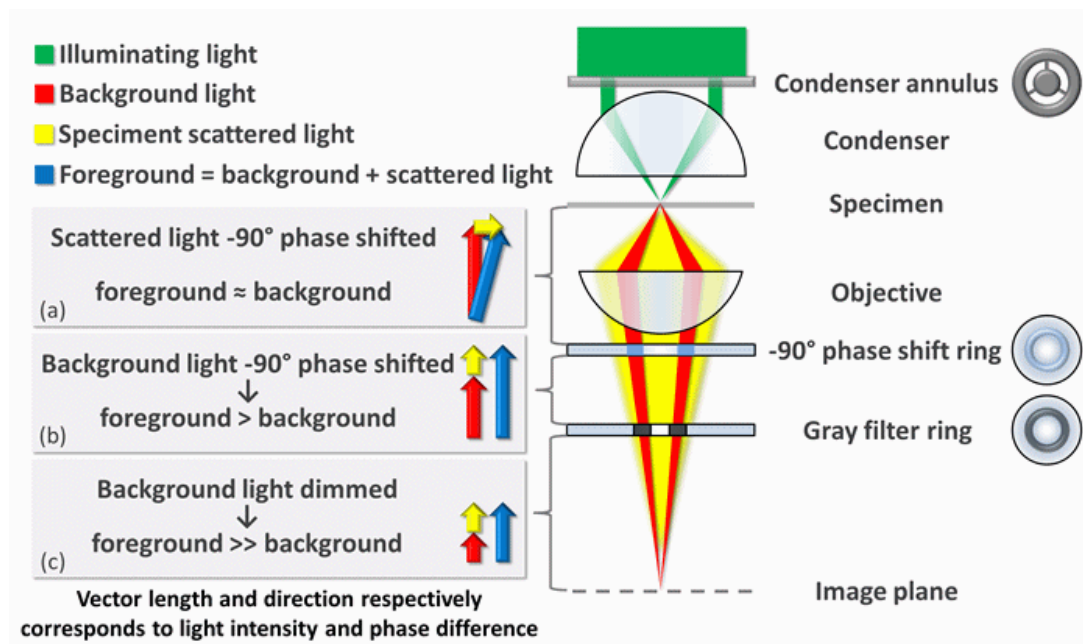


Figure (1): Example of phase contrast microscopy. Figure copied from wikipedia (Phase contrast microscope). Author: Egelberg (licensed under Creative Commons Attribution-Share Alike 3.0 Unported)

1.2. Combination with an Incubator

The time-lapse microcinematography attempts so far shown were recorded in the time frame of a couple of hours in the maximum. However, if one is interested in studying the development and differentiation of cells over a period of days, the incubation of the cells limits the observation length. To achieve this, the combinatorial use of an incubator is required. Typically, people did not address to this note, as it was thought, that the warm and humidified atmosphere within an incubator would necessarily destroy the intricate optics of a microscope (Baker, 2010). The first to successfully test the combinatorial use of a microscope with an incubator was Sally Temple in 1986 (Temple and Raff, 1986). Nowadays a plethora of devices exist that bring the cell culture incubation into the mi-

croscope, like the Holomonitor M4, Olympus[®] VivaView[®], Nikon[®] Cell Incubator Observation, Zeiss[®] Axiovert Incubator, or ChipmanTechnologies Cell-IQ[®] to name just a few.

1.3. Fluorescence Microscopy

Fluorophores are compounds, that can emit light of a certain wavelength upon excitation with a certain (shorter) wavelength. Typically, they contain multiple aromatic groups. In fluorescence microscopy, this feature is used to study and localize these fluorophores within a sample (Ghiran, 2011). Briefly, the components of a fluorescence microscope are a light source (e.g. xenon arc lamps, LED's, or lasers), an excitation filter, a dichroic mirror, and an emission filter, which allows separation of the intense illumination light from the much weaker emitted light (Figure 2). In biological sciences, mostly epifluorescence microscopes are used, in which fluorophore excitation and fluorescence detection occur via the same light path. Generally, multi-color images are derived from multiple images of the same sample, excited with different wavelength (Figure 3) (Sawano et al., 2002).

The first applications derived from the use of fluorescent chemical compounds like DAPI (Kapuscinski, 1995) and Hoechst (Latt et al., 1975) which bind the minor groove of DNA, thus staining nuclei, or phalloidin, which is used to stain actin fibers (Cooper, 1987; Capani et al., 2001). Other compound even change their fluorescence depending on their

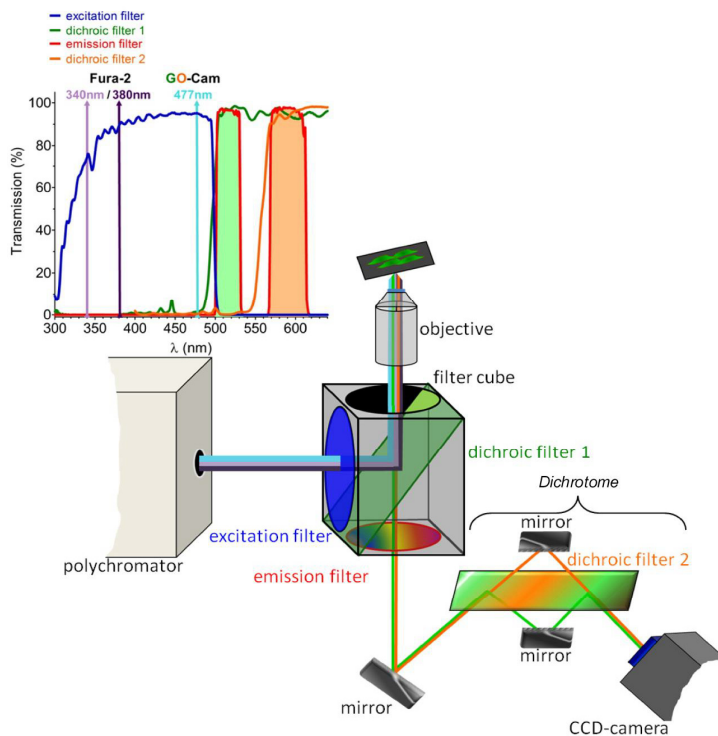


Figure (2): Schematic representation of an imaging setup of a fluorescent microscope. The light paths of the excitation - (violet = 340 nm, dark blue = 380 nm, and light blue 477 nm) is generated in the polychromator and is reflected on the dichroic mirror through the objective to the sample. There, the fluorophore emits the corresponding light (green = 510 nm and orange = 560 nm), which travels through the objective again and passes through the dichroic mirror. Via a further set of mirrors and filters, both wavelengths are separated and finally detected by a CCD-camera to simultaneously image the Ca^{2+} indicator fura-2 and red-shifted cameleons (D1GO-Cam). Left corner curve shows the respective excitation and emission maxima. from (Waldeck-Weiermair et al., 2012)

environment, e.g. acridine orange. The fluorescence of this cationic dye changes from an excitation and emission maximum of 502 nm and 525 nm (green), respectively, when bound to DNA to excitation maximum of 460 nm (blue) with an emission maximum of 650 nm (red) (Traganos et al., 1977). In addition, this dye can enter acidic compartments, such as lysosomes (Canonica and Bird, 1969). In such low pH conditions the emission maximum can be seen at 600 nm (orange) when excited at 460 nm.

Other applications are primary or secondary immunofluorescence by which antibodies labeled with a fluorophore are used to localize cellular structures (Fritschy and Härtig, 2001). Last but not least, a plethora of fluorescent proteins exist, mostly derived from the green fluorescent protein (GFP) (Shimomura et al., 1962; Chalfie et al., 1994; Ormö et al., 1996; Tsien, 1998), which led to the 2008 Nobel Prize for Martin Chalfie, Osamu Shimomura, and Roger Y. Tsien. Those fluorescent proteins can be genetically coupled to proteins of interest, whereby the cellular localization can specifically be determined *in vivo* (Chudakov et al., 2005).

However, use of fluorescence has some drawbacks. Firstly, fluorophores undergo a process termed photobleaching, a consequence of excitation-induced damage to the fluorophores, which limits the lifetime of a fluorophore. Secondly, fluorophore-laden cells are more susceptible to phototoxicity, particularly via the generation of reactive oxygen or nitrogen species (Hoebe et al., 2007). Another factor is, that observation via fluorescence is blind to the occurrence of any other, non-labeled structure or process.



Figure (3): Example of a double labeled cell. Cells were transfected with the red-fluorescent Ca^{2+} probe D1GO-Cam (*left panel*), loaded with violet fluorescent fura-2 (*middle*). Subsequently, both images were overlaid (*right*). from (Waldeck-Weiermair et al., 2013)

1.3.1. Confocal Microscopy

Confocal microscopy increases the optical resolution and contrast of a sample (Pawley, 1995). This is achieved by sending a light beam through a pinhole, thereby limiting the spatial spreading of the light. By this only in-focus areas of a specimen produce an image. The technique was invented by Marvin Minsky in 1955 (Minsky, 1988). Here, the observable range is limited by the wavelength, between 340 nm in the violet and about 800 nm in the red, accordingly. The light source is typically a laser, thus light of high intensity is

used, potentially altering the cellular structure through phototoxic effects (Hoebe et al., 2007).

Another limitation of this technique is the small sample size that can be visualized at any time. This can be solved by various means. i.) in *confocal laser scanning microscopy* multiple mirrors are used to scan the entire sample (Paddock, 1999). ii.) a *Nipkow disk* (also called scanning disk), which has multiple pinholes can be applied (Pawley, 1995). Light passes through only one pinhole at a time. As the disk rotates very fastly between the light source and the sample, a multitude a images are created, which are subsequently combined by a computer, resulting in one sharp image.

iii.) *programmable array microscopy (PAM)* makes use of electronically controlled light modulators, that produce multiple moving pinholes (Caarls et al., 2011). All those processes can be repeated in a z-scan, whereby various heights of the sample are scanned. Afterwards those images can be used to produce a three-dimensional model, which shows the exact spatial composition of flourophores, i.e. flourescently labeled protein within a cell.

An alternative is the use of *two photon microscopy* (Benninger and Piston, 2013), which yields a deeper tissue penetration, more efficient light detection, and less phototoxicity (Patterson and Piston, 2000) than confocal microscopy. The basic principle is, that instead of one high energy photon, two photons with approximately half the energy are used simultaneously to excite the flourophore.

1.3.2. Super-Resolution Imaging

The techniques presented so far all are limited by the diffraction limit of light, first described by Ernst Abbe in 1874, which stated that the maximal resolution of a microscope is limited to about half the length of the wave used to derive to image, or about 250 nm. This notion was widely accepted until the development of *super-resolution microscopy* techniques, first of all stimulated emission depletion (*STED*) *microscopy* developed in 1994 by Stefan Hell (Hell and Wichmann, 1994; Egner et al., 2002; Hell, 2010). Other techniques include stochastic optical reconstruction microscopy (*STORM*) (Rust et al., 2006), Photo Activated Localization Microscopy (*PALM*) (Betzig et al., 2006), and Saturated structured illumination microscopy (*SSIM*) (Gustafsson, 2005). Those methods enable a resolution of a few nm, theoretically below 10 nm, which allows single-particle tracking (Johnson-Buck et al., 2013).

I will not go into the physical details of the super-resolution techniques, as this would go far beyond the scope of this thesis. All have certain advantages and disadvantages, generally, the drawbacks are similar to confocal and flourescence microscopy, i.e. photo-bleaching and phototoxicity, but to a more pronounced level, as the used photons are

typically more energetic. Accordingly a compromise between super-resolution and physiologic imaging conditions have to be made. Recent advances, however, have been made to approach those limitations, which led to the establishment of instant SIM (York et al., 2013), with high spatial and temporal resolution, and even label-free super-resolution techniques (Kaufmann et al., 2011; Ayas et al., 2013).

1.3.3. Resonance Energy Transfer Microscopy

Apart from tracking and localizing structures, flourophores can also be used to measure e.g. the concentration of certain molecules or enzyme activity within living cells in real-time. At first, this was attempted by use of chemical flourophores, that change their flourescent properties upon binding with a substrate. Ideally, ratiometric, i.e. with two emission maxima, one that increases flourescence, while the other decreases upon binding, probes are used, because those give information about the concentration of substrate irrespective of the flourophore concentration. These include the Ca^{2+} indicators fura-2, or indo-1 (Grynkiewicz et al., 1985). However, those fourophores enter the cell and distribute within the cytosol. If more detailed information about the concentration of Ca^{2+} within subcellular compartments (i.e. organelles) is required, different attempts are required. E.g. the non-ratiometric dye Rhod-2 accumulated within mitochondria and was successfully used to measure its content (Davidson and Duchen, 2012). However, as it is non-ratiometric the signals are difficult to quantify.

Another means by which those measurements can be performed, is the use of flourescent proteins (Palmer et al., 2011). Various genetically encoded sensors exist, to measure among others the Ca^{2+} concentration within cells and organelles (Miyawaki et al., 1997; Palmer and Tsien, 2006), ATP concentration (Imamura et al., 2009; Nakano et al., 2011; Vishnu et al., 2013), the redox state (Lukyanov and Belousov, 2013), protein-protein interactions (Deak et al., 2013), or enzyme activity (Tsou et al., 2011). Most of these sensor are based on *Förster* resonance energy transfer (FRET) (Jares-Erijman and Jovin, 2003), a process first postulated by Theodor Förster (Förster, 1948). FRET is a process, by which energy is directly transfered between two chromophores in close vicinity, also known as non-radiative energy transfer (Andrews and Bradshaw, 2004).

This technique is not limited to the use of flourescent proteins (Pfleger and Eidne, 2006), but I will focus on this application. Essentially, FRET occurs between two flourescent proteins adjacent to each other, if the emission spectrum of one protein (donor) significantly overlaps with the excitation spectrum of the other (acceptor).

As an example of a FRET-based sensor, I use a red-shifted (in contrast to the commonly used yellow-shifted) Ca^{2+} sensor (cameleon, Figure 4 B and C), published by our group during the work of my diploma thesis (Waldeck-Weiermair et al., 2012). The cameleons

are composed of a Ca^{2+} sensing calmodulin (CaM) domain and the Ca^{2+} -CaM interacting peptide of the myosin light chain kinase, M13, flanked by two fluorescent proteins on the C- and N-terminus, respectively (Miyawaki et al., 1997). Binding of Ca^{2+} leads to a conformational change in the CaM-M13 domains, whereby the two fluorophores come in close vicinity, yielding a FRET signal.

Various ways of analysis of FRET exist (Spiering et al., 2013), I present the common analysis in Figure 4 C (Waldeck-Weiermair et al., 2012).

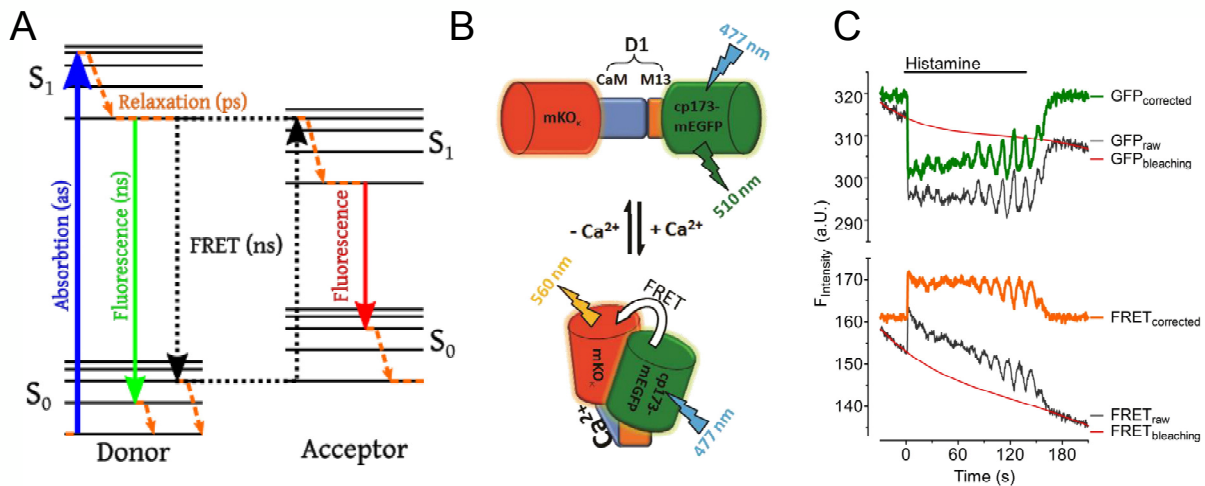


Figure (4): FRET microscopy. **A:** Jablonski diagram of a FRET pair. Upon excitation of the donor to the excited S_1 state, instead of emitting a photon at relaxation, the acceptor is directly excited, yielding its specific fluorescent photon (Author: Alex M Mooney, licensed under Creative Commons Attribution-Share Alike 3.0 Unported). **B:** Example of a FRET-based Ca^{2+} sensor (from (Waldeck-Weiermair et al., 2012)). Upon binding of Ca^{2+} , the conformation of the sensor changes, leading to intramolecular FRET. **C:** Representative recordings of cytosolic Ca^{2+} oscillations upon cell stimulation with 100 mM histamine in intact HeLa cells expressing D1GO-Cam. The black curves represent original traces of the FRET donor GFP (*upper panel*) and the respective FRET signal (*lower panel*). At the moment of histamine stimulation, the donor signal decreases, while the acceptor signal increases, which is *per definitionem* FRET. Original traces (black) were corrected for photobleaching using the red curves (representing the bleaching functions regarding a one phase exponential decay) yielding the corrected traces for the GFP (FRET donor, green trace, *upper panel*) and the FRET channel (orange trace, *lower panel*), respectively.

2. Aims of this Diploma Thesis

The main objective of my diploma thesis was to establish long-term live-cell imaging techniques in our laboratory and thereby amend the wealth of our assays. The focus was put on the development of microscopic viability, proliferation, and migration assays, respectively. This included testing and establishing various techniques of analysis.

Secondary objectives were:

- to develop conditions, which yielded clear differences in viability, proliferation, and migration (e.g. various starvation conditions)
- to apply those assays in the course of other projects of our laboratory:
 1. to study the lipotoxic effects of palmitic acid (PA)
 2. to investigate the effects of the *Crateagus* extract WS-1442 on endothelial cells
 3. to determine the influence of the endocannabinoid anandamide (AEA) on endothelial cell migration
 4. to elaborate a putative impact of mitochondrial Ca^{2+} uptake on cell viability, proliferation, and migration
 5. to measure the effect of AMP-activated Protein Kinase (AMPK) on viability and proliferation
- to correlate long-term live-cell imaging assays with short-term live-cell imaging and metabolic assays

II. Material and Methods

1. Materials

1.1. Chemicals

Cell culture materials were purchased from Gibco, Invitrogen (Vienna, Austria), and fetal calf serum (FCS) and media supplements were from PAA laboratories (Pasching, Austria).

Palmitic Acid (PA), Oleic Acid (OA), bovine serum albumin (BSA), Wortmannin (WM), AICAR, Compound C (CC), C2-Ceramide, MTT stock solution, and the growth factors (GF) epidermal GF (EGF), vascular endothelial GF (VEGF), fibroblast GF (FGF), and endothelial cell growth supplement (ECGS) were from Sigma-Aldrich (Vienna, Austria). Anandamide (AEA) was from Tocris Cookson (Abingdon, United Kingdom). The crataegus extract WS 1442 was a kind gift from Elisabeth Willer (LMU, Munich, Germany). Ionomycin was from Abcam[©].

NaCl, KCl, Na₂HPO₄, MgCl₂, Hepes, D-glucose, NaHCO₃, KH₂PO₄, CaCl₂, β - Mercaptoethanol and all other chemicals were provided from Roth (Karlsruhe, Germany), unless stated differently.

1.2. Plates and Dishes

35 mm dishes and 6- to 48-well plates were from Greiner (Kremsmünster, Austria), Corning (Amsterdam, Netherlands), PAA (Pasching, Austria), or SDL Life Sciences (Stuttgart, Germany), respectively.

8-well slides were from ibidi[®] and PAA, respectively, silicon-based wound-healing inserts were from ibidi[®] (Munich, Germany).

1.3. Cell Culture Media and Buffers

EA.hy926 and HeLa cells were routinely incubated in Dulbecco's Modified Eagle Medium (DMEM, Sigma-Aldrich, Vienna, Austria) (Dulbecco and Freeman, 1959). During experiments, cells were either incubated in the same medium, or in a loading buffer. PAEC were incubated in DMEM or Minimal Essential Medium (MEM, Sigma-Aldrich) (Eagle, 1959). INS-1 cells were incubated in Roswell Park Memorial Institute medium (RPMI, Sigma-Aldrich) (Moore et al., 1967). Compositions are listed in Table 2.

	DMEM	MEM	RPMI	Loading Buffer
Inorganic Salts (mg/l)				
Ca(NO ₃) ₂			100	
CaCl ₂	264	200		294
Fe(NO ₃) ₃	0.1			
MgSO ₄	200	97.67	48.84	
MgCl ₂				203.3
KCl	400	400	400	375
KH ₂ PO ₄				60
NaHCO ₃	3700	2200	2000	218.4
NaCl	6400	6800	6000	7830
NaH ₂ PO ₄	141	138		
Na ₂ HPO ₄			800	48.3
Amino Acids (mg/l)				
L-Arginine	84	126	200	126.4
L-Asparagine			50	
L-Aspartic Acid			20	
L-Cystine	63	31	65	24
L-Glutamine	580	292	300	367.2
L-Glutamic Acid			20	
Glycine	30		10	
L-Histidine	42	42	15	42
L-Hydroxyproline			20	
L-Isoleucine	105	52	50	52.4
L-Leucine			50	52.4
L-Lysine	146	73	40	72.5
L-Methionine	30	15	15	15.1
L-Phenylalanine	66	32	15	33
L-Serine	42		30	
L-Threonine	95	48	20	47.6
L-Tryptophane	16	10	5	10.2
L-Tyrosin	72	52	29	36
L-Valine	94	46	20	46.8
Vitamins (mg/l)				
Biotin			0.2	
Choline chloride	4	1	3	1
D-Calcium panthothenate	4	1	0.25	1
Folic acid	4	1	1	1
Niacinamide	4	1	1	1
Para-Aminobenzoic Acid			1	
Pyridoxine hydrochloride	4	1	1	1
Riboflavin	0.4	0.1	0.2	0.1
Thiamine hydrochloride	4	1	1	1
Vitamin B ₁₂			0.005	
i-Inositol	7.2	2	35	2
Other Components (mg/l)				
D-Glucose	1000	1000	2000	2000
Phenol Red	15	10		
Sodium Pyruvate	110			
Gluthathione			1	
Hepes				2380

Tab. (1): Buffers and Media used (numbers refer to concentration in mg/l). DMEM = Dulbecco's Modified Eagle Medium, MEM = Minimal Essential Medium, RPMI = Roswell Park Memorial Institute Medium. All media contain 1% Penicillin / Streptomycin and 1% Amphotericin-B. If stated, glucose was replaced by galactose or mannitol, respectively.

2. Cell Culture

Some experiments were performed with the EA.hy926 cell line, a hybrid endothelial cell (EC) line resulting from the merger of primary human umbilical vein cells (HUVEC) with the human lung cancer cell line A549 (Edgell et al., 1983; Bouïs et al., 2001). EA.hy926 cells were kindly provided by J.S. Edgell (University of North Carolina, Chapel Hill, NC, USA) were used at passages 45 to 100 and grown in Dulbecco's Modified Eagle Medium (DMEM) containing 10 % FCS, 1 % HAT (5 mM hypoxanthin, 20 μ M aminopterin and 0.8 mM thymidine), 50 units/ml penicillin, 50 μ g/ml streptomycin, and were maintained at 37 °C in 5 % CO₂ atmosphere in a cell incubator until optimal confluency was reached. Primary HUVEC's were kindly provided by Elisabeth Willer (LMU, Munich, Germany). Those primary cells are only stable for approximately one to three passages. Our laboratory does not typically work with primary cells, hence only a limited number of experiments could be performed. HUVEC's were grown in endothelial cell growth medium (Provitro, Berlin, Germany) containing 10 % fetal bovine serum (Biochrom, Berlin, Germany), PAEC were grown in DMEM or MEM as stated. Description of HUVEC preparation can be read elsewhere (Fürst et al., 2008).

Porcine aortal EC (PAEC) were received from the Institute of Pharmaceutical Sciences, University of Graz. Other experiments were performed with the human cervical cancer cell line HeLa (Skloot, 2010), which were cultured in medium similar to the EA.hy926 medium, but without HAT supplement. Recently I performed experiments with HeLa SilenciX cells with a stable knockdown of mitochondrial Ca²⁺ uniporter (MCU KD), Annexin A5 (ANXA V KD) or respective scrambled shRNA expressing (Control) HeLa cells (tebu-bio, Offenbach, Germany).

Rat insulinoma cell line INS-1 (Skelin et al., 2010) were grown in Roswell Park Memorial Institute Medium (RPMI) and kindly provided by Prof. Dr. C. B. Newgard (Duke University, Durham, NC).

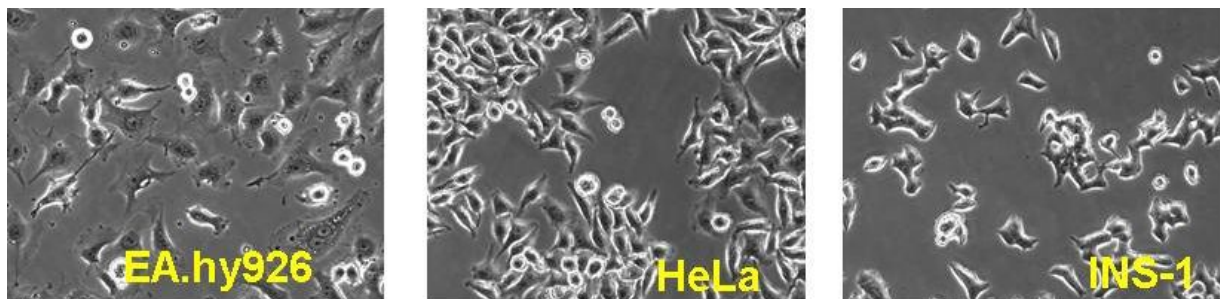


Figure (5): Cell lines used during this thesis: endothelial EA.hy926 cells, cervical cancer HeLa cells, and rat insulinoma INS-1 cells

3. Loading Cells with Chemicals

Two attempts of treating cells with various substances were performed: (i) Cells were treated with different chemicals and biological agents in the cell culture medium before microscopic imaging and incubated for a pre-defined amount of time. This was typically applied for the real-time long-term image series. In most cases, substances were added 10-45 minutes before the experiment started, depending on the microscopy system and the number of conditions applied. Sometimes, the medium was changed during the experiment, if stated. Subsequently the same positions were further observed (possible in the Cell-IQ[©]).

(ii) Different buffers and substances were applied during experiments in a perfusion chamber. This was done for the intracellular Ca^{2+} and ATP measurements.

4. Transfection

Typically, to conduct the transfection, DNA or RNA is added to a serum-lacking medium and a reagent that enables the nucleic acids to pass the plasma membrane is necessary. I used TransFastTM (Promega, Madison, WI, USA), which is composed of the cationic amphiphilic lipid (+)-N,N-[bis(2-hydroxyethyl)]-N-methyl-N-[2,3-di (tetradecanoyloxy) propyl] ammonium iodid and the neutral phospholipid DOPE (=DioleOyl Phosphatidyl Ethanolamin) (Felgner et al., 1994). In aqueous solutions these compounds form micelles, which can internalize the nucleic acids. Subsequently those spherous lipid compositions fuse with the plasma membrane and release its content into the cytosol.

Two attempts are regularly performed in our laboratory, siRNA-mediated gene knockdown and plasmid-based overexpression, respectively.

4.1. Overexpression

For overexpression, cells are grown until a confluency of about 80% is reached. Volumes and amounts refer to one well of 6-well plate. Subsequently, 2 μg of purified DNA was diluted in 1 ml DMEM without any supplements. Afterwards, 2.5 μl TransFastTM transfection reagent was added to solution and the mixture was vortexed immediately. After 15 minutes incubation at roomtemperature to allow liposome formation, cells were washed with PBS and transfection medium was added to the cells. Cells were incubated at 37 °C in 5% CO_2 for 20 hours, then the transfection medium was replaced for normal cell culture medium. Experiments were performed at least 16 hours later to allow expression of the transfected DNA.

D1ER was kindly provided by Prof. Dr. Roger Tsien (University of California San Diego, CA, USA) (Palmer et al., 2004). AMPK activity reporter (AMPKAR) was purchased

from Addgene (Tsou et al., 2011).

ERAT4.01 was engineered by our group (Vishnu, Khan, Karsten et al., in Press). Briefly, this was achieved by amplifying the ATP-binding box (i.e. ϵ -subunit) of the F_0F_1 -ATP synthase of *Bacillus subtilis* from AT1.03 (Imamura et al., 2009). This ATP-binding domain was subsequently exchanged for the D1 domain (design1 of Calmodulin and M13 sequence) of the ER-targeted Ca^{2+} probe D1ER (Palmer et al., 2004).

For the experiments with HeLa cells with different proliferation rates (Figures 44 and 45) cells were either transfected in 10 cm dishes and subsequently splitted into 6-well plates (20hSC), or directly transfected within 6-well plates (72hSC), respectively.

4.2. RNA interference

RNA interference, or RNAi, is a process by which small RNA single strands of 20-30 basepairs interact with the mRNA of a gene and lead to its degradation (Tomari and Zamore, 2005). In cell culture, this method is used to introduce specific small interfering RNA (siRNA) strands into cells to knockdown the expression of a gene. The protocol is similar to the overexpression protocol, only the DNA is replaced by 2 μ l of 40 μ M siRNA. Cells were then incubated in the transfection medium for 20 hours. 40 to 72 hours later, the transfected cells were used for experiments.

Against Mitochondrial Calcium Uptake 1 (MICU1) a combination of two siRNA's were used as shown (Perocchi et al., 2010; Waldeck-Weiermair et al., 2011). (siRNA1: GCAAUG-GCGAACUGAGCAAUAtt; siRNA2: GCAGCUCAAGAAGCACUUCAAtt) The siRNA against AMP-activated protein kinase (AMPK) was from Santa Cruz Biotechnology (Dallas, Texas, USA).

5. Cell Viability Assay

In a viability assay the ability to metabolize, divide, or migrate of a population of cells within a defined area can approximately be determined. This is either achieved by indicators (Riss et al., 2013), e.g. for metabolic activity, membrane permeability, mitochondrial activity, or genomic assays, or by morphology analysis of image sequences.

5.1. MTT

(3-(4,5-Dimethylthiazol-2-yl)-2,5-diphenyltetrazolium bromide (MTT) is a yellow tetrazole, which is reduced to purple formazan in viable cells. This assay is dependent on the reduced nucleotides NADH and NADPH, hence it reflects the glycolytic rate of a cell population, indicating the number of healthy cells (Berridge and Tan, 1993).

The MTT stock solution (5mg/ml in water) was dissolved in normal cell culture medium (1:10). Cells were washed in 37 °C warm PBS and incubated for at least three hours in 37 °C and 5 % CO₂. Afterwards cells were washed in PBS twice, subsequently lysis solution (0.04 M HCl in isopropanol) was added. The plate was shaken on a microplate shaker at 1400 rpm for 15 min. Then the absorbance at 572 nm and 650 nm was measured on a photometric plate reader (Victor 1420, EG& G Wallac, Gaithersburg, MD, USA).

5.2. Morphological Analysis

For morphological analysis image sequences were acquired as described in results. The viability was then estimated by either measuring the intensity of the series using MetaMorph, or the cell counting option of Cell-IQ[©] Analyser software. A more detailed description can be found in results section.

6. Microscopy

6.1. Microscopes

Most experiments were performed on an *Array Confocal Laser Scanning Microscope (ACLSM)*. The ACLSM is built on an inverse, fully automatic microscope (Axio Observer.Z1 from Zeiss, Göttingen, Germany) that is equipped with a 10x (Plan-Flour 10x/0.3 Ph1), 40x(Plan-Flour 40x/1.3 Oil), and 100x objective (Plan-Fluor 100x/1.45 Oil) from Zeiss (Jena, Germany), a Nipkow-based confocal scanner unit (CSU-X1, Yokogawa Electric Cooperation, Tokyo, Japan), a motorized filter wheel (CSUX1FW, Yokogawa Electric Cooperation) on the emission side, and an acousto optic tunable filter (AOTF, also called piezoelectric device)-based laser merge module for laser lines 405 nm, 445 nm, 473 nm, 488 nm, 515 nm, and 561 nm (Visitron Systems, Puchheim, Germany). Emission was acquired with a charged-coupled device (CCD) camera (CoolSNAP-HQ, Photometrics, Tucson, USA). The microscope is surrounded by an incubator box, to achieve a stable temperature of typically 37 °C. All devices were controlled by VisiView Premier acquisition software (Visitron Systems).

Other experiments were performed on a *Cell-IQ[©] multi-label fluorescence* device (Chipman Technologies, Tampere, Finland). Some experiments were done on a test device, others could be done with kind permission of Univ.-Prof. Dr.rer.nat. Berthold Huppertz (Medical University of Graz, Institute of Histology). The Cell-IQ[©] is a combination of a cell incubator and a microscope. It is connected to a gas supply, I used an atmosphere of 5 % CO₂, 21 % O₂, and 74 % N₂. For phase contrast imaging a LED light source above the substage is used. For fluorescence images, samples were excited with the CellLite[™] multi-label fluorescence module persisting of three LED's (470 nm, 550 nm, and 635 nm).

On the emission side a filter cube is installed, which allows measurement of 525 nm, 593 nm, and 692 nm, respectively. Images were acquired with a CCD camera through a 10x objective (Plan-Flour 10x/0.3 Ph1). Two standard-sized multi-well plates fit into the fully automatic substage within the incubator, as described in Results.

Intracellular measurements of ATP or Ca^{2+} were performed on a *AxioVert inverted microscope* (Zeiss, Vienna, Austria) with a 40x oil immersion objective. The system was equipped with a polychromator illumination system (VisiChrome high speed, xenon lamp, Visitron Systems, Puchheim, Germany), a thermoelectric-cooled CCD camera (Photometrics CoolSNAP HQ, Visitron Systems), a liquid-cooled CCD camera (Photometrics Quantix KAF, Roper Scientific, Tucson, AZ), a light source (440AF21, Omega Optical, Brattleboro, VT), a beam splitter (Optical Insights, Visitron Systems), filter-wheel (MAC 6000/5000, Ludl Electronic Products, Hawthorne, NY) adjustable excitation filters. All devices were controlled by VisiView 2.0.3 (Universal Imaging, Visitron Systems) software (Waldeck-Weiermair et al., 2012).

6.2. Time-lapse Imaging

For live-cell time-lapse imaging, sequential series of images of the cell culture dishes and plates are acquired. Experiments were performed on the ACLSM, or Cell-IQ, respectively. The cell plates were put on a motorized substage, which allows automated movement in x- and y-axis. Varying foci are the effect of slight differences in the plastic of different wells or its content and can be aimed by adjusting the distance between objective and substage, the z-axis.

The period between cycles can be set before inception of imaging. Typically, the cycle time was set to two to 30 minutes, depending on the device used and the assay performed (see Table in Addendum). The time course of live-cell time-lapse imaging was between 30 minutes to about 160 hours.

6.3. Intracellular Ca^{2+} and ATP measurements

Ca^{2+} and ATP in the lumen of the ER were measured in cells transfected with the *Förster* resonance energy transfer (FRET)-based sensors D1ER or ERAT4.01, respectively. Cells were grown on 30 mm glass coverslips. Before the experiments, cells were kept in loading buffer for 15 minutes to 10 hours at room temperature, as indicated. Glucose starvation was induced by pre-incubation in glucose-free loading buffer. Coverslips were subsequently put into a perfusion chamber and imaged using the AxioVert inverted microscope. Here, cells were at first perfused in experimental buffer with Ca^{2+} (2 Ca^{2+} , Table 2). Afterwards,

Ca^{2+} was washed out (0 Ca^{2+} , Table 2) and subsequently Ca^{2+} was released from the ER via treatment with 2 μM of the pore-forming ionophore ionomycin.

	Experimental Buffers	
	2 Ca^{2+}	0 Ca^{2+}
Inorganic Salts		
CaCl_2	222	0
MgCl_2	203	203
KCl	375	375
NaCl	8000	8000
Other Components		
D-Glucose	2000	2000
Hepes	2380	2380

Tab. (2): Experimental buffers (numbers refer to concentration in mg/l). If stated, glucose was replaced mannitol.

7. Image Analysis

Analysis of the image sequence series was performed with four different softwares, VisiView Premier Acquisition software (Visitron Systems, Puchheim, Germany), MetaMorph 6.2r6 (Universal Imaging, Visitron Systems, Puchheim, Germany), Cell-IQ[®] Analyser software (HVD Life Sciences, Vienna, Austria), and Image J, respectively.

Depending on the task, each have certain advantages over the other, see results section. Intracellular Ca^{2+} and ATP measurements were analysed as presented in introduction and elsewhere (Waldeck-Weiermair et al., 2012).

8. Data and Statistical Analyses

For most experiments, data shown represents the mean \pm S.E.M., where the number individual cells or replication of the same condition on the cell population is at least 3 ($n > 3$). In those cases, data analysis was carried out with GraphPad Prism 5.0 employing either analysis of variance (ANOVA) or t-test in case of normally distributed data or nonparametric methods in all other cases ($p < 0.05$ was considered to be significant).

Whenever indicated the number was below 3, mostly 1. Accordingly no statistical analysis was performed with those experiments. Graphs were produced using GraphPad Prism 5.0.

III. Results

The results of my diploma thesis are presented in three parts.

The first part is a description of the establishment of the long-term live-cell imaging assays. This part includes a short literature research about the established assays in comparison with my results (Section 1).

In the second part, I present morphological peculiarities that were observed during live-cell imaging experiments (Section 2).

In the third part, I present a selection of my results, acquired with the established assays, focussing on the effect of nutrient and serum starvation and the mitochondrial Ca^{2+} uptake on viability, proliferation, and migration of cells (Section 3 and 4).

Finally, I show correlations between the long-term live-cell imaging with organelle Ca^{2+} and ATP measurements (Section 5).

1. Establishment of Life-Cell Imaging Assays

Here, I present a brief overview of the aspects that had to be considered in the course of establishing the long-term live-cell imaging assays for proliferation, viability, and migration. The protocols presented are intended to be guidelines for use on the systems tested, i.e. a VisiView controlled array confocal laser scanning microscope (ACLSM) and a Cell-IQ[©].

1.1. Confluency

The first step of my project was to establish conditions under which subsequent experiments could be performed, i.e. viability and migrational assays, respectively. This included testing for various medium compositions (see below) and cell confluencies for the various cell types used.

For the EA.hy926 endothelial cells, HeLa cells, and INS-1 cells the number of cells required to plate in order to achieve a specific confluency was known, and I relied on this information. Intuitively, I expected a fully confluent cell layer to be optimal for a migrational assay, like a wound-healing (WH) assay by use of inserts or by scratching, because the cells need to have reached a certain density, which leads to a directed migration towards a gap.

To the contrary, a proliferation analysis, in which the division rate is calculated, sub-confluent layers seemed to be superior, as the cells need to spread in order to divide properly. Additionally, cells are known to change some properties, if their vicinity becomes too crowded. For example, endothelial cells are known to reduce division rate and

gene expression if they grow too confluent, a process called growth arrest (Fishman et al., 1975; Castellot et al., 1981). HeLa cells on the other hand have lost this ability (Zhang et al., 2012).

1.1.1. Correlation between Endothelial Cell Confluency and Cell Number

For EA.hy926 cells, I measured the growth after plating defined amounts of cells by determining the confluency after 24 hours and 48 hours afterwards using Cell-IQ Analyser, respectively (Figure 6). The amounts of cells shown in A and B refer to one 35 mm cell culture dish and were diluted in 2 ml of medium. I found, that those cells plated at concentrations of 4×10^5 to 6×10^5 were already almost totally confluent at the first day (A, left panel). Accordingly, at the next day, the cells were not considerably proliferating until day two (B, left panel, increase in confluency of 12.5%, 8.8%, and 3.4%, respectively). On the other hand, the lower confluent cells (10^5 to 3×10^5 cells) were proliferating, shown by an increase in confluency of 37.7%, 39.7%, and 31.8%, respectively (A and B, right panels).

As cell confluency cannot go beyond 100%, I also counted the number of cells for each cell concentration at both days. By this, I could detect if the cells were in a growth arrest

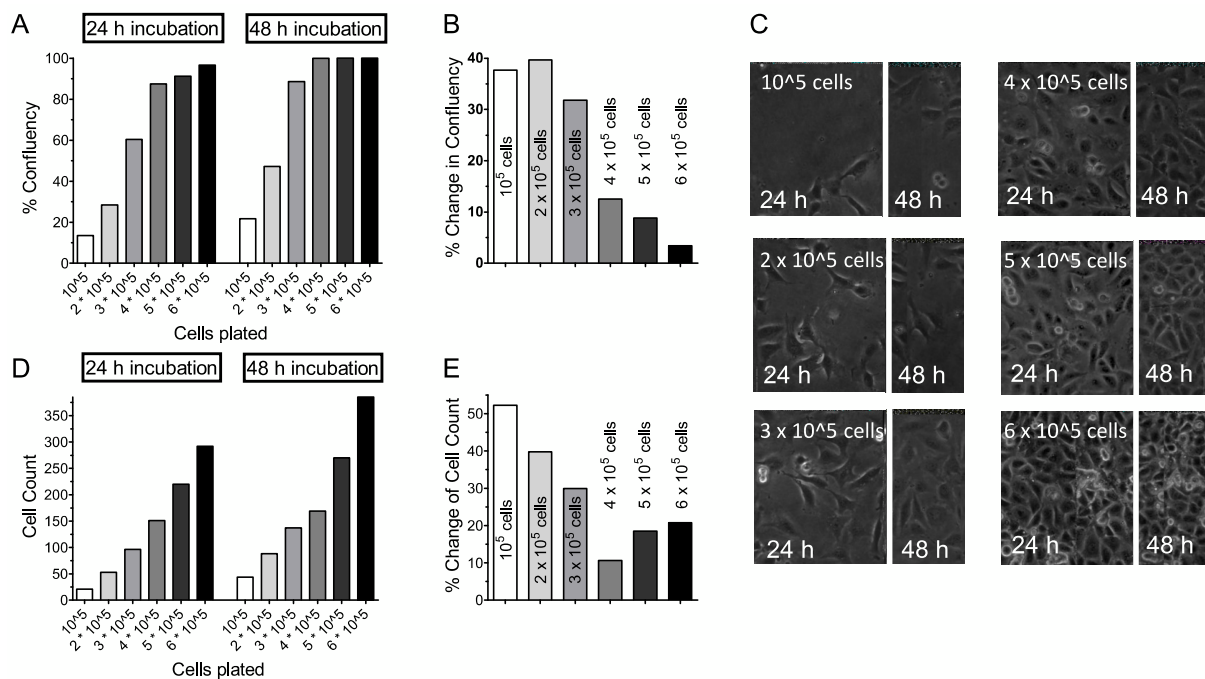


Figure (6): **A:** Determination of EA.hy926 cell confluency 24 and 48 hours after plating 10^5 to 6×10^5 cells into 35 mm dishes using Cell-IQ Analyser. **B:** Corresponding determination of the change in confluency. **C:** Representative images of EA.hy926 cells plated at different concentrations (10^5 - 6×10^5 cells as indicated) 24 hours or 48 hours after plating. **D:** Manual cell count of the same images. **E:** Corresponding determination of the change in confluency. (n=1)

state or still proliferating. The cells were counted manually. I found, that the EA.hy926 cells had an elevated cell number for all cell densities plated after 48 hours compared to 24 hours (D). The relative change of the cell number between day one and day two was more pronounced for the lower cell concentrations, with an increase of the count of 52.3% for 10^5 , 39.8% for 2×10^5 , 29.9% for 3×10^5 , and 10.7% for 4×10^5 . Those first four conditions gave the impression, that a growth arrest was indeed occurring. However, the highest confluencies of 5×10^5 and 6×10^5 cells showed a slightly higher increase in cell number of 18.5% and 20.8%, respectively, limiting the conclusion of a total growth arrest.

1.1.2. ATP Sensor-Transfected HeLa Cells Proliferate Slower than Ca^{2+} Sensor-Transfected HeLa Cells

For HeLa cells, I did not calculate exact amounts to be plated in order to reach a certain confluency. Rather, I referred on the experience of our cell culture, which worked without any major difficulties. However, when I estimated the confluency of HeLa cells plated with the aim to reach certain confluencies of 10%, 20%, 40%, 60%, and 100% one day later with Cell-IQ Analyser, I found slight variations (Figure 7). All the reached confluencies

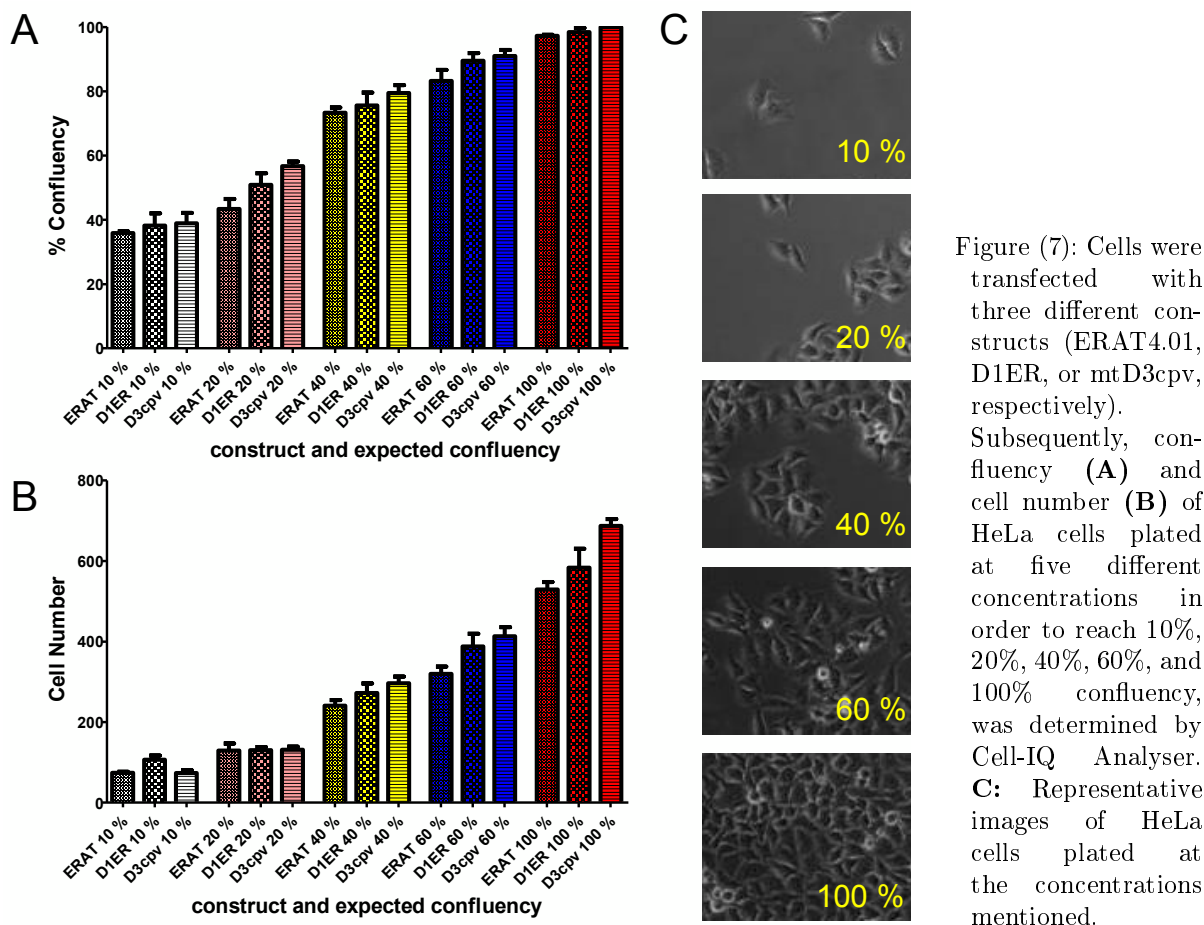


Figure (7): Cells were transfected with three different constructs (ERAT4.01, D1ER, or mtD3cpv, respectively). Subsequently, confluency (A) and cell number (B) of HeLa cells plated at five different concentrations in order to reach 10%, 20%, 40%, 60%, and 100% confluency, was determined by Cell-IQ Analyser. C: Representative images of HeLa cells plated at the concentrations mentioned.

were about 20% higher than expected (Figure 7 A). The three different conditions of each confluency refer to three genetically encoded *Förster* resonance energy transfer (FRET) based sensors, that were transfected into HeLa cells prior to replating. Experiments with those sensors are presented in the final section of the results.

Interestingly, it appeared that cells transfected with the different constructs were proliferating with a slightly different pace upon transfection. Seemingly, for all conditions the mtD3cpv and the D1ER transfected cells were more confluent than the ERAT4.01 transfected cells. The same tendency was seen by determining the total cell number (Figure 7 B) instead of the confluency. Noteworthy, ERAT4.01 is an ATP sensor, while the former two are Ca^{2+} sensor. This might be seen as an indication, that chelating ATP within the ER can hamper the proliferation rate of cells. Further research will be required to elaborate this note.

Similar to the EA.hy926 cells, I did not observe a growth arrest, indicated by the three conditions at 100% confluency (Figure 7 A, red bars) that differed in their total cell count (Figure 7 B, red bars).

1.2. Proliferation

Depending on the definition, cell proliferation refers to both the rate of division of a cell population and the increase in cell size (Bast et al., 2000; Enesco and Leblond, 1962). Those two processes are not the same, but act in concert in most of the cases, with a cell first growing in size and subsequently dividing into two similar daughter cells. Mostly, proliferation is determined by (fluorescently) labeling cells and subsequent detection of labeled cells (Lyons and Parish, 1994).

While both processes can be separated analytically, the basic set-up of a proliferation assay is the same. The cells are plated in order to achieve a subconfluent layer of cells, ideally between 20% and 50%. Proliferation was either quantified by plotting changes in confluency or cell number (Figure 6 and 7). With cells that were too confluent at the start of the experiments, differences in the rate of proliferation were less obvious or even undetectable, if the change in confluency was shown, but changes in the total cell number were still observable. After the cells were fully adhered (at least 20 hours after plating), the culture plates were imaged under the respective microscope. The acquired images could then be viewed and analysed (e.g. Figure 38 D and E).

1.3. Division

A dividing cell can be easily differentiated from a non-dividing cell, both morphologically and molecularly (Griffiths et al., 2010). Among other methods, the latter can be done by analysing the activation pattern of several marker proteins, e.g. cyclins or cyclin-

dependent kinases (CDK's) (Beemster et al., 2002; Schnittger et al., 2002), measuring DNA content (Kittler et al., 2007), or by determining the state of the cytoskeleton (De-grassi and Tanzarella, 1988).

Ideally, during mitosis two daughter cells derive from one mother cell (exceptions are presented in the chapter "Morphological Peculiarities", Figure 26), whereby specific morphological changes occur. Non-dividing cells appear as differently shaped objects, with various appendages and clearly distinguishable nuclei and organelles (see Figure 35). Additionally, they show more or less directed movements. Obviously, in different cell lines the cellular morphology appears differently.

In contrast, dividing cells are much more uniform, even different cell types of various species show few variations, mainly as a matter of size, in the sense that a small cell turns into a small dividing cell. In phase-contrast imaging, dividing cells look like a very bright ring surrounding a dark center (see Figures 26 and 27 B). Neither a nucleus nor other organelles can be perceived and movement seems passive, if any occurs at all. If the magnification is high enough and sequence fast enough, it is even possible to differentiate the mitotic phases (not shown).

After about 20 min, the bright ring becomes uneven, until two distinct rings clearly appear. Subsequently, the two rings start to spread, until two daughter cells are formed. As mentioned above, I compared the two morphological analyses techniques to estimate the rate of cell division.

With intensity measurement, a dividing cell appears as a transient peak in intensity (Figure 19 A). Thus, it can be used to compare small ROI's, but within an entire population, the signal is in fact negligible. On the other hand, by morphology analysis of the Cell-IQ Analyser a clear and realistic quantitation could be achieved (Figure 38).

1.4. Cell Death and Viability

Classically, cell death was classified into programmed (apoptosis) (Kerr et al., 1972) and premature (necrosis) cell death (Wylie et al., 1980). However, in recent years an ongoing debate occurred about the classification of cell death (Schwartz et al., 1993; Galluzzi et al., 2011; Edinger and Thompson, 2004). Particularly, some forms of necrosis appeared to be programmed as well (Proskuryakov et al., 2003). Additionally, other forms of programmed cell death were introduced, e.g. autophagic programmed cell death (Tsujiimoto and Shimizu, 2005), or necroptosis (Teng et al., 2005).

In a viability assay the ability of single cells or cell populations (or tissues) to remain viable, i.e. to thrive, is determined. The viability and cell death rate of a cell population inversely correlate, hence both reflect the other. A multitude of viability assays exist. The first attempts were performed using dyes like trypan blue, which selectively stains dead

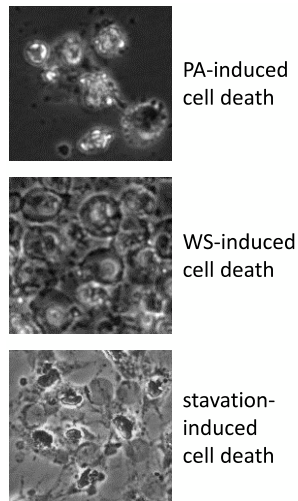


Figure (8): Depending on the experiment and mode of death induction, a dead cell can appear morphologically distinct from another dead cell of the same type of cell. Cell death induced of EA.hy926 cells by palmitic acid (PA, *top panel*) appears as bright round and detached objects, that tend to form conglomerates, while death induced by the Crataegus extract WS-1442 (*middle panel*) and starvation-induced cell death (*bottom panel*) of the same cell type appears as cells with differently looking membrane blebs.

cells (Wainwright, 2010) Later on it was identified, that some altered cells yield a characteristic pattern in gel electrophoresis of nuclear DNA (Williamson, 1970; Chen et al., 1996). This process was later found to be a hallmark of apoptosis (Kerr et al., 1972), mediated by the Caspase-Activated DNase (CAD) (Enari et al., 1998). The DNA fragmentation is also detected by the terminal deoxynucleotidyl transferase dUTP nick end labeling (TUNEL) assay (Gavrieli et al., 1992). Other viability assays are based on dyes like trypan blue mass spectrometry (Lindner and Seydel, 1983).

Another type of viability assay is based on the metabolic activity of the cells, e.g. luminescence mediated MTT assay (Mosmann, 1983; Berridge et al., 2005). Finally, several fluorescence-based assays exist, e.g. 7-Aminoactinomycin D (Lecoeur et al., 2002) or propidium iodide (PI) staining (Lecoeur, 2002). As those methods cannot clearly distinguish between different types of cell death further progress was made to differentiate necrosis from apoptosis, e.g. by combined use of PI and Annexin A5 staining (Baskić et al., 2006). Of note, apart from being molecularly distinct, various cell death types can also appear phenotypically different (Figure 8.)

In my microscopic viability assay, similar to the proliferation assay, cells were plated at least 20 hours before the experiments started. In those assays, a higher albeit still subconfluent cell density was preferable, as this reduced the effect of chance cell death events on the overall outcome. Before or during the experiments the cells were exposed to the respective conditions. Finally, the image series were acquired and subsequently analysed (e.g. Figure 35).

1.5. Migration

Cellular migration (Vicente-Manzanares and Horwitz, 2011; Kramer et al., 2012) is crucially involved in many physiologic (e.g. angiogenesis (Folkman and Shing, 1992), immune

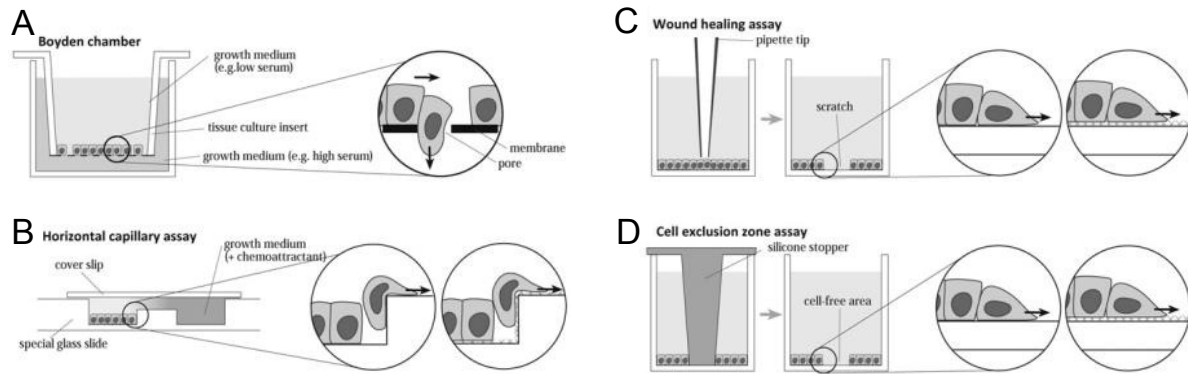


Figure (9): Examples of migration assays. **A:** Boyden chamber assay and **B:** Horizontal capillary assay are chemoattractant assays. **C:** Wound-healing scratch assay and **D:** Cell exclusion zone assay are non-chemoattractant assays. Adopted from (Kramer et al., 2012).

cell migration (Luster et al., 2005), wound-healing (Shaw and Martin, 2009), or neurogenesis (Hatten, 2002)) and pathologic conditions (e.g. invasion (Friedl and Wolf, 2010) or metastasis of tumors (Nguyen et al., 2009), or auto-immune diseases (Luster et al., 2005)). All migration experiment I performed were done with endothelial cells, hence I concentrate on these vasculature forming cells.

The process by which blood vessels are formed *de novo* is called vasculogenesis, the subsequent formation from preexisting ones is called angiogenesis (Folkman and Shing, 1992). Several factors and their corresponding receptors regulate angiogenesis and endothelial differentiation in a complex interplay, involving both genetic and environmental aspects (Fraisl et al., 2009; Atkins et al., 2011). The exact pattern of activation and inhibition factors is only roughly known (Distler et al., 2003), however, some growth factors, like VEGF or bFGF have been identified to play a crucial role. In adults, angiostatic mediators predominate, hence no angiogenesis occurs under physiological conditions. To the contrary, during e.g. embryogenesis, wound healing processes, or tumorigenesis the angiogenic effectors outweigh the antagonistic stimuli, inciting ECs to proliferate and migrate (Carmeliet and Jain, 2011).

Pathologies occur on both ends of the spectrum. While for example in chronic non-healing wounds angiogenesis is reduced (Blakytyn and Jude, 2006), in tumorous tissues angiogenesis is increased (Folkman, 2002). If a tumor reaches a threshold size, which prevents nourishment of the entire neoplasia, some of its cells release pro-angiogenic factors due to oxygen and nutrient deprivation. The subsequent uncontrolled angiogenic state results in an increase of supply to the tumor cells and also elicits a higher probability of metastasis. Thus, one pharmaceutical therapy in oncology is to inhibit angiogenesis (Bridges and Harris, 2011; Pandya et al., 2006). A long list of substances with angiostatic ability (e.g. the endocannabinoid anandamide (AEA) (Pisanti et al., 2007; Waldeck-Weiermair et al., 2008)) is described.

Several methods to estimate the migratory rate of cell populations exist (Kramer et al., 2012). Briefly, two general attempts exist, chemoattractant and non-chemoattractant assays. In chemoattractant assays, cells are grown in one type of medium, and are connected via pores, which are slightly smaller than the cells, to another medium. This can either contain more serum, or compounds, which either attract or repel cells. The simplest form is called transwell migration assay or Boyden chamber assay (Boyden, 1962), which is a classical end-point assay, as cells that migrated through the pores are identified at a certain time after the experiment started (Figure 9 A). Another form is the capillary chamber migration assays (Zigmond, 1988; Zicha et al., 1991). Here, two chambers placed on a small dish are interconnected via a narrow bridge (B). One of the chambers is filled with medium containing cells, the other with no cells and an attractant. Subsequently, the migration of the cells through the medium filled bridge can be determined live using microscopy (Chaubey et al., 2011) or also as an endpoint assay.

In my diploma thesis, I compared two non-chemoattractant assays, the woundhealing scratch (C) and cell exclusion zone assay (D) using cell culture inserts, respectively. Both have been used to study the migration of various cell types (Zhang et al., 2011; Wu et al., 2012; Inoue et al., 2007; Omelchenko and Hall, 2012; Fougerat et al., 2012). Both methods differ in their setting, the analysis and validity are akin, though.

In a **scratch assay** the cells are grown on a cell culture dish until complete confluency is reached. Before the experiment is started, a wound is scratched onto the confluent layer of cells using a 200 μ l pipette tip (Lampugnani, 1999; Liang et al., 2007; Cory, 2011). The cells are then washed at least twice with phosphate buffered saline (PBS) to remove

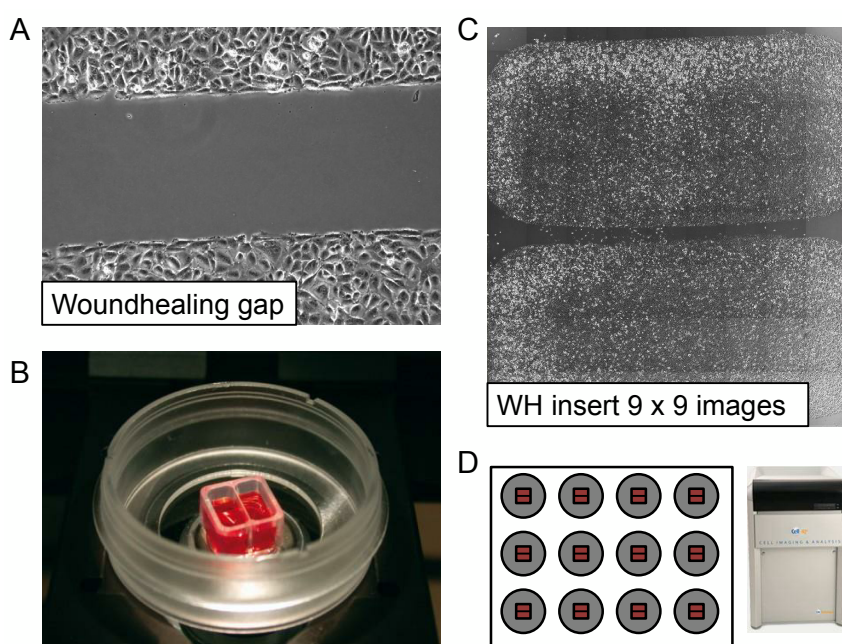


Figure (10): Cell Exclusion Zone Insert from ibidi©. **A:** Single image of the gap before migration induction. **B:** Image of WH insert in a 35 mm dish (from www.ibidi.com) **C:** 81 aligned images yielding the entire cell growth area of an WH insert, recorded with Cell-IQ. **D:** In a Cell-IQ up to 24 wells (2 x 12-well plate) can be recorded simultaneously.

cellular debris from the culture dish.

A similar attempt can also be performed using a **cell exclusion zone insert** from ibidi®. These are silicon based cell culture inserts with two chambers, separated by a 500 µm wall. The inserts adhere on plastic dishes by applying mild pressure, but are incompatible with glass dishes. Each chamber is then filled with 70 µl cell solution, so that the cells can only grow within the predefined area inside the chambers. I found, that plating of about 18.000 EA.hy926 cells - about 2.8×10^5 per ml - in each chamber of an insert resulted in a confluent cell layer after 24 hours of incubation. The next day, the insert is removed and the cells are washed with PBS to remove debris and non-attached cells. Especially during my first attempts, I often observed several cells which began to attach at the beginning of the experiment due to insufficient washing. In the most drastic examples this led to a considerable reduction in the size of the gap, which interfered with the pace of migration and more importantly with the semi-automatic analysis.

In both cases, afterwards cell culture medium or buffer including a growth stimulus (serum) is added to the cells. Then regions of interest (ROI) are chosen so as to contain the gaps between the cells and an image series of the migrating cells is acquired.

1.6. Caveats

During the task of establishing long-term live-cell imaging assays, one inevitably faces problems and drawbacks. I decided to concentrate on the major factors and not to enlist every single hindrance with its solution, as this would go beyond the scope of this work. Additionally, a lot of those problems were device-specific and would thus not be helpful in different settings.

1.6.1. Contamination

In the biological sciences, the term contamination is defined as the accidental introduction of a foreign substance into an experimental sample. If the substance is a microorganism (mostly bacteria or fungi) with the ability to multiply, it can easily outgrow the population of experimental cells and, thus, frustrate the outcome of the experiment. This is the sort of contamination I talk of.

Our generally used cell culture medium is filtered and antibiotics and antifungals are present which typically prevent contamination. To the contrary, most of the experimental buffers used for experiments in the temporal range of minutes lack antibiotics and antifungals. For those experiments, this is no detriment, since the period is usually too short for substantial microorganisms to grow. However, when using these experimental buffers for experiments that last several hours (Figure 37), this can render a drawback.

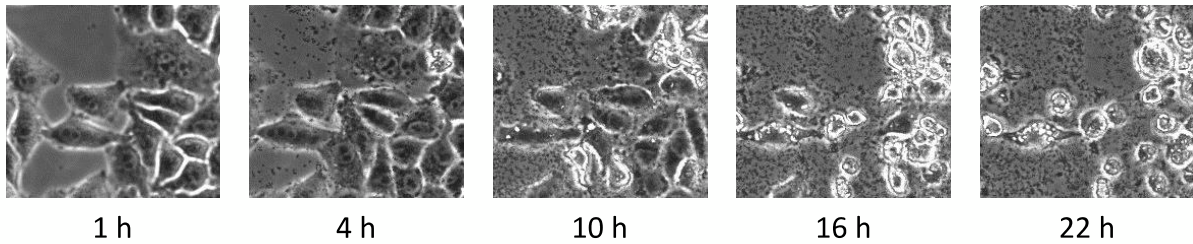


Figure (11): Time course of an experiment where a bacterial contamination occurred. HeLa cells were kept in buffer without antibiotics. Already after about one hour, the first bacteria (small black dots) could be observed, after 4 hours bacteria were ubiquitously present, in the final images almost only bacteria were seen.

Obviously, the solution is simple: Filter the buffers before usage and add antibiotics and antifungals to them. While the first operation is - apart from consuming time - free of adverse effect, the latter holds a drawback in itself. Antibiotics can effect the cellular DNA and protein synthesis or even metabolism (Kuhlmann, 1995). Hence, in some cases it appears sensible to limit the use of such substances, e.g. when measuring cell proliferation. In all but a few experiments, however, medium with antibiotics and antifungals was used. The lack of antibiotics and antifungals in cell culture medium does not necessarily lead to a overwhelming rate of contamination, if careful cell culture handling is applied, as evidenced by the standard application e.g. during transfection.

From my personal experience I think, that use of antibiotics and antifungals can be reduced during long-term live-cell imaging, if the buffers are filtered and cell culture procedures are carefully applied. Nonetheless, eventually contaminations are inevitable (Figure 11). As long as those rapidly proliferating germs remain the exception rather than the rule one has to live with it.

1.6.2. Various pH Buffers do not Influence Cell Proliferation

What kind of buffers and media can be used for long-term live-cell imaging mainly depends on the system and its gas supply. Essentially, this reflects the methods by which changes in the pH of the media are buffered. There are two means by which the pH in cell cultures is buffered, so that the medium remains mildly basic at a pH of around 7.4, which is ideal for cellular growth. Firstly, the *bicarbonate/CO₂* system is the standard pH buffering system in cell culture (Figure 12, straight lines and filled bars). Bicarbonate is a weak buffer with a pKa of 6.1, which seems thus not ideal as a physiological buffer system. However, in the presence of high levels of atmospheric CO₂, which is in equilibrium with dissolved CO₂, bicarbonate is suitable to maintain the pH in the physiological range.

An alternative is the use of bicarbonate/CO₂ system-independent buffers like *HEPES* (N-2-hydroxyethylpiperazine-N'-2-ethanesulphonic acid) (Figure 12, dotted lines and unfilled

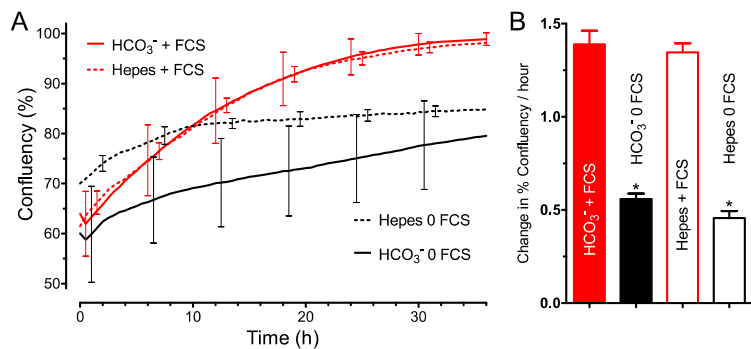


Figure (12): Comparison of HeLa cell growth incubated in bicarbonate (continuous lines) or Hepes (dotted lines) buffered medium ($n=3$). **A:** Shown is the time course of the confluency. **B:** Bar charts indicate the inverse slope from A in pixels per hour for the first 12 hours (vertical dotted line in A). * $p < 0.05$ FCS absence (black lines) vs. FCS presence (red lines).

bars). HEPES has a pK_a of 7.66, but has the disadvantage of being toxic to cells at a relatively low concentration.

Accordingly, most commonly the bicarbonate/ CO_2 system is used in cell culture. Thus, whenever possible this system should be preferred for long-term live-cell imaging attempts. So far, I was not able to apply the CO_2 control in the incubator of the array confocal laser scanning microscope (ACLSM) due to insufficient sealing. On the other hand, the Cell-IQ[®] is provided with an intrinsic incubator including a gas supply. Therefore, when using a system with a operating gas supply, media with the bicarbonate/ CO_2 system should be applied, in other cases organic buffers like HEPES are to be chosen.

However, in an exemplarily experiment in which the cellular proliferation of both pH buffered media was compared in combination with (red) or without (black) fetal calf serum (FCS) starvation, I did not find any difference in the proliferation rate.

1.6.3. Choice of Cell Culture Dishes or Plates

As mentioned previously, the choice of cell culture dishes or plates depends on the system on which the experiment is performed and the type of the assay. On the ACLSM's stage multi-well plates can neither be fixed in a way, that every well can be reached by the objective, nor can a focussable image be acquired. Because of that, I was limited to two 35 mm cell culture dishes or small eight-well slides. For migration experiments, up to four wound-healing inserts can be placed in each 35 mm dish. Recently, I was able to modify the stage to allow use of six 35 mm dishes simultaneously, comparable to a six-well plate (Figure 13 A), i.e. 24 wound-healing inserts.

In the Cell-IQ[®] system the use of two standard multi-well plates is possible (Figure 13 B). Typically, 6-, 12-, 24-, 48-, and 96-well plates are available, thus, theoretically 192 different positions could possibly be observed during one experiment. However, such a great number of different positions was not feasible, especially if more than one position per well was chosen, due to time constraints. Depending on the needed accuracy of the automatic focus, each image acquisition requires between 20 seconds and 1 minute, easily summing up to a couple of hours for 192 positions. Such a long delay between acquisition

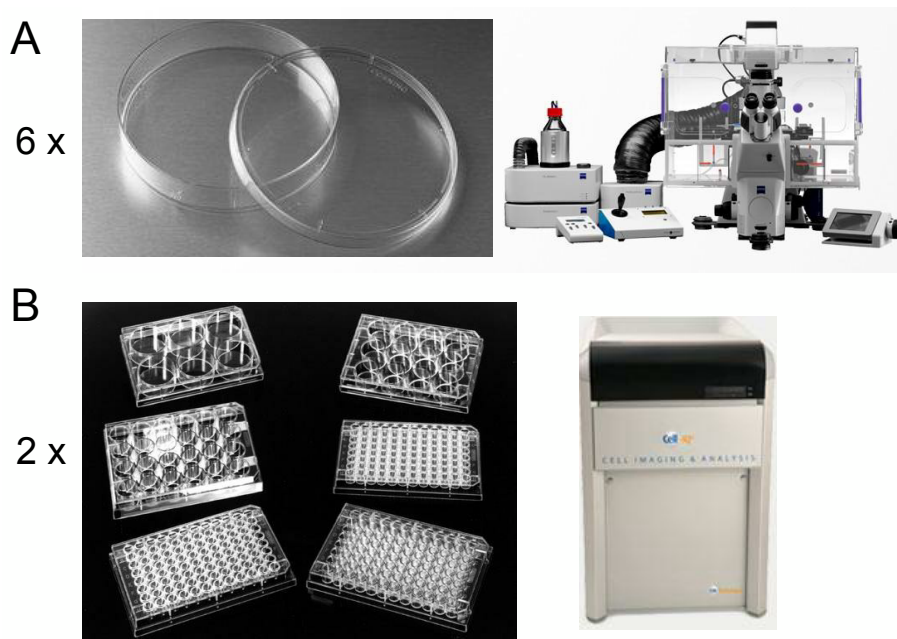


Figure (13): Depending on the system, different plates and dishes must be used. **A:** On the ACLSM up to six 35 mm dishes can be imaged simultaneously (but for most experiments of this thesis only two dishes were applicable). **B:** In the Cell-IQ two multi-well plates can be imaged simultaneously, yielding a theoretical number of 192.

of the first and the last image results in a hardly comparable initial situation. Another factor that led to the dismissal of 96-well plates was the occurrence of a relatively strong meniscus on the edge of each well. I tried the adaptability of twelve-, 24-, and 48-well plates. Typically, on twelve-well plates the cells showed an even distribution, while on the 24-well and especially the 48-well plates, the cells possessed a more polarized distribution pattern, with cell accumulations on the edges and in concentric circles. Therefore I mostly relied on twelve-well plates (still up to 24 positions during each experiment) or 24-well plates if more conditions were needed.

Another factor is the ability to use fluorescence. For whole cell stainings, any tested dish or plate could be used, although of course for long-term experiments low light intensities should be applied, to prevent bleaching and phototoxicity. If subcellular structures, especially with low fluorescent intensity, are to be observed, in preliminary experiments (not shown) I found, that most of the plastic dishes were not feasible, but glass labware was preferable.

1.6.4. Intense Light Reduces Endothelial Cell Migration

Light, especially intense light, is undoubtedly a source of energy. In plants it is used for the anabolism of complex carbohydrates, e.g. sugars, from carbon dioxide during photosynthesis. But also animal cells respond to light. Apart from the obvious examples of sensory neurons in the retina and the melanocytes in the skin, other cell types are also believed to be at least to some extent light-dependent. Namely in the retinal vasculature, endothelial cells were recently shown to respond to light by regulation of expression of vascular endothelial growth factor (VEGF) (Rao et al., 2013). Another example was shown

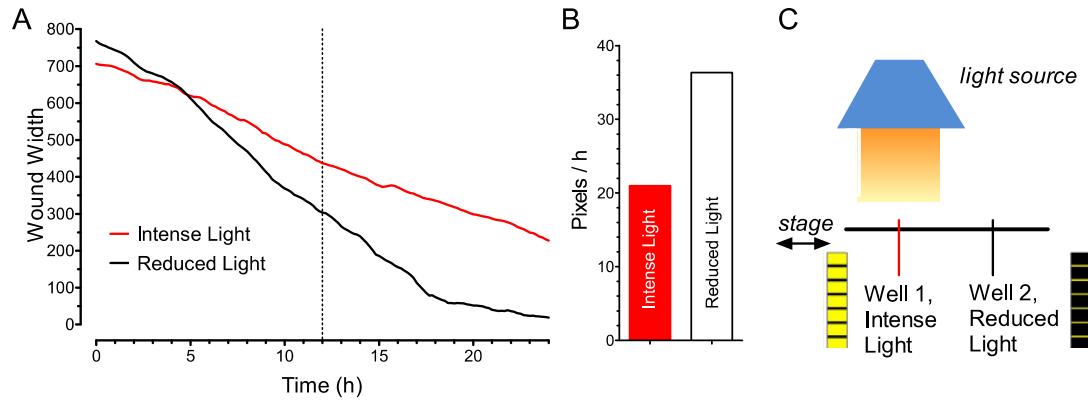


Figure (14): Pace of migration in cell exclusion zone assay depends on the intensity of the applied light ($n=1$). **A:** Gap closure shown as decline in gap width. Cells were either exposed to intense light (red line) or reduced light (black line). **B:** Bar charts indicate the inverse slope from C in pixels per hour calculated for the first 12 hours of the experiment (vertical dotted line in A). **C:** Illustration of the experimental setup. The first position (Well 1, Intense Light) is initially imaged with light present. Afterwards, the stage moves towards position 2 (Well 2, Reduced Light) and makes an image. At the end of each cycle, the stage moves back to position 1 and remains there. The light is turned on throughout the entire experiment, thus position 1 is exposed to substantially more light (represented by the yellow and black bars).

in zebrafish, where light could suppress rate of mitosis and cell proliferation (Tamai et al., 2012).

The ACLSM is equipped with an adjustable light source. Generally, the higher the magnification and resolution the more intense light is required to achieve reasonable contrast. During my first experiments, I was not attending to this. Then, when I ran the first wound-healing assays, I soon realised, that the first ROI always yielded a slower migration capacity than the same treatment condition at another ROI (Figure 14). The reason for this, I found in the way the acquisition software VisiView routinely controls the ACLSM. Before the automatic acquisition starts, I defined the ROI's, one or more for each condition and the temporal resolution (or timepoint, TP). When acquiring the image series, the stage is automatically moved above the objective to each ROI in the same order as previously defined. After one image at each ROI was acquired, the stage remains at ROI 1 (Figure 14 C, red line) until the next TP is reached, when the next round of image acquisitions starts. In the meantime, however, the light remains powered. Thus, position 1 is exposed to considerably more light than any other position. In support of this observation, the ROI's in the vicinity of ROI 1 were more influenced by the light, than those that were farther away (not shown). Finally, this was solved by several adjustments in the settings of VisiView and the microscope itself, whereby the light was turned off during the countdown towards the upcoming TP.

1.7. Establishment of Analysis Techniques

In my thesis, I compared two visual analysis techniques of long-term live-cell imaging series, intensity and morphology analyses, respectively. Primarily, those were used to estimate the viability and the rate of cell division. But also other - sometimes unexpected - outcomes could be observed, like the synchronous appearance of vacuoles upon treatment with the phosphoinositide-3-kinase (PI3K) inhibitor Wortmannin (Figure 27). I should not forget to mention, that both techniques result in an estimation of the analysed processes and do not result in exact numbers. Here, I describe both techniques, including advantages and limitations and I will ponder various applications.

1.7.1. Morphology Analysis

The morphology analysis was rendered with the Cell-IQ Analyser software (chipman technologies, 2004). The software can differentiate between various classes of cell types, based on morphological differences, like the size, shape, brightness and others, although, to my knowledge the exact algorithm is not published by the manufacturer (Toimela et al., 2008). As a general rule, the manufacturer states, that anything that can be differentiated by the eyes of a specialist can potentially be differentiated by the program's algorithm, given enough teaching, i.e. addition of sample images to a database.

In a first step four values can be set, so that the most possible number of objects are recognized as such (Figure 15). 1.) segm grad threshold, a traditional threshold, in the sense that small values result in more positive but also more false positive results, respectively. 2.) minimum cell distance. 3.) maximal cell diameter. 4.) cell symmetry. According to my experience 1.) and 4.) have only limited influence on the number of positively recognized objects, whereas the size parameters 2.) and 3.) are of major impact.

Since various cell types differ in size and morphology, those values need to be adjusted for every cell type observed. But also the image quality needs to be taken into account, as on lower quality images - i.e. with a higher binning - each pixel represents a larger area, which changes the relative size of each object. By using those four values, the program analyses each image and creates a dot where an object was recognized on a copy of the raw image. As with most tests, sensitivity and specificity rarely both reach 100%, as setting the values in a way that no false negatives occur, automatically leads to more false positives or multiple positives (i.e. one cell is depicted with more than one dot). Accordingly, if the aim is to increase sensitivity, then the specificity decreases. As I will show, false positives can be neglected, hence a tradeoff between recognizing too many multiple positives and too few objects has to be made.

Once a reasonably accurate number of objects was recognized, I defined various classes,

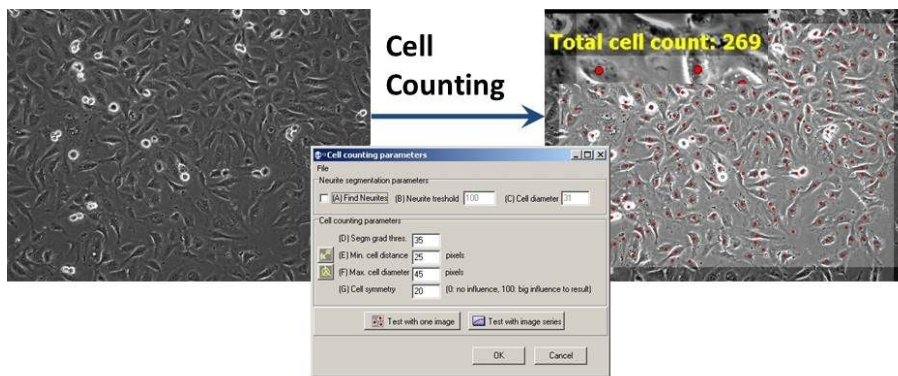


Figure (15): Cell-Counter of Cell-IQ Analyser. The cell counting parameters need to be optimized to receive good sensitivity and specificity.

namely "viable cells", "altered cells", "dividing cells", "dead cells" (in fact, a differentiation between more than one kind of cell death was also successfully tested, not shown), and possibly others such as "many vacuoles" (Figure 27). If not excessively present, false positives display only a minor struggle, since they may be defined as an additional class of objects, I commonly defined it as "trash". Alternatively, the cell division rate can be estimated by simply using the cell counter. An increase in cell count during the course of an image series unambiguously reflects a certain division rate.

Following, I manually created a sample library with representative images of each class (Figure 16), which is later used by the analyser to create a protocol for the algorithm. This is the most time intense process of the whole analysis, because the efficiency can only be tested by creating a new protocol and using it on one image. Both processes take time, and can easily reach the range of minutes simply for rendering one protocol, especially if the number of classes and objects in the sample library increases.

Once most of the objects were defined as the objectively right class on one image, the same protocol needs to be tested on other timepoints. Although one might expect that images acquired under similar conditions should result in comparable outcomes, this is not necessarily the case, which led to some frustration during my first attempts of analyses.

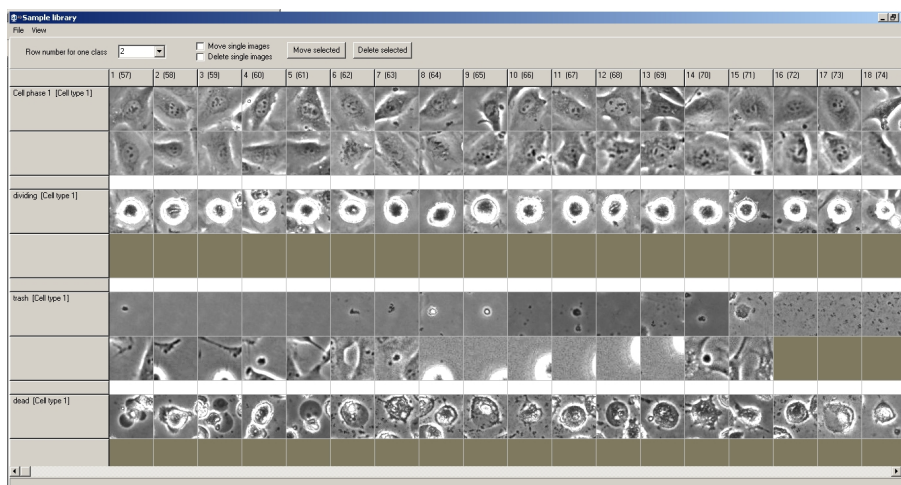


Figure (16): Manually chosen images are included into a sample library. Those are used by the Cell-IQ Analyser to render a protocol, which automatically calculates the number of each cell type defined for every image of a series.

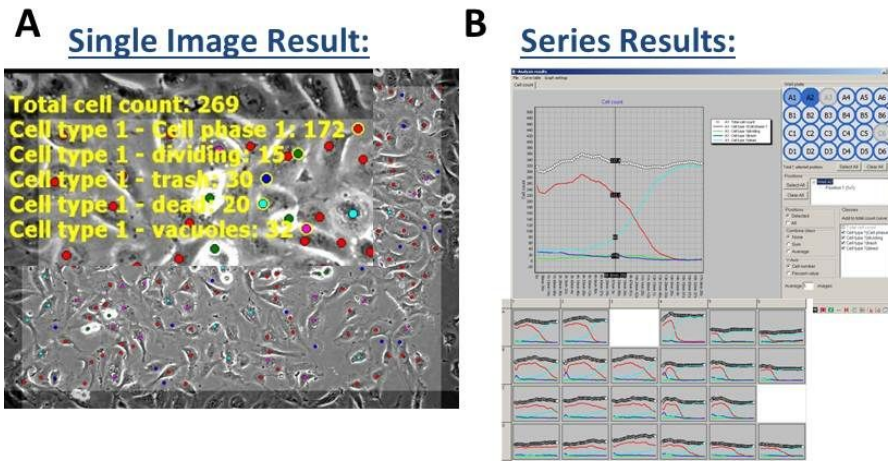


Figure (17): **A:** Single image with five different defined cell types. **B:** Graphs of CellCounter and the course cell type distribution during image series on 24 wells.

Therefore, more representative images needed to be included to the sample library, also called "teaching" the program. The more classes were included, the more elaborate the sample library needs to be and triple-digit samples for one class are no rarity. Fortunately, the protocols can be reused, when the same type of cell is observed at another experiment, although this always requires adjustment, especially the same type of cell might appear morphologically distinct in several setups (e.g. "dead" cells, Figure 8).

Nonetheless, the Cell-IQ Analyser regularly makes individual errors, e.g. a seemingly dead cell is recognized as a dividing cell, or vice versa. This is due to the different analyses natures of the human brain and a computer. While the former recognizes structures automatically - neuroscientists may excuse this simplification - as objects, the latter peruses an image on a pixel by pixel basis. Hence, each object influences its vicinity and may lead to a misplacement of other objects, albeit this can be reduced by teaching the analyser ever better. This influenced the outcome especially in the experiments where the majority of cells transiently acquired vacuoles. A cell with "vacuoles" is brighter than a regular "viable" cell, as are "dividing" or some types of "dead" cells. Hence, a misplacement can more easily occur when the majority of cells are brighter.

In addition, the algorithm analyzes a sequence in an image by image manner, thus it is incapable to adapt any given time point according to previous or posterior events. A human brain as analysing device can jump back and forth through the series, which enables it in most cases to differentiate between a possibly dividing or dead cell, through the fact that a cell division results in two daughter cells, or at least one multi-nucleated cell, whereas a dead cell remains rather static. This note was also useful in the intensity analysis (Figure 19).

Finally, the program calculates the number of objects for each class present at every time-point of the sequence, resulting in a graph and a dotted image series, whereby each class is represented by a differently coloured dot (Figure 17).

Afterwards, the graph can be exported to Excel. This data can then presented in various

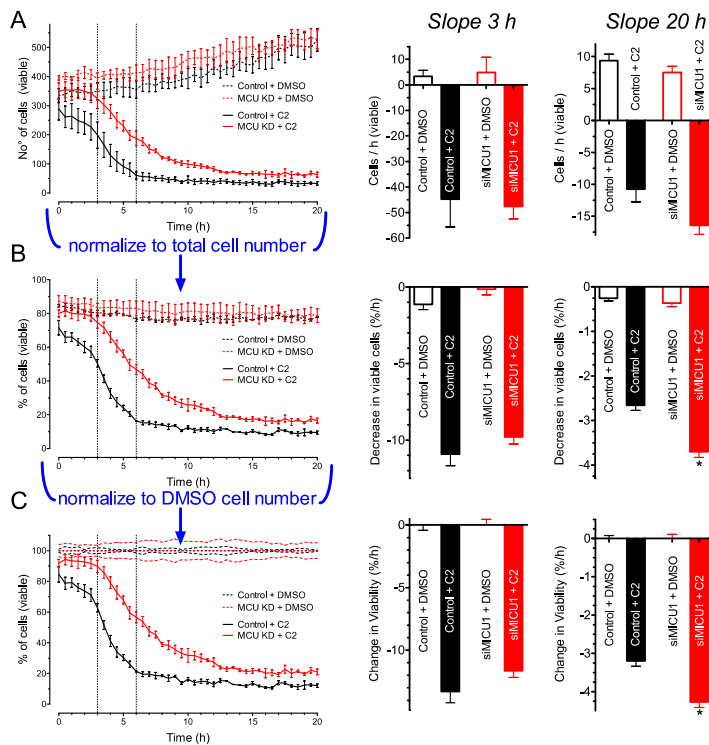


Figure (18): Example of steps morphological viability analysis (from Figure 39). *left panels*: Curves of viability of MCU knockdown (MCU KD, red) and control HeLa cells (black). Cell death was induced by treatment with 40 μ M C2-Ceramide (straight lines), controls were treated with the resolvent DMSO (dotted lines). *middle panels*: Slope of viability during 3 and 6 hours (vertical dotted lines in left panel). *right panels*: Slope of viability during entire experiment. **A**: Total number of viable and dividing cells for each condition are plotted. **B**: By dividing each value through the respective total cell number, the percentage of viable cells is determined. **C**: Finally, the viability of MCU KD and Control cells treated with C2-Ceramide was normalized to the respective DMSO control, yielding a MTT-like type of presentation.

ways (Figure 18). First of all, the total number of each cell type can be plotted (A), whereby the viability and proliferation can be presented. Sometimes it is useful to plot the fraction of each cell type. This is achieved by dividing the number of the respective cell type through the total cell count (B), in this case showing the percentage viability or of dead cells (Figure 20 A). If the viability of two different cell types with slightly different proliferation rates are compared (C, MCU KD and control, respectively) it is feasible to compare both conditions with cell death induction to their respective controls, similar to the analysis of an MTT assay.

1.7.2. Intensity Analysis

I performed this analysis using the MetaMorph 6.2r6 software. Other programs, like the open-access application Image J, can be used equally well.

The intensity analysis makes use of an images brightness, or to be more precise spatiotemporal brightness changes within an image sequence, due to the fact that in phase contrast imaging a dividing cell, a vacuolized cell, and certain types of cell death appear brighter than a viable non-dividing cell.

At first, the images of a sequence were binarized, i.e. a brightness threshold was set and every pixel brighter than this threshold was shown in white, the remainder pixels appeared black. Afterwards, small objects were erased from the image (Figure 19, top panels). Then,

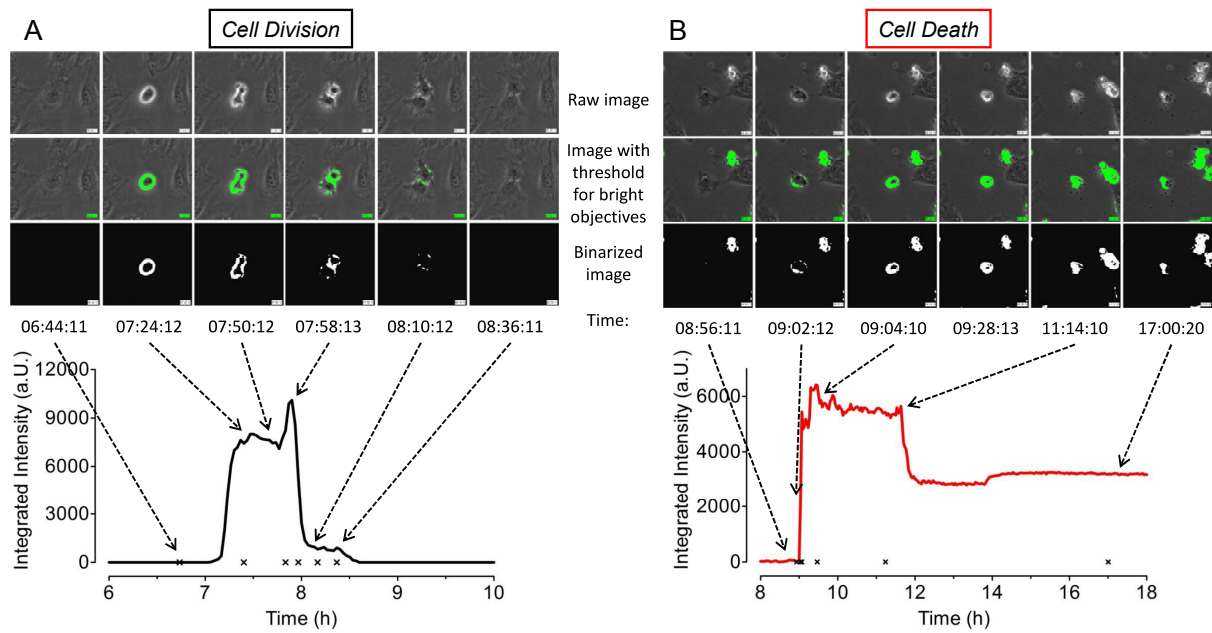


Figure (19): Examples of Intensity Analysis: The raw image is binarized into a black and white image by applying an intensity threshold. **A:** Temporal presentation of one cell division, which reflects a transient sharp intensity peak for about one hour. **B:** Temporal presentation of palmitic acid (PA)-induced cell death. This results in a sharp, but less pronounced intensity increase, reaching a stable level for the rest of the image sequence. Several cell death events sum up, cumulating over time.

the average brightness of a typical dividing or dead cell was calculated and the total cell number counted manually. Subsequently, the total image brightness was divided by the total cell number and the median single cell division brightness value. Approximately, the obtained value reflects the number of dividing or dead cells at every time point (Figure 20 B) (Khan et al., 2012).

At a first glance, this technique seems to be too unspecific, as a certain value reflects either a number of dead or dividing cells. However, if one takes a closer look at both processes, it becomes obvious that they can well be differentiated. A dividing cell appears as a strong transient intensity increase, which is soon abandoned (Figure 19 A). In contrast, the intensity of a dying cell increases relatively slowly, followed by a step peak in case of cell death. Subsequently, brightness decreases slightly, until a stable level is reached (Figure 19 B).

Hence, the intensity accumulates if the number of dead cells mounts, whereas dividing cells increase the intensity only temporally. Furthermore, any obtained value should always be put into context. If, for example, a toxic substance is added to the cell culture dish, it is more reasonable that an increase in intensity reflects a decrease in viability, rather than more dividing cells.

Last but not least, since both events can be easily differentiated, a trained person should always classify the obtained results.

1.7.3. Conclusion

To summarize both techniques and come to a conclusion under which circumstances which technique should preferably be used, I will now briefly enlist the pros and cons of both techniques, in particular by considering the efficiency, expenditure of time, applicability including potential to use as a high throughput analysis, and costs.

Both methodologies are not capable of reflecting the absolute cell counts for each time point of an image series keenly, yet the tendency of the spatiotemporal changes during one experiment can be drawn quite accurately. While the specificity is generally quite high (if the settings are optimized), the sensitivity is often rather low, particularly with the intensity analysis, which is only able to differentiate some kinds of cell death from cell division in a context-dependent manner. What exacerbates this method further is the fact, that the total cell count can only be calculated by counting manually, at least with MetaMorph 6.2r6.

Here, the morphology analysis is superior. First of all, the total cell count is estimated automatically, and several classes of cell types can be defined, thus one can differentiate

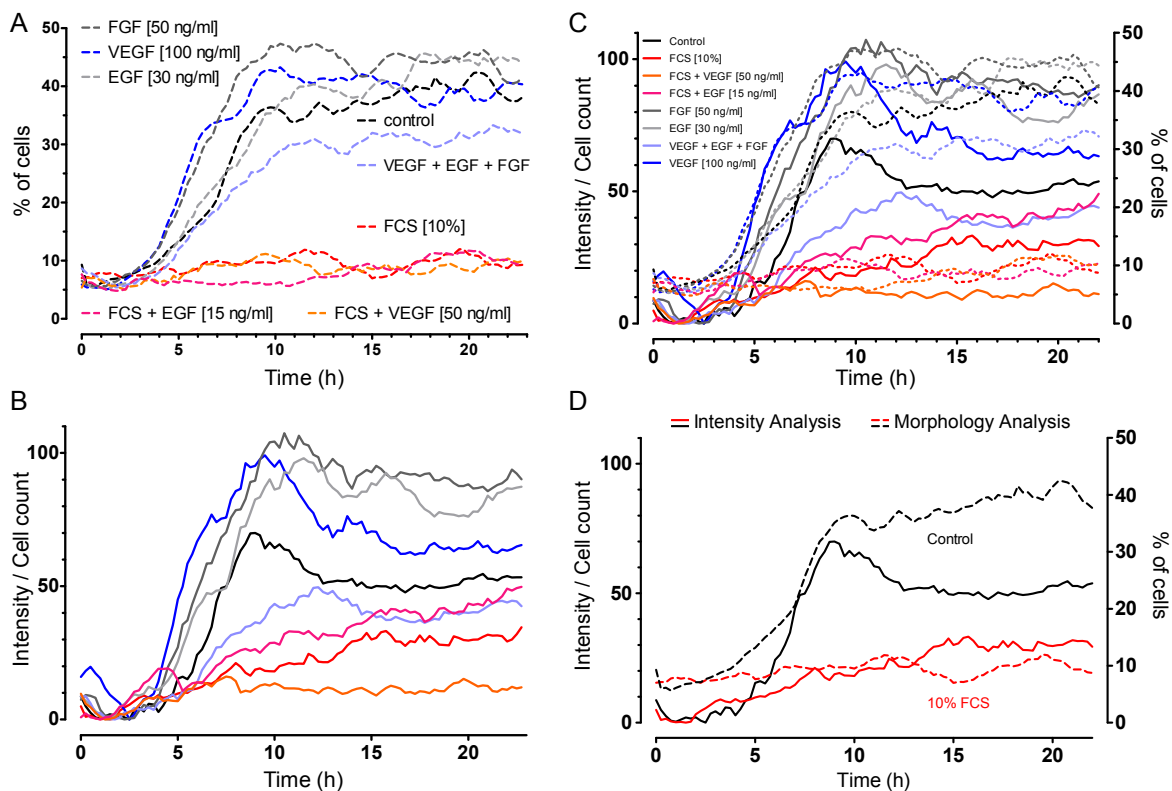


Figure (20): Comparison of intensity and morphology analysis of the same experiment with eight different conditions (compare to Figure 30, $n=1$). **A:** Dead cells were morphologically recognized with the Cell-IQ Analyser. **B:** Intensity of the binarized images was divided by the respective cell count. **C:** (A) and (B) superimposed, though not identical, the same tendency can be drawn by both techniques. **D:** Comparison of two conditions from (C).

between viable, dividing, altered, and several types of dead cells. Still, individually misplaced objects occur regularly, due to the mode of computing the results, as mentioned above, though those can be ignored, if the sensitivity is satisfactorily.

The time required to perform an analysis is an important factor in everyday's application. Especially during the compilation of a sample library required for the Cell-IQ Analyser to create a protocol, the morphology analysis is rather time intense. Although the preparation time is mitigated, once a protocol is present, slight adjustments need to be done for each experiment, in order to achieve optimal results. Apart from that, the actual time to compute the algorithm can easily take several hours, depending on the number of images analysed. So it is beneficial if the computer with the Analyser installed is not the same device which is used for data acquisition, as is the case in our laboratory.

The intensity analysis on the other hand is faster, with the cell counting taking most of the time. This can be solved by combining both techniques, so that the cell counter of the Cell-IQ Analyser is used instead, similar to the cell division estimation with only the cell counter. So, as a screening method for intensity increase accompanied cell death, the intensity analysis can well be used. The spatial change in intensity reflects not only the appearance of cell death events, but also its kinetics, which makes it superior to single end-point assays. Apart from that, other forms of cell death cannot be recognized, the cell division rate cannot be estimated as good as by using the cell counter solely, and for other morphology changes it is more or less blind (although the occurrence of vacuoles can to some extent be recognized since cells with vacuoles are slightly brighter than viable cells). Apart from that, the applicability of both methods is comparable, once some experience is made.

Last but not least the costs are an important factor. While the intensity analysis is without charge, if an open-access application like Image J is used, the morphology analysis is not. Programs like the Cell-IQ Analyser are very sophisticated and require constant care, and are highly specialised. Still, the once-only purchasing is worth it in my opinion, if long-term live-cell imaging needs to be performed and analysed. The amount of information that can be read out of an experiment is distinctly higher than with any other technique I can think of. It is also noteworthy, that although the time required to compute a differentiated cell count is rather long, it is far from being intractable as well as substantially more effective than performing the same analyses manually.

Overall, in cases where cell death appears as brighter cells, both techniques give comparable results (Figure 20). In this experiment, EA.hy926 cells were treated with different growth stimuli before observation. Cell death was estimated by morphology (A, dotted lines) or intensity analysis (B, straight lines), respectively. Interestingly, although not identical, the tendency of the fraction of dead cells and intensity / cell count reflect a comparable time course (C and D), shown by the similar curves of the same-colored dot-

ted and straight lines.

1.7.4. Migration Analysis

Several cell migration assays exist. I performed non-chemoattractant assays, also known as "wound-healing" assay, by scratching a wound or by using cell exclusion zone inserts (see above) (Liang et al., 2007; Yarrow et al., 2004). In the following, the methods I used to analyse are described.

The most straightforward method to estimate the ability of cells to migrate is to measure the size of the wound gap manually. I used MetaMorph 6.2r6., other softwares, e.g. Image J, could equally well be chosen. One can either retrace the area of the gap, or as a simplified alternative, draw a representative line over the gap (Figure 23 E and F, colored lines). This has to be repeated for each consecutive image of the image series. The decline of the area or length of the line, respectively, inversely correspond to the velocity of the migrating cells. From this data, the slope of the migrating cells can be calculated and compared for various conditions. This type of analysis was routinely performed for the scratch assay (Figure 34 and 42).

However, one can easily hazard a guess that with increasing numbers of conditions this methods soon becomes inefficient. Thus, more sophisticated and ideally automatic analysis methods are required. The first attempts to analyse the migration were performed using the similar means like the intensity analysis described in the previous part. This was possible because generally the gap appears brighter than the cells surrounding it. Then, in a binarized image the decline of the bright portion of the image could be used to calculate the gap closing. Unfortunately, the brightness of the images changes slightly in the course of most image series so that several adjustments to the threshold needed to be applied. Additionally, the same threshold cannot always be used for every position. Hence, the gain in efficiency of analysis was negligible if several attempts with different intensity thresholds were needed.

On the other hand, visual analysis tools are available (Yarrow et al., 2004; Gebäck et al., 2009) I tested the wound-healing option of the Cell-IQ Analyser (Figure 21). The first step is to set a threshold value by which the software differentiates between the gap and cell area. I assume this is mainly computed by intensity analysis, similar to my first attempt, although the exact algorithm is again not stated by the company. In most cases, this already renders a convincing result, but slight adjustments still need to be applied. In the subsequent steps the software allows to define values for minimizing gaps between recognized pixels, subtracting small objects, and ignoring small gaps. The latter point prevents the recognition of gaps within the cohort of cells, which happens quite regularly. Typically at the prefinal stages this can turn into a drawback. Expectedly, the individual

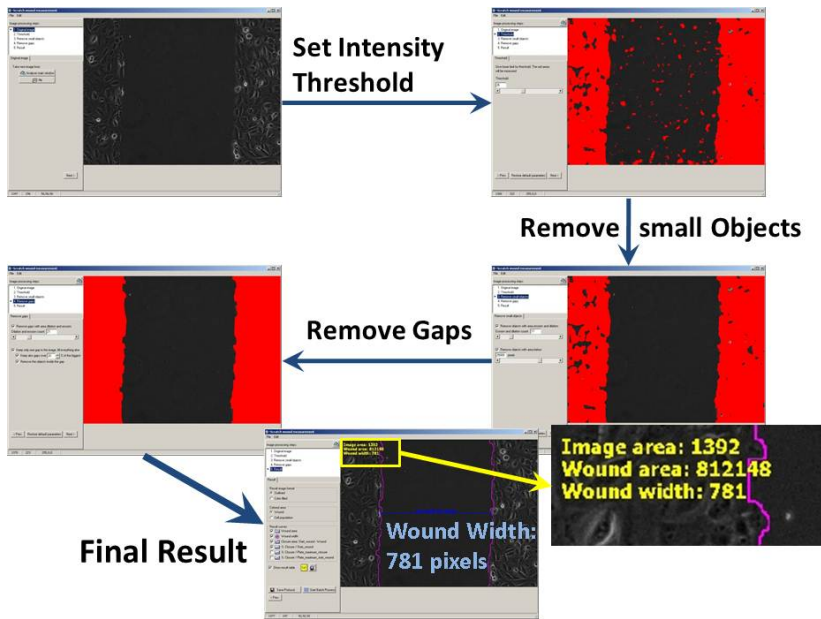


Figure (21): Process of the Cell-IQ migration analysis. At first, an intensity threshold is set on the raw image. Afterwards, small objects are removed and subsequently gaps within the cell areas are deleted. Finally, the particular wound width and area are shown.

cells do not migrate with the same pace and, thus, in some areas the gap closes faster than in others. If now the software allows only one gap (the biggest) to be recognized, this causes a feigned sudden decline of the gap size. This can be circumvented by allowing the recognition of more than one gap. The minimum size of the detected gaps can be defined in relation to the biggest, e.g. 25%. This has the detrimental effect that the Analyser sometimes does not compute 100% gap closure, but rather something like 98%. Nonetheless, in the majority of cases, this gave a realistic quantification of the migratory potential, comparable to the intuitive estimation of looking at the image series.

Usually, for several positions of the same experiment the same values could be applied, rarely some adjustments had to be made and different computation had to be performed. Noteworthy, this did not occur, if the images were acquired with the Cell-IQ and only rarely when using the ACLSM. Images that were acquired on the ACLSM also needed to be converted from the acquired .tif files to .jpg files, as the Cell-IQ Analyser was unable to edit tif files.

Another aspect that needs to be considered is the cleanness of the gap. By this I mean

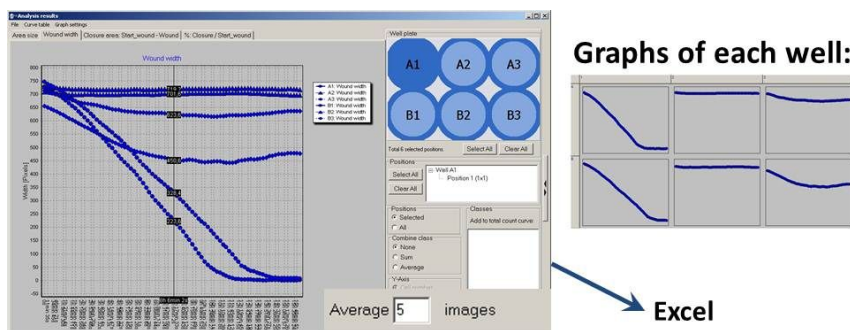


Figure (22): Cell-IQ result curves of a WH image series with six different wells. To minimize aberration, the average of five time-points is calculated for each point. The data can be exported to Excel for further analysis.

that the gap ideally should be free of cellular debris or reattached cells at the inception of the experiment. Accordingly, the semi-automatic analysis of a scratch assay was essentially limited. I was not successful in establishing a method of washing the samples well enough so that the Cell-IQ Analyser was able to differentiate the gap clearly from cells at every timepoint. In most cases, cellular debris interfered with the ability of the software to recognize the gap. Therefore, I preferably used the cell exclusion zone inserts, which concomitantly led to less variation in the size of the gap, albeit not abolishing it (Figure 23 C, E, and F).

1.7.5. Estimated Pace of Migration Depends on Applied Analysis

Another point that needs to be mentioned is the percentage bias of the migration analysis. Essentially, there are two possible ways of analysing the migration pace of a woundhealing assay, i.) the wound closure in relation to the initial gap size (Figure 23 A, B), and ii.) the closure of the gap widths in units of length (Figure 23 C, D). Throughout my thesis, I used the arbitrary unit of pixels, determined by the Cell-IQ Analyser. Note that, depending on the system and quality of the acquired images, the pixel width potentially varies between different experiments, although the true width should be around 500 μm .

At a first glance, the first attempt of plotting the percentage wound closure is more catchy, as any condition starts at 0% and the temporal variance until complete wound closure was reached for various conditions should reflect the difference in migration ability. With perfectly normalized initial gap widths, both means of data presentation should be the same. If, however, the gap widths are not similar (as is mostly the case), there would be a difference between the two types of data presentation.

I chose to present one of my first woundhealing assays as an example of this percentage bias. Here, I intended to visualize if the endocannabinoid anandamide (AEA) has any influence on the migration of EA.hy926 cells, both in absence (black and green) or presence (red and blue) of serum (FCS). At first, I only plotted the percentage wound closure (Figure 23 A,B) and found, that addition of AEA diminishes the migratory pace of EA.hy926 cells with FCS present, while under serum starvation either condition did almost not migrate at all. This was reflected by the slope of gap closure in percent per hour of 6.6 for FCS and 4.3 for FCS + AEA. In subsequent experiments, I could not replicate this result. Therefore, I looked at my results again, and realized, that the initial gap width was much wider for the FCS + AEA (Figure 23 C, E, F, blue lines) condition than for the other three conditions (red, black, and green lines). Now, I decided to plot the decline in the gap width (C) and calculate the inverse slope of migrated pixels per hour from it (22.0 and 20.4, respectively). Although the FCS + AEA still migrated slightly faster by this analysis, the difference was much smaller (Figure 23 F, bottom panel) and

more realistic.

Consequently, for any subsequent migration analysis, only the wound width analysis is shown.

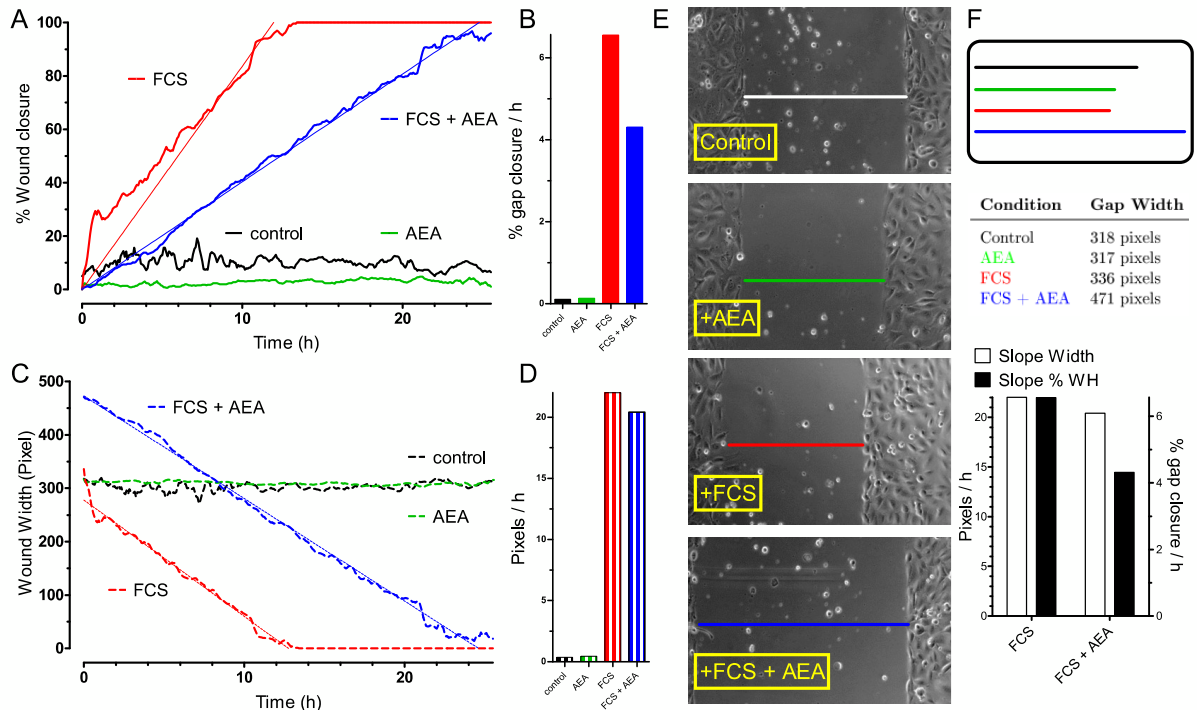


Figure (23): Exemplified analysis of a "wound-healing" experiment using the Cell-IQ Analyser. Cells were incubated in experimental buffer with or without 10% FCS and anandamide (AEA, 1.5 mM in absence, 15 mM in presence of FCS) or the solvent ethanol, respectively. (n=1) **A**: Gap closure shown as percentage of the initial situation. **B**: Bar charts indicate the percentage slope per hour from A. **C**: Gap closure shown as decline in gap width. The origin of the lines represents the initial gap width. **D**: Bar charts indicate the inverse slope from C in pixels per hour. Thin lines in A and C represent the slope until gap closure assessed by linear regression. **E**: Images show the gap width at the beginning of the experiment for each condition as indicated. Colored lines show the length of each gap. **F**: The *upper panel* directly compares the gap width of each condition, which are enlisted in the table in the *middle panel*. The *lower panel* shows a direct comparison of the slopes calculated from the width (white bars) and the percentage (black bars), respectively.

2. Morphological Peculiarities

During the experimental work on my thesis, I acquired a plethora of image series. This led to the observation of several morphological peculiarities, both on the single cell level and the population level. In this section I present a few examples of my image series, like multi-nucleated cells, atypical cell divisions, or merging cells, but also the appearance of vacuoles in the majority of cells upon treatment with some pharmacological compounds, which could be satisfactorily quantified with the morphological analysis of Cell-IQ Analyser.

2.1. Multi-Nucleated Cells and Merging Cells

In almost every image series I made, peculiar cells or events were observable. Accordingly, the term peculiar is maybe not a perfect, but still feasible description of what was observed.

First of all, I realized that on mostly any area of observation some cells were conspicuously huge and had multiple nuclei, especially if EA.hy926 (Figure 24, *left panel*) or HeLa cells (*right panel*) were used. Particularly bi- and tri-nucleated cells were no rarity at all, but also multi-nucleated, sometimes ten or more, were observed. For the somewhat smaller INS-1 cells, multiple nuclei were more difficult to recognize.

With more careful inspection of the acquired image series, I found that a multi-nucleated cell can form by two means, both relied to cell division. Firstly, a multi-nucleated cell can arise from an incomplete cell division, yielding one daughter cell with twice as many nuclei as its progenitor cell. Secondly and more typically, a multi-nucleated cell can come into existence by merger. In almost any observed case, this happened between two daughter cells from the same division within a couple of hours later (Figure 25). Within the timeframe of the 12-48 hours of most of my experiments, I suspect that a fusion between two cells can be seen on mostly any series. However, since the merging typically appears between two cells of the same kinship that in most cases remain in close vicinity before the fusion, regularly it is hard to differentiate if the two cells were at any time completely separated, or if, after all, incomplete cytokinesis is the cause for most of these processes. But in some examples seen, the cells seemed to be truly separated before merger, especially in the more agitated EA.hy926 cells (not shown).

However, every attempt to computationally quantitate the cell merging process over time remained unsatisfactorily incomplete. The same was realized for the quantitation of multi-nucleated cells with the tested softwares and applications. Thus I resigned to quantitate these processes, as the immense amount of data could not have been reasonably rendered

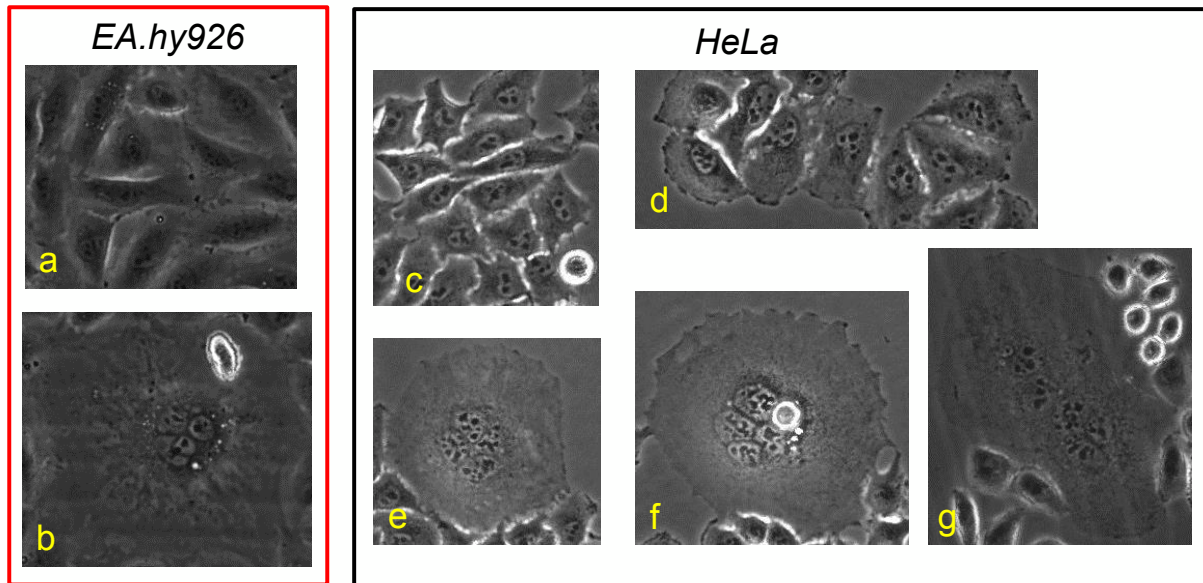


Figure (24): Exemplified images of multi-nucleated EA.hy926 cells (*left panel*) and HeLa cells (*right panel*). **a**: regular EA.hy926 cells. **b**: one EA.hy926 cell with at least five nuclei. **c**: regular HeLa cells. **d**: group of bi-nucleated HeLa cells. **e**, **f**, **g**: examples of multi-nucleated HeLa cells with seemingly up to ten nuclei.

in the frame of my diploma thesis.

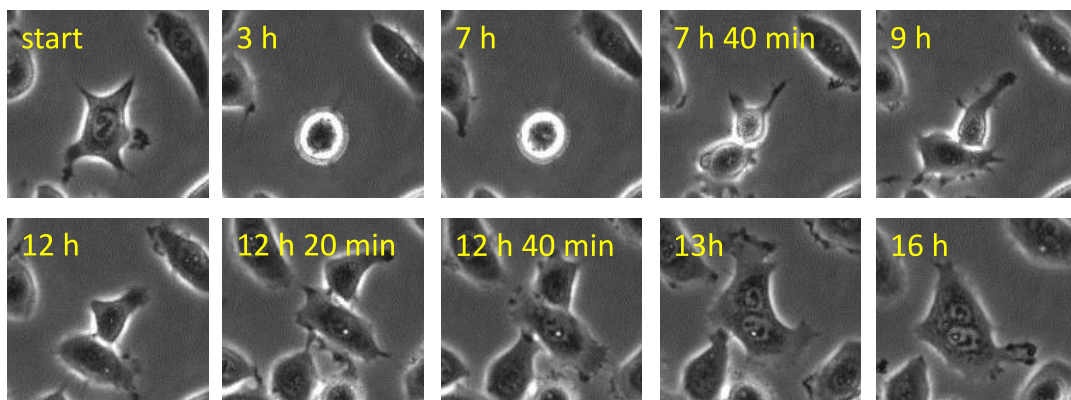


Figure (25): Time course of a HeLa cell division, followed by a fusion of the same HeLa cell. Between 9 hours and about 13 hours after start of the sequence the two daughter cells clearly appear separated. Afterwards, the two daughter cells fuse and become one multi-nucleated cell.

2.2. Atypical Cell Divisions

Another interesting note was the observation of atypical divisions, i.e. divisions with more than two daughter cells. Since most of the experiments were performed using cultivated cancer cell lines this was expected, albeit a fascinating event at a first glance.

Hence, I decided to show one example of a triplicate division observed in primary hu-

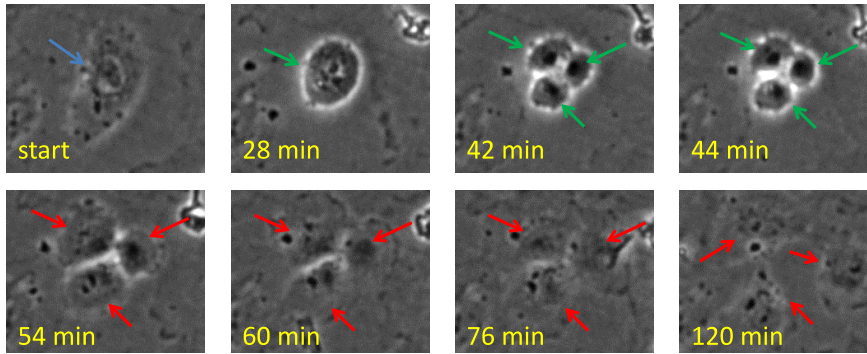


Figure (26): One HUVEC (blue arrow) divides into three daughter cells (red arrows). After about 28 minutes the cell starts to divide (green arrows). At about 42 minutes three daughter dividing cells crystallize.

man umbilical vein endothelial cells (HUVEC, Figure 25). Similar atypical division were observed more regularly in the cancerous cell line, sometimes with four or even more descendants.

2.3. Vacuoles Occur Transiently upon Treatment with the PI3K Inhibitor Wortmannin after 15 Minutes

Finally, in this section I also show examples of morphological peculiarities on the cell population level, that could be quantified with Cell-IQ Analyser. In a set of experiments in which the toxicity of the saturated fatty acid palmitic acid (PA) on EA.hy926 cells was tested (Khan et al., 2012), I found that the PI3K inhibitor wortmannin (WM) had a protecting effect (data not shown, see (Khan et al., 2012) supplemental video 1 and 2). When I made image sequences of cells treated with or without 1 μ M WM, it was observed that the cells treated with WM time dependently developed vacuoles between about 15 minutes and 4 hours after treatment, irrespective of presence of PA (Figure 27). The disappearance of the vacuoles after 4 hours most likely is due to light-dependent inactivation of WM (Warashina, 1999). In this period literally all the WM-treated cells had vacuoles (Figure 27 F, upper panel, middle image).

In order to morphologically differentiate cells with "vacuoles" from other regular ("viable") cells (Figure 27 A), I created an according sample library with Cell-IQ Analyser (Figure 16). Additionally I included several other types of cells, namely "dividing", "membrane blebs" (Figure 27 B), which also appeared transiently in less quantity upon treatment with WM, and "dead" cells (Figure 27 C). Each of those morphological cell types were plotted in relation to the total cell number (Figure 27 D).

As the vacuoles appeared as bright dots within the cells, intensity analysis could also be applied to determine the appearance of the vacuoles (Figure 27 E). Here, the image series was analysed as described above by intensity analysis. By trend, the appearance of the vacuoles could be accurately drawn by both Cell-IQ Analyser and intensity analysis. Nonetheless, this data confirms my conclusion, that both techniques cannot suitably be applied to determine exact numbers of different cell types. This was also endorsed by the

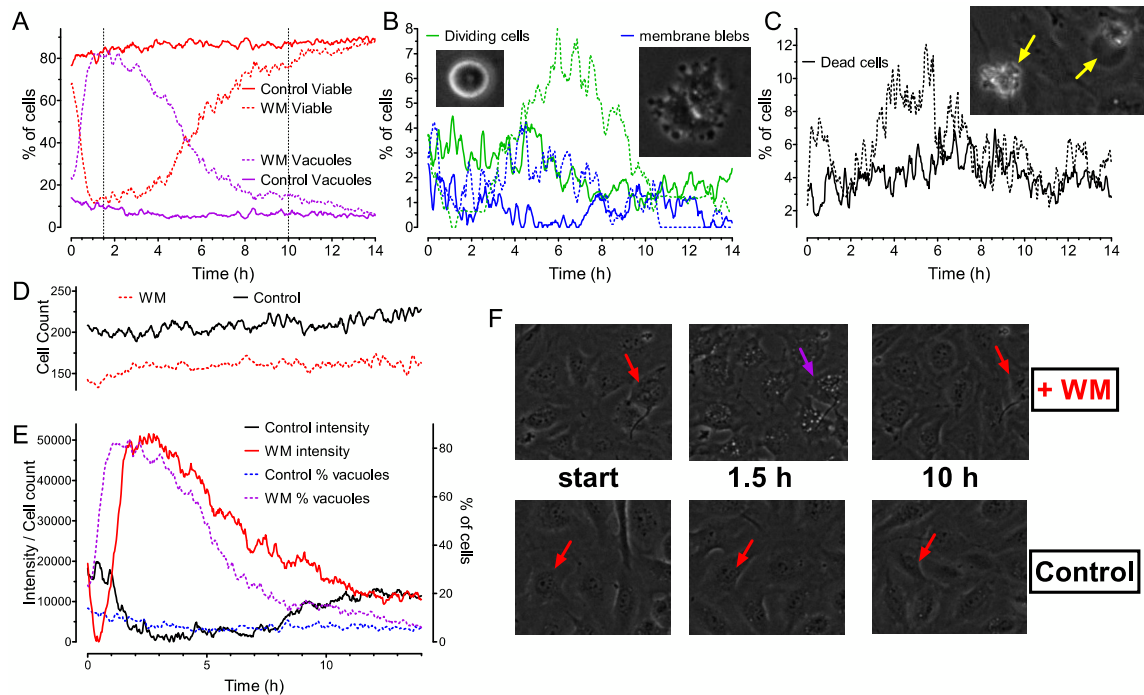


Figure (27): Appearance of vacuoles and other morphological peculiarities can be quantified by morphology analysis (A,B,C) or intensity analysis (E). In this experiment, EA.hy926 cells ($n=1$) were either treated with $1 \mu\text{M}$ of the PI3K inhibitor wortmannin (WM, dotted lines) or same amount of solvent DMSO (straight lines). **A**: Curve representing normal cells (green lines) or cells with membrane blebs (blue lines). Vertical dotted line indicate the timepoints at which representative images from F are shown. **B**: Curve representing dividing cells ("viable", red lines) or cells with vacuoles ("vacuoles", purple lines). **C**: Curve representing dead cells (black lines). **D**: Total number of cells of WM treated cells (red dotted line) or control cells (black line). **E**: Comparison of morphological analysis of Cell-IQ Analyser with intensity analysis. Intensity threshold was set as to include the vacuoles. Subsequently, the image were binarized and the intensity measured was divided through the respective cell count from E (see "Establishment of Analyses Techniques"). The resultant curve represents the intensity of each cell at any timepoint. For both WM-treated (red line from intensity analysis and dotted purple line from Cell-IQ Analyser) and control cells (black line from intensity analysis and dotted blue line from Cell-IQ Analyser) the resultant curves matched each other. **F**: Representative images indicating appearance of vacuoles in WM-treated cells (*top panel*) between about 20 min and 3.5 hours of experiment, which was not observable in controls (*bottom panel*). Purple arrows represent cells with vacuoles, red arrows "viable" cells.

numbers of the other cell types, which were too high (except for "viable" cells). Especially the "membrane blebs" cells only appeared in the first hours of treatment with WM, yet were recognized throughout the entire experiments in both groups (Figure 27 C, blue). An increase of "blebs" at the beginning of the experiment can be seen, but this is not clear.

The number of "dividing" cells, on the other hand, was accurate, at least in the control cells (Figure 27 C, green). The appearance of vacuoles of the WM-treated cells, however, obviously interfered with the morphological pattern of "dividing" cells. Thus, at first the fraction of cell divisions was falsely too low, lateron too many were recognized.

Finally, the number of "dead" cells was in any case too high, also partly explainable by

the inclusion of "vacuole" cells. In both groups, almost no cell death appeared, yet the fraction of "dead" cells was around 4% in both conditions. This shows again the limitations of the Cell-IQ Analyser.

2.4. Crateagus Extract WS-1442 induces Strong, Light-Intensity-Dependent Phototoxicity and Vacuolization

In another set of experiments, I tested the effect of the Crateagus extract WS-1442 on EA.hy926 cells (Willer et al., 2012). Crateagus, or hawthorn, is used as a phytopharmakon against mild forms of heart failure, which was shown to improve clinical symptoms, without a clear effect on mortality (Dahmer and Scott, 2010). Moreover, it was shown to yield an anti-hypertensive effect (Walker et al., 2002) and could prevent restenosis after balloon catheter induced dilatation of the carotid artery in a rat model (Fürst et al., 2010). The latter effect was shown to be evoked by an inhibitory effect on vascular smooth muscle cells rather than endothelial cells (Fürst et al., 2010). In contrast to our expectations, I observed a clear cell death induction in long-term live-cell imaging experiments upon 10-100 $\mu\text{g}/\text{ml}$ WS-1442 treatment, which did not occur in EA.hy926 cells treated with equal concentration of WS-1442, but kept in the cell incubator (Figure 28 A and C). In the cells treated with lower concentration, cell death appeared delayed (not shown). I suspected this difference might be caused by light.

Accordingly, I conducted an experiment to test if WS-1442 induces phototoxicity. Three 35 mm dishes of confluent EA.hy926 cells were treated with 100 $\mu\text{g}/\text{ml}$ WS-1442 in loading buffer. Two were defined as ROI 1 (Figure 28 B, left panel, Intense Light) and ROI 2 (B, right panel, Reduced Light), the last dish was kept in the same atmosphere of the ACLSM incubator as the other dishes, but covered with foil (Figure 28 C, middle panel). As previously described, the image acquisition process of the ACLSM leads to a higher light exposure of ROI 1 than of any other ROI. In both ROI's I could observe a quick cell death induction, however, the cells of ROI 1, i.e. intense light, cell death appeared enhanced (maximal cell death recognition after about 3 hours, compared to 6 hours in ROI 2, i.e. reduced light).

Then, I used the newly developed settings indicated before to apply the same light exposition to both ROI's and observed cells treated with 100 $\mu\text{g}/\text{ml}$ WS-1442 (Figure 28 C, top panel) or solvent-treated controls (C, bottom panel). As before, WS-1442-treated (C, middle panel) and non treated controls (not shown) were kept nearby the microscope and covered with foil. By this, I unveiled a phototoxic effect of WS-1442, which was dependent on the light exposition.

Furthermore, I found that the Crateagus extract WS-1442 induced the appearance of vac-

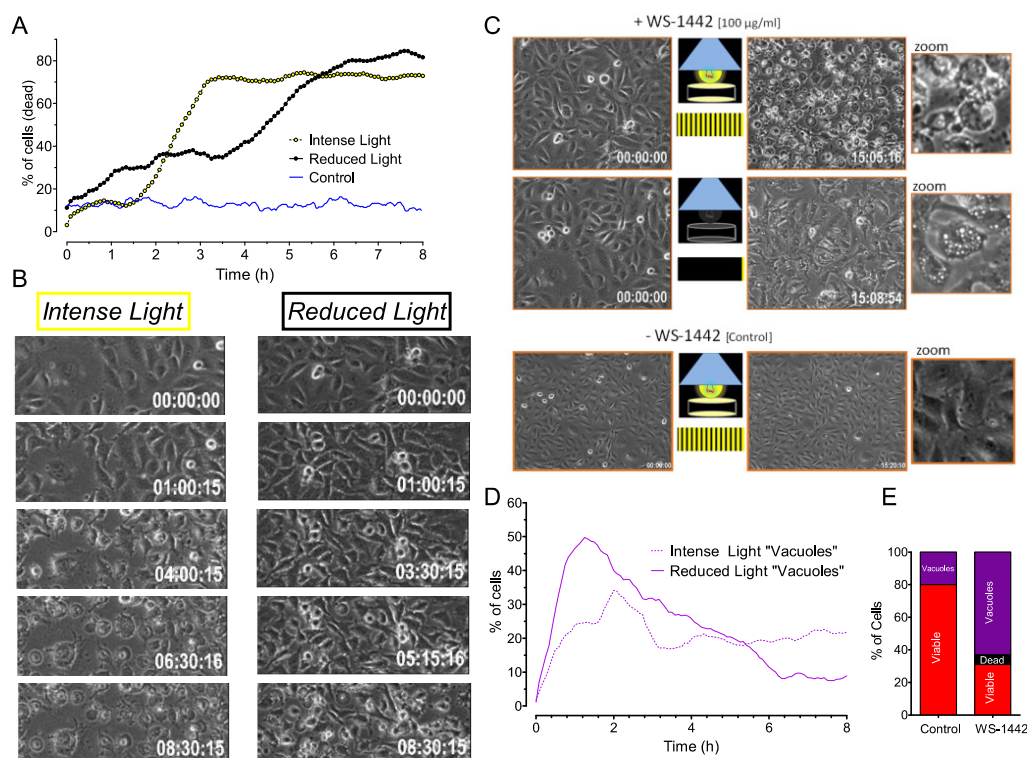


Figure (28): Phototoxic effect of Cateagrus extract WS-1442 on EA.hy926 cells ($n=1$). Image were morphologically analysed by Cell-IQ Analyser. **A**: Percentage of dead cells treated with $100 \mu\text{g/ml}$ WS-1442 exposed to intense light (yellow dots) or reduced light (black dots). Intense and Reduced light was applied as shown in Figure 14 C. Non WS-treated cells (Control, blue line) are derived from another experiment. **B**: Representative images of cells exposed to intense light (*left panel*) or reduced light (*right panel*). **C**: Representative images of cells treated with WS-1442 (first two rows) or controls (third row). The cells in the first row were exposed to light, while those in the second row were incubated in the dark and one image at the start and one at the end was acquired. **D**: WS-1442 treated cells possessed a transient increase in cells with vacuoles (purple lines) before the viability decreased (compare to A). Of the cells exposed to reduced light (straight line) more had vacuoles than of those exposed to intense light (dotted line). **E**: Percentage of viable (red), dead (black), and cells with vacuoles (purple) of the final image of WS-1442 treated cells and control cells incubated in the dark. While under both conditions almost no cell death occurred (control: 0%, WS: 6%), the number of cells recognized with vacuoles more than triplicated (control: 20%, WS: 66%).

uoles (Figure 28 C, D, and E). Most intensively, this was observed in the control cells also treated with WS-1442 but kept in the dark under the same incubation conditions. These cells did not die, but developed an immense increase in cells with "vacuoles" (Figure 28 C, middle panel). The only time those cells were exposed to light was at the acquisition of the initial and final image. This was in line with a previous report about the effects of this compound (Willer et al., 2012).

I used the Cell-IQ Analyser morphology analysis to determine the number of "viable", "vacuole", and "dead" cells, first for the image serie of the Intense vs Reduced Light experiment (Figure 28 D). Interestingly, both cell groups developed a detectable increase of "vacuole" cells within the first 2 hours. While of reduced light cells (straight lines) approximately 50% of cells had vacuoles, only about 35% of intense light EA.hy926 cells (dotted

lines) had. Of the control cells incubated in the dark, 80% were "viable", and 20% had "vacuoles", "dead" cells did not appear at all. In the WS-1442-treated non-light exposed cells, 31% were "viable, 63% had "vacuoles", and 6% were recognized as "dead" (Figure 28 E). This estimation was more accurate than in the previously presented experiment. This was not due to a better differentiation of the Cell-IQ Analyser, but the fact that the sample library in this case was substantially optimized with those four images. Accordingly not many cells were grouped falsely, but this resembled more a manual analysis. Still, for the entire image series of the cells exposed to intense and reduced light from Figure 28 A, the fraction of cells with "vacuoles" was accurately estimated (Figure 28 D).

3. Effect of Growth Factor and Nutrient Deprivation

In the following section various experiments are presented, concerning modulations in the composition of the experimental buffers and media. Strictly speaking, I tested effects of various growth factors (GF) and removal of serum and glucose on endothelial cells (EC), HeLa cells, and pancreatic *beta* cells. The experiments were performed at different times and are not presented in a chronologic, but thematic order. They were neither necessarily performed on the same system, nor part of the same set of experiments.

3.1. Endothelial Cells reduce Viability in Absence of Serum

In the first part of this section, two of my earlier experiments are presented. The experiments were performed on the ACLSM, hence, instead of cell culture medium with bicarbonate pH buffer, the experimental buffer was used.

3.1.1. Upon Serum-Starvation Sub-Confluent Endothelial Cells Change their Morphology and Appear Elongated

At first, I tested the effect of serum deprivation on the growth and viability of EC. Cells were grown on two 35 mm dishes until about 50% confluency was reached. Then, during image acquisition, half of the cells were further incubated in experimental buffer without any serum or GF (Control, Figure 29 D, lower row), the other half was incubated in experimental buffer containing 10% fetal calf serum (FCS, Figure 29 D, upper row).

In the course of the 24 hours experiment, the control cells showed almost no change in confluency, whereas the FCS-treated EC exhibited an increase of about 12.5% (Figure 29 A). Noteworthy, an increase in confluency possibly corresponds to both a rise in total cell number and/or a change in cellular morphology. Both appeared to be the case. In Figure 29 B, I plotted the average fraction of dividing cells at each timepoint, analysed with the Cell-IQ Analyser. As expected, in average 5.4% of the FCS-treated EC were dividing on each image, significantly more than control cells (4.3%). At a first glance, I had the impression, that those EC without a growth stimulus changed their shape and appeared increasingly "elongated" (Figure 29 C, dotted lines, and D, indicated by yellow arrows). As quantized by Cell-IQ Analyser, after about 13 hours 50% of the cells lacking serum appeared "elongated". I also recognized a decrease in spontaneous movement of control cells, almost halting after about 20 hours (not quantified).

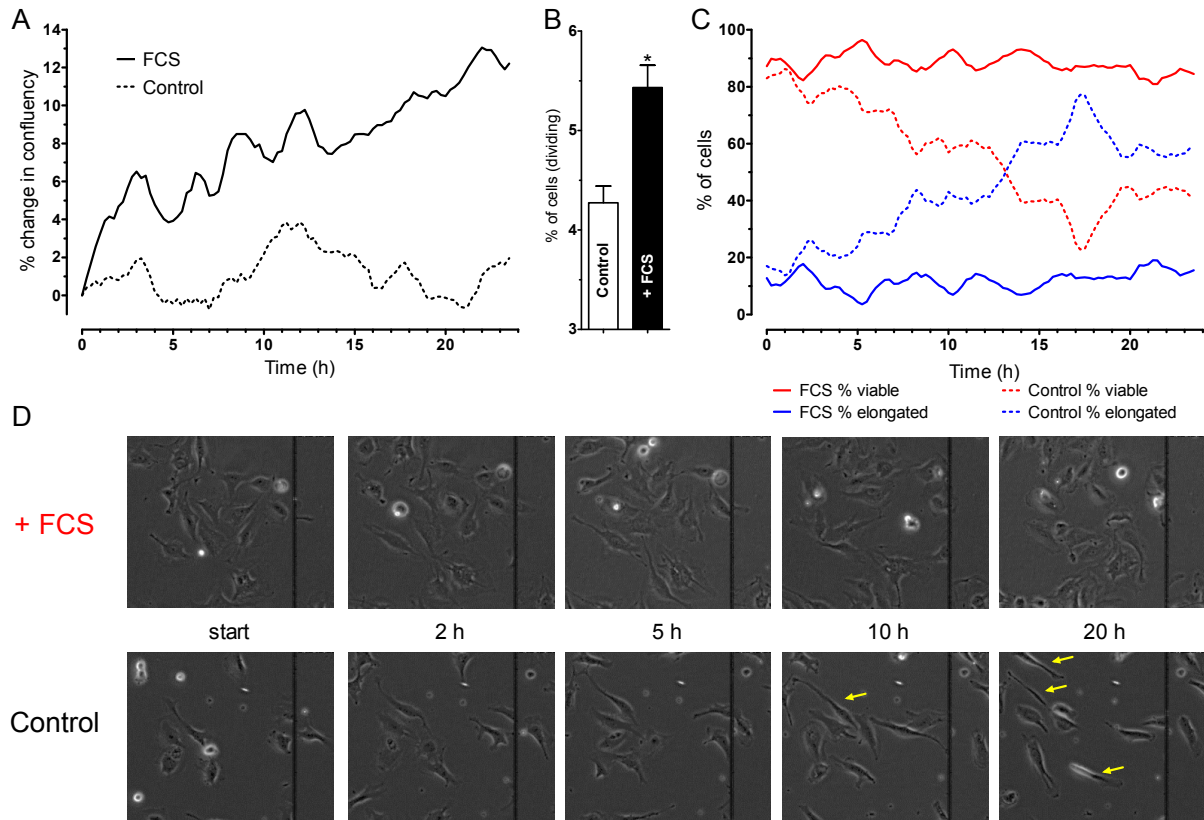


Figure (29): Effect of FCS on sub-confluent EC during 24 hours of imaging ($n=1$). **A**: Relative change in confluency, representing both cell size and number. **B**: Average percentage of dividing cells at any instance. **C**: Changes in cellular morphology are induced by serum starvation, shown is percentage of viable cells and "elongated" cells (yellow arrows). **D**: Representative time-lapse images of cells treated with 10% FCS or without GF, yellow arrows indicate "elongated" cells, quantified by Cell-IQ Analyser.

3.1.2. Serum-Starvation Induced Viability Decrease cannot be Rescued by Addition of Single Growth Factors

In a subsequent experiment, I tested eight different experimental buffer GF compositions. In contrast to the previous experiment, the cells were grown on an eight-well dish in cell culture medium until fully confluent. Then, the EC were incubated in experimental buffer containing the growth stimuli presented in Table 3. The respective concentrations of the GF's were derived from various publications, where those concentrations were used to stimulate EC to migrate (Cavallaro et al., 2001; Grotendorst et al., 1989). In the conditions with multiple GF's, the concentration was divided by the number of GF's present, so that the intensity of GF stimulation should be comparable, except for FCS, which was always used in the standard concentration of 10% of the total medium volume.

The first observation of this experiment was, that, in line with the previous experiment, EC viability diminishes in the absence of FCS, indicated by the appearance of bright conglomerates of detached, presumably dead cells (exemplified images of Figure 30 A,

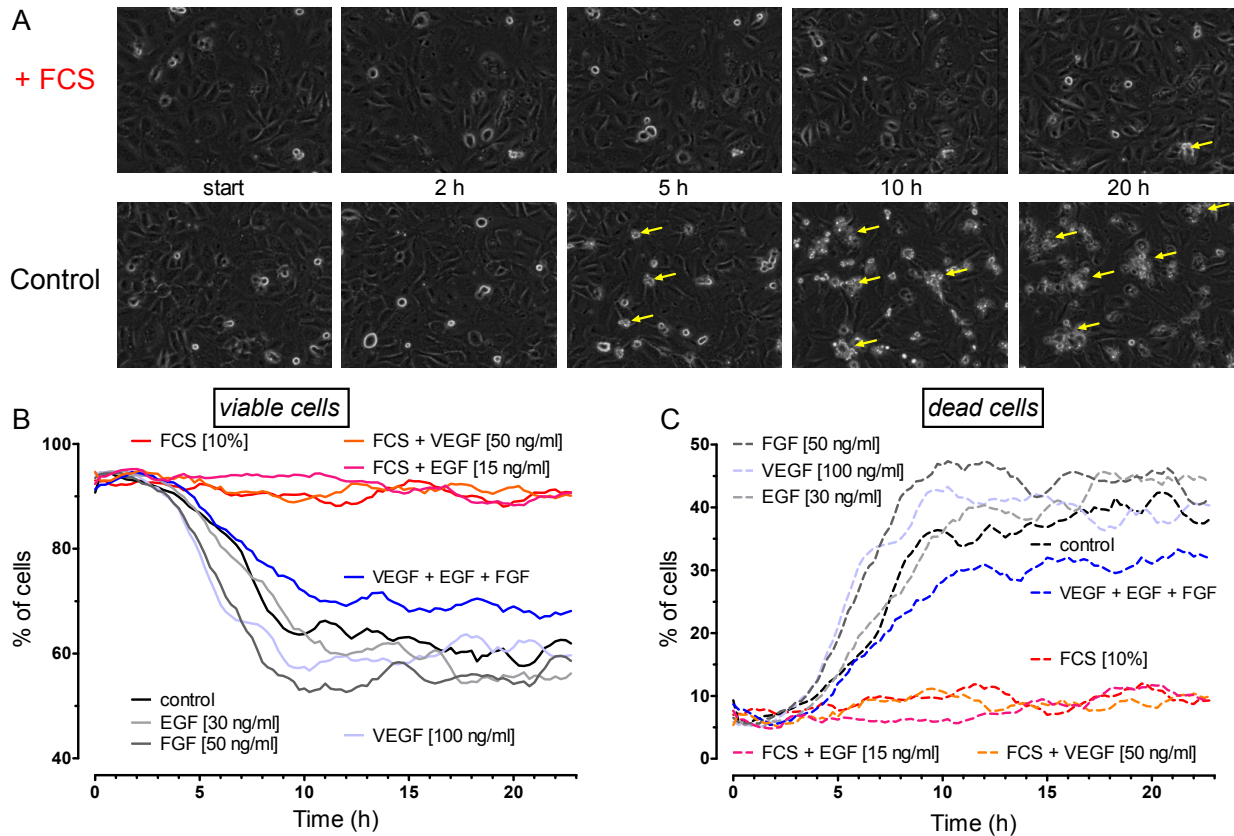


Figure (30): Effect of various GF compositions on fully confluent EC viability during 24 hours of imaging ($n=1$). **A**: Representative time-lapse images of cells treated with 10% FCS or without GF, yellow arrows indicate bright dead cells. **B**: Percentage of viable cells. **C**: Percentage of dead cells.

yellow arrows). Interestingly, lack of serum rather than growth stimulation *per se* was the key factor, as the control cells without any stimulation did not differ from those with GF's present. All the conditions that included FCS showed no impairment on cell viability in the course of the 24 hour observation period. To the contrary, in the cells treated with serum-free buffers, the fraction of viable cells rapidly declined at about five hours, reaching a stable phase at about ten hours, whereafter cell death occurrence decelerated. Figures 30 B and C show the time courses of viable and dead cells, respectively, computed by Cell-IQ Analyser, where viable cells (Figure 30 B) represents "viable" and "dividing" cells. This proved to be a satisfactorily accurate calculation of the subjectively estimated tendency. The sub-maximal viability (90.7% - 94.6%) at the start of the experiment of each position reflects the limitations of the morphology analysis, as false negative classifications are inevitable. Interestingly, this analysis unveiled, that combined usage of several GF, namely vascular endothelial GF (VEGF), epidermal GF (EGF), and fibroblast GF (FGF), each in one third of the single GF concentration, seemed to have a reductive effect on cell death (Figure 30 B and C, blue lines). By trend, the same result was obtained by intensity analysis (Figure 20).

Position	Growth Factors	Concentration	
1	Control, no GF		
2	FCS	10%	
3	vascular endothelial GF (VEGF)	100 ng/ml	
4	epidermal GF (EGF)	30 ng/ml	
5	fibroblast GF (FGF)	50 ng/ml	
6	VEGF + EGF + FGF	33 + 10 + 17 ng/ml	Tab. (3): Conditions used in the experiment presented in Figure 30.
7	FCS + VEGF	10% + 50 ng/ml	
8	FCS + EGF	10% + 15 ng/ml	

Of note, however, as each condition was only acquired once, no statistically utilisable analysis was possible. Another point which has to be accounted carefully, is the fact that in experiments with cell culture medium, no comparable reduction in viability occurred in response to serum starvation (Figure 35).

3.2. Serum-Starvation of HeLa Cells does not Alter Their Proliferation Rate for 12 Hours

In the next part, I present experiments in which the effect on cellular viability in response to serum starvation was devolved to the cervical cancer cell line HeLa (Figure 31).

HeLa cells were plated a 12-well plate one day before image acquisition. Likewise to the first presented experiment with EC, the cells were grown to sub-confluent level (in average 35.9% - 44.10%). About 30 min before the experiment started, the medium was exchanged to either cell culture medium with (Control + FCS, red lines or bars) or without (Control 0 FCS, black lines or bars) 10% FCS.

Interestingly, in contrast to the results from figures 29 and 30, FCS removal did not lead to a drastic increase in the number of dead cells, but rather caused a halt in cell growth. Thus, I decided to plot the confluency (Figure 31 A) and total number of cells on each image (Figure 31 E) estimated by the Cell-IQ Analyser. Both modes of analysis clearly showed, that during the first 12 hours of serum deprivation, no significant decrease in cell growth occurred (Figure 31 A, green box, and C). To the contrary, cells even seemed to grow slightly faster in absence of serum as shown by the slope of confluency (0.90% / h, blue and black line vs. 0.79% 7 h, red line).

Afterwards, another condition was introduced by re-addition of serum-containing medium (Rescue, blue lines and bars). To eliminate the possibility that the medium exchange itself would effect the cell growth, the medium of the controls was also exchanged with or without serum, respectively. As expected, the subsequent increase in confluency (Figure 31 B) of the Rescue (0.75% / h) and Control + FCS (0.78% / h) cells was significantly higher than of the controls without FCS (0.18% / h). Rather surprising, however, was the finding, that the increase of the total cell number (Figure 31 F) of the Rescue cells (7.9 cells / h / image) was significantly higher than both controls with (6.5 cells / h /

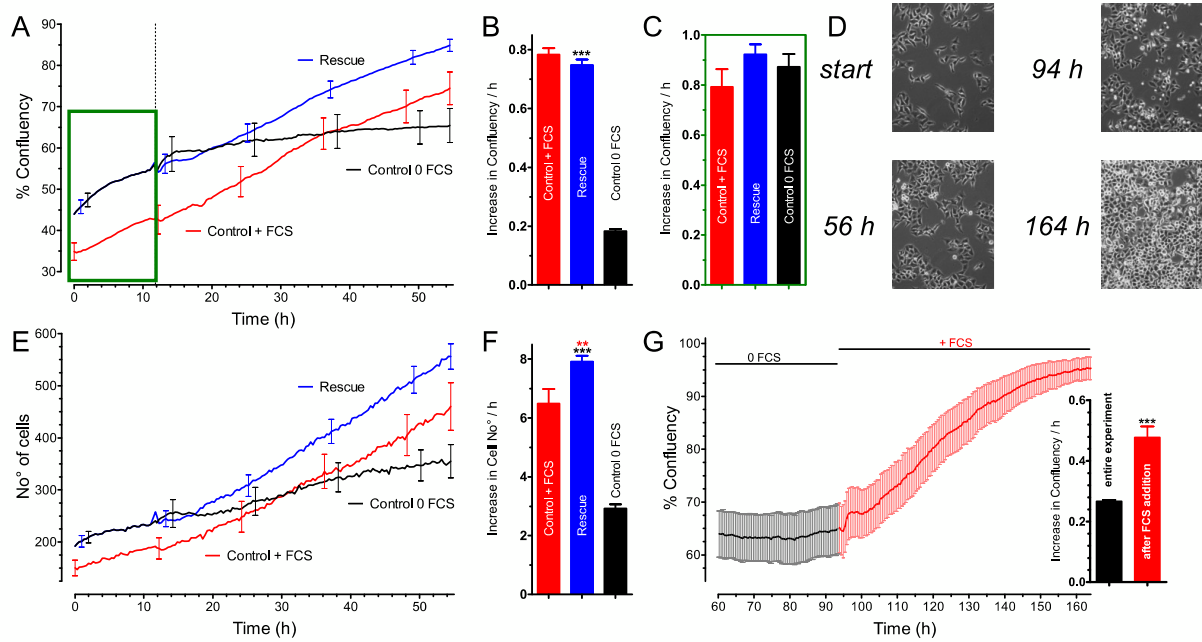


Figure (31): Growth of HeLa cells in response to serum starvation. Cells were either incubated in cell culture medium with FCS (red lines or bars, $n=3$) or without FCS (black lines or bars, $n=3$). 12 hours after experiment started, the medium was exchanged to either the same, or FCS was re-applied (Rescue, blue lines or bars, $n=6$). **A**: Time course of the confluency. **B**: Slope of confluency after re-addition of FCS. $***p<0.0001$ vs. Control 0 FCS. **C**: Slope of confluency before re-addition of FCS, indicated by the green box in A. **D**: Representative images of cells incubated FCS-free for 92 hours and illustrating the subsequent rise in cell growth. **E**: Time course of the total cell number. **F**: Slope of cell number after re-addition of FCS. $**p=0.006$ vs. Control + FCS. **G**: After cessation of experiment, the serum-free control was further observed (black line). After 92 hours, medium was again exchanged and FCS re-applied (red line). The inlay bar chart shows the slope of confluency over the whole experiment (black) or after FCS re-addition (red).

image) and without (2.9 cells / h / image) serum. This indicates, that a short period of a couple of hours of serum starvation can substantially increase cell division of tumor cells.

3.2.1. Prolonged Serum-Starvation of HeLa Cells Reduces Proliferation Rate and can be Rescued even after 94 Hours of Starvation

When this experiment was finished, I recognized that those cells which were incubated in serum-free medium for 56 hours still did not show a notable increase in dead cells. Those cancerous cells seemed to respond to lack of FCS by down-regulating their division rate. In order to find out, how long HeLa cells would survive serum starvation before an increase in cell death occurs, I continued to observe those serum-free controls (representative images are shown in figure 31 D). 94 hours after serum removal those cells were still viable but dormant concerning cell division. At this state a change of the medium would be necessary, if the cells were kept in regular cell culture conditions. Thus, I decided to change the medium and re-apply FCS, in order to unveil if the cells were still able to strive after such a

long period of serum deprivation. Indeed, after re-addition of FCS at 94 hours, the cells started to proliferate again (Figure 31 G), quantified by the significantly increased slope of confluency after FCS re-addition (red bar of the inlay diagram) compared to the slope of the entire experiment (black bar).

3.3. Endothelial Cells reduce Migration in Response to Serum and Nutrient Starvation

In a further set of experiments, I wanted to detect how starvation of serum and nutrients influences the migration of endothelial cells. As described above (Figure 23), I showed the wound width in pixels of each image of either a scratch (Figure 34) or insert assay (Figures 32 and 33) and calculated the slope of wound closure from this data. By this, I precluded the percentage bias of migrational assays.

3.3.1. Endothelial Cell Migration Requires Serum irrespective of the Concentration

In the first experiment presented (Figure 32), my objective was to detect the optimal concentration of FCS in order to stimulate cell migration. The previously used concentration

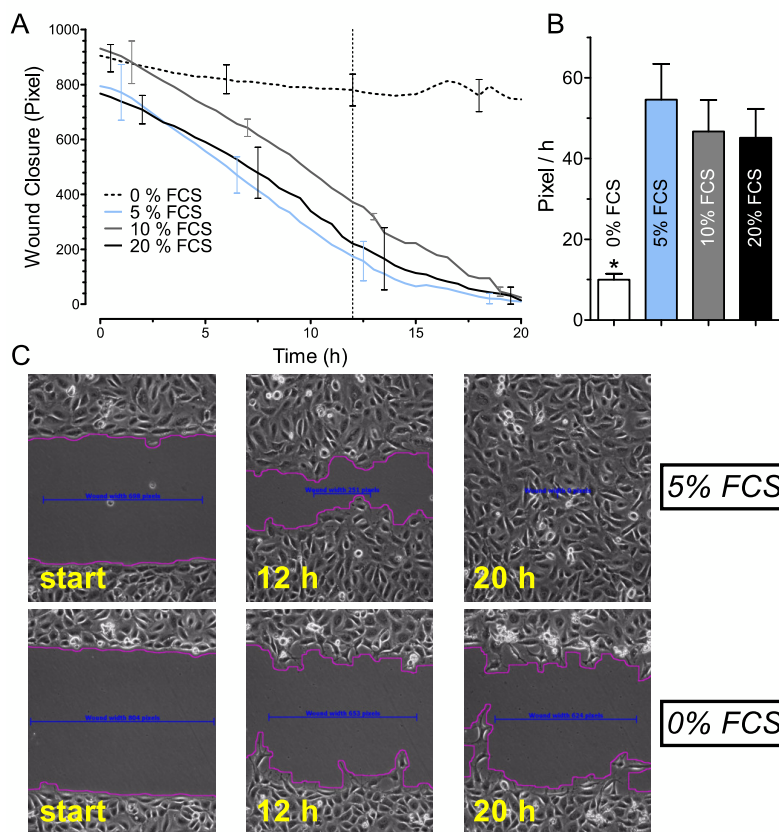


Figure (32): Migrational ability of EC grown in cell exclusion zone inserts. Cells were stimulated with 0%, 5%, 10%, or 20% FCS ($n=3$). **A**: Gap closure shown as decline in gap width. **B**: Bar charts indicate the inverse slope from A in pixels per hour for the first 12 hours (vertical dotted line in A). $*p<0.05$ vs. FCS presence. **C**: Representative images of WH assay of EC stimulated with 5% (top panel) or absence of FCS (bottom panel) at start, 12 hours, and 20 hours, respectively.

was our standard cell culture medium concentration of 10%. I compared the stimulatory potential of three FCS concentrations (5%, light blue curve and bar; 10%, gray curve and bar; 20%, black curve and bar) to serum-free medium (0%, black dotted curve and unfilled bar). As expected, the slope of migration for the first 12 hours of the experiment (Figure 32 B) was almost abolished in absence of FCS (9.9 pixel / h).

Interestingly, the velocity of migration was comparable irrespective of the actual concentration of FCS. The lowest concentration of 5% FCS even held a modestly increased migration slope of 54.5 pixel per hour compared to 10% (46.7 pixel / h) and 20% (45.1 pixel / h), respectively.

3.3.2. Glucose Starvation has only Minor Influence on Endothelial Cell Migration

In the next shown experiment (Figure 33), I additionally included the effect of glucose removal on the migrational ability of EC. Interestingly, removal of glucose (gray line and bar) only insignificantly reduced the pace of wound closure in presence of FCS compared to glucose containing medium (red line and bar). Furthermore, I confirmed the previous result that absence of FCS (black dotted line, white bar) significantly decreases EC migration.

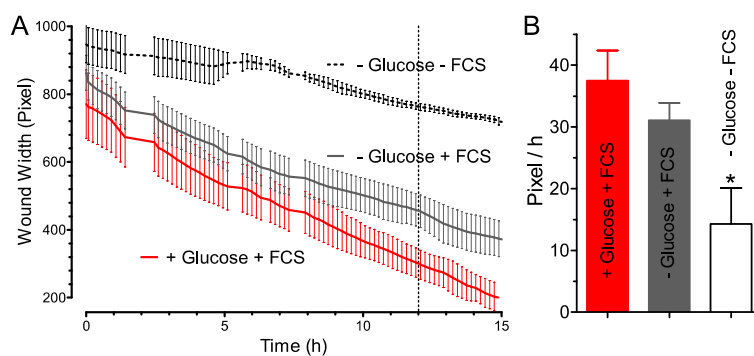


Figure (33): Cells were incubated in cell culture medium containing 10% FCS and 5.5 mM glucose (n=3), 10% FCS and no glucose (n=6), or no FCS and no glucose (n=3). **A:** Gap closure shown as decline in gap width. **B:** Bar charts indicate the inverse slope from A in pixels per hour for the first 12 hours (vertical dotted line in A). * $p < 0.05$ vs. both conditions containing FCS.

3.3.3. Previous Starvation of Primary EC decreases Migration Velocity

In another set of experiments, I was able to test, if primary EC also mitigate their migration in response to starvation. For those experiments I received porcine aortal EC (PAEC) from the Institute of Pharmacology of the Medical University of Graz on 35 mm dishes. Since we could not replat those cells in our cell culture, I was not able to perform an insert migration assay. Accordingly, I had to perform a scratch assay on the ACLSM. At the time of the experiment, I was only able to observe two 35 mm dishes simultaneously.

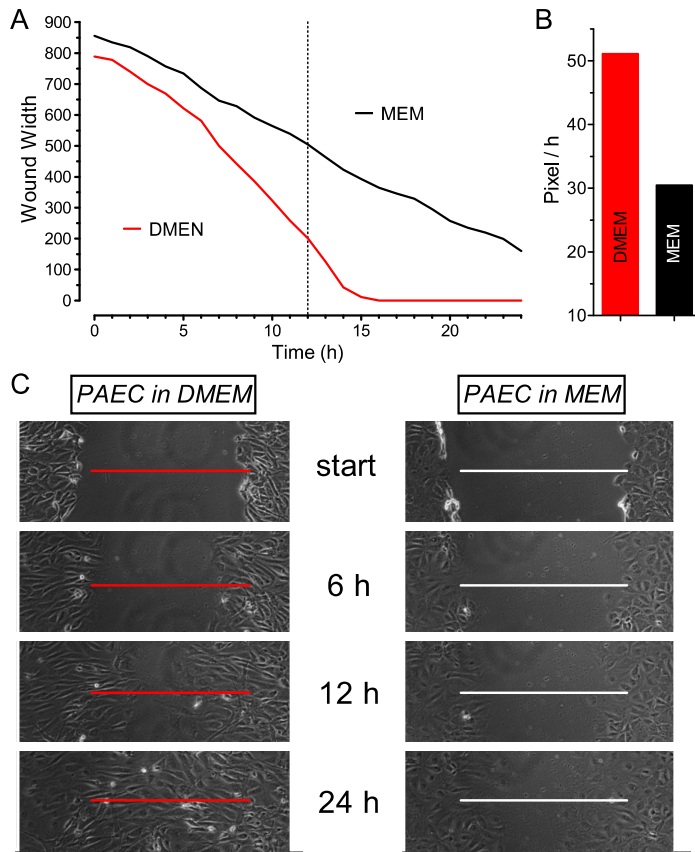


Figure (34): Migrational ability of porcine aortal endothelial cells (PAEC) manually analysed from a scratch assay. Cells were incubated in Eagle's minimal essential medium (MEM) or Dulbecco's Modified Eagle Medium (DMEM) for five days prior to experiments as indicated. During image acquisition, both conditions were stimulated with 10% FCS in experimental buffer (n=1). **A**: Gap closure shown as decline in gap width, estimated by manually measuring gap width. **B**: Bar charts indicate the inverse slope from A in pixels per hour for the first 12 hours (vertical dotted line in A). **C**: Representative images of DMEM and MEM pre-incubated PAEC's at start, 6 hours, 12 hours, and 24 hours, respectively. Red line (DMEM) and white line (MEM) represent gap width at beginning of the experiment.

Thus, each condition was only observed once and no statistic could be drawn (Figure 34). Before the image acquisition started, the cells were incubated in our cell culture for five days. In this period, one dish of cells was incubated in Dulbecco's Modified Eagle Medium (DMEM, red line and bar), while the other cells were kept in Eagle's minimal essential medium (MEM, black line and bar), representing a modest starvation. Before the experiment, the medium of both DMEM- and MEM-incubated cells was exchanged for experimental buffer containing 10% FCS as migration stimulus.

As can be seen by the inception point of the experiment, the initial wound width of both scratches was satisfactorily comparable (DMEM: 788.2 pixel, MEM: 855.8 pixel; Figure 34 A and C). As expected, the cells pre-incubated with DMEM had a considerably higher migration velocity than those treated with MEM (Figure 34 B; 51.1 pixel / h vs. 30.5 pixel / h).

3.4. Various Cell Lines respond differently to Serum and Nutrient Starvation

The aim of the following experiments was to compare the effect of nutrient - or more precisely glucose - starvation of the mostly used cell lines of our laboratory, namely the

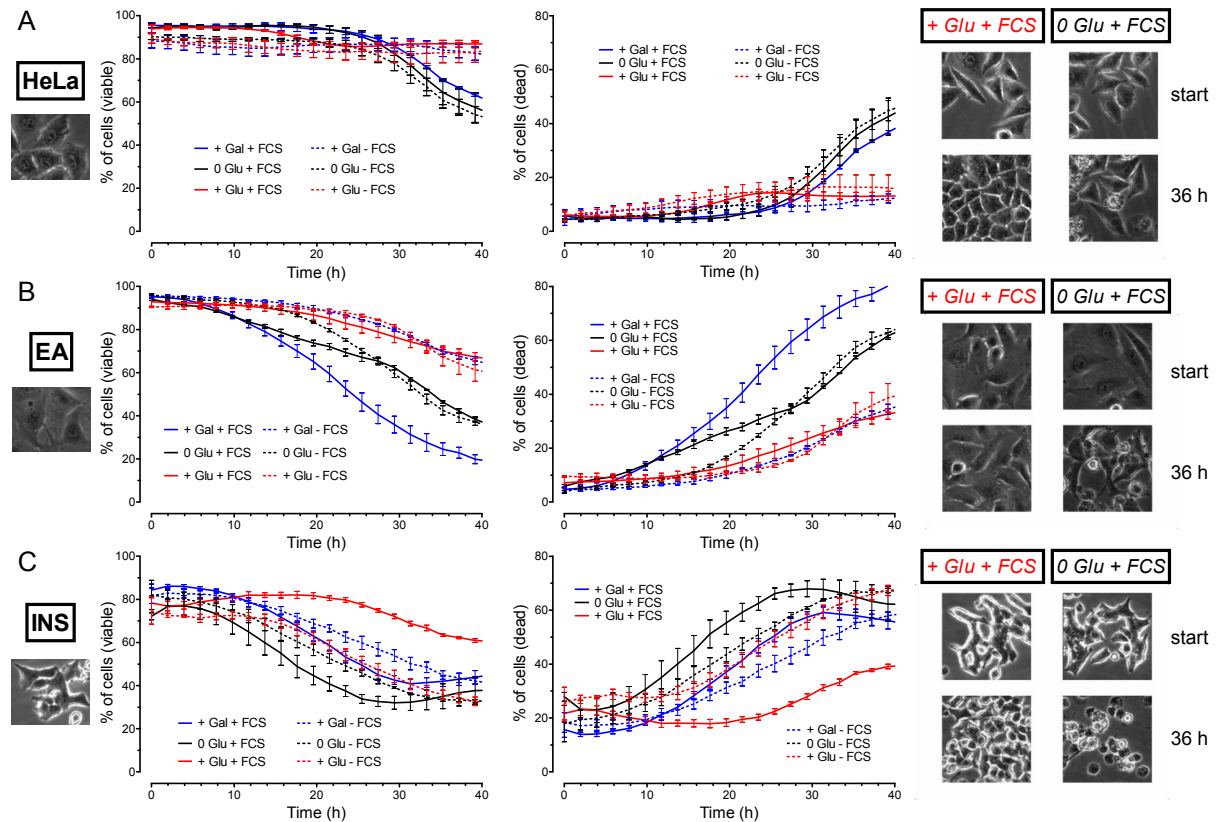


Figure (35): Viability assay in response to different media compositions (see Table 4) of **A:** HeLa cells, **B:** EA.hy926 cells, and **C:** INS-1 cells in the course of 40 hours ($n=3$). *Left panel:* Percentage of viable cells. *Middle panel:* Percentage of dead cells. *Right panel:* Representative images of each cell type at beginning of experiment and 36 hours later with, or without 10 mM glucose present.

EC EA.hy926, HeLa cells, and the pancreatic *beta* cells INS-1, respectively.

3.4.1. Glucose-Starved HeLa Cells Decrease Viability after 29 Hours

In a first experiment I intended to apply a rather physiologic condition of starvation (Figures 35 and 36). The cells were incubated in their standard cell culture medium, hence in any case no complete nutrient austerity was applied. Glucose was either present in the normal concentration (+ Glu, red lines), or replaced by the same concentration of mannitol (0 Glu, black lines) or galactose (+ Gal, blue lines). In order to keep a stable and comparable osmolarity of the buffers and media, in cases of glucose starvation mannitol was substituted (Nahman Jr et al., 1992), which is weaker metabolized by mammalian cells than glucose (Stanley et al., 1984).

Additionally, 10% FCS were either added (+ FCS, straight lines) or not (dotted lines, - FCS). The exact composition of each condition is enlisted in Table 4.

Similar to the previous experiment, the kinetics of the viability development in the course of 40 hours of image acquisition is shown. As the number of conditions was much higher

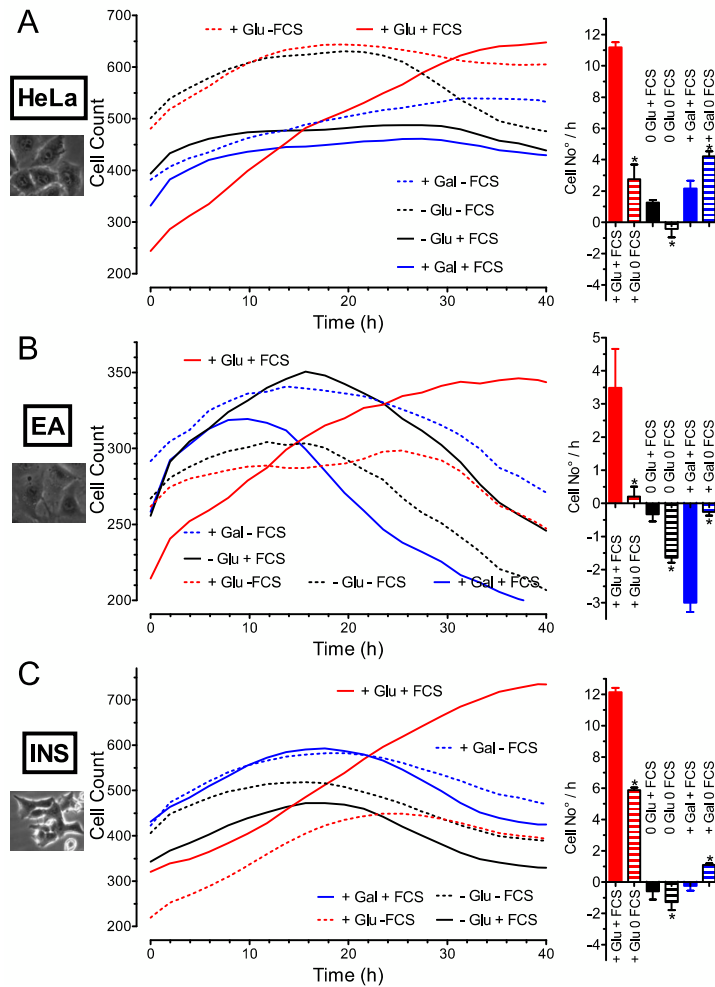


Figure (36): Cell count of the experiment presented in Figure 35 in response to different media compositions (see Table 4) of **A**: HeLa cells, **B**: EA.hy926 cells, and **C**: INS-1 cells in the course of 40 hours ($n=3$, error bars not shown). *Left panel*: Total number of cells. *Right panel*: Slope of cell number during the first 36 hours of image acquisition. $*p<0.05$ + FCS vs. 0 FCS of all conditions.

in this experiment, I plotted the percentage of viable cells (left panels) separately from the percentage of dead cells (middle panels). In order to make the differences of glucose starvation more graspable, exemplarily I also show images of each cell type at the beginning and the end of the experiment, either incubated in glucose-free or glucose-containing medium (right panels).

Notably, each cell type responded differently to the respective conditions, both in terms of kinetics and quality. The viability of *HeLa* cells (Figure 35 A) remained almost unaffected irrespective of the nutrients available until about 29 hours. Afterwards, the cells lacking glucose decreased their viability slowly but steadily, reaching about 50% viability after 40 hours.

3.4.2. Serum-Starvation of HeLa Cells does not Alter Viability but Diminishes Proliferation

Presence or absence of serum seemed to influence the fraction of viable cells only marginally, in line with the experiment of figure 31. However, only those HeLa cells incubated with glucose and FCS increased their cell number considerably over the entire observation pe-

riod (straight red line in Figure 36 A, left panel), with an average increase of 11.2 cells per hour (right panel). All the other conditions yielded a weaker increase in cell number, which basically halted after about 15 hours. This indicates, that one means of handling with energetic stress of these cells, is to restrict cell division, and by this adaptation remain viable.

3.4.3. Endothelial Cells Proliferate Less than HeLa Cells in all Conditions and are more Sensitive to Starvation

The EA.hy926 cells were responding to the applied conditions similar to the HeLa cells, but with a different kinetic pattern (Figure 35 B). In presence of glucose, the cells remained viable with or without further addition of serum for about 24 hours, afterwards a slight viability decrease occurred (about 25% dead cells after 40 hours). However, again similar to the HeLa cells, only those cells with FCS present were proliferating, shown by the increasing total cell number (straight red line in figure 36 B, left panel). The slope of cell number increase was lower than at HeLa cells with 3.5 cells per hour (right panel), the negative slope of the other conditions indicates an increase in dead cells, which tend to form conglomerates that are harder to differentiate as single entities for the Cell-IQ Analyser. But in this cell type, presence of serum had a diminishing effect on viability in the case of glucose deprivation. While cell death appearance started at about 6 hours in FCS containing medium, viability only decreased after about 18 hours in absence of FCS. This might be viewed as an indication, that the cells are better able to tolerate nutrient deprivation, if they are not stimulated to proliferate. This is supported by the higher cell number increase of the 0 Glu + FCS (Figure 36 B, straight black line) EA.hy926 cells compared to the 0 Glu 0 FCS cells (dotted black line).

3.4.4. Galactose Promotes more Cell Growth in Absence of Serum

So far I solely presented the effect of glucose and FCS deprivation of these three cell lines. But in this experiment I also substituted glucose by another monosaccharide, galactose. Galactose is a hexose like glucose. Within a cell, galactose is metabolized and can fuel glycolysis, and hence should theoretically substitute for lack of glucose in terms of ATP generation. However, the enzymes involved in metabolising glucose and galactose slightly differ, e.g. galactose bypasses the hexokinase, which mediates the first and partly rate-limiting reaction of the canonical glucose glycolysis.

Noteworthy, in all cell types tested, substitution of glucose by galactose could only rescue viability in the absence of FCS (Figure 36 and Table 4). In contrast, in both glucose presence or absence (substituted by non-metabolized mannitol) the cells showed a significantly higher cell number slope if FCS was present.

Cell Type	Medium	Sugar	Serum	Cell Count Slope
1	<i>HeLa</i>	5.5 mM glucose	10% FCS	11.2 cells / h
2		10 mM galactose	10% FCS	2.2 cells / h
3		none	10% FCS	1.3 cells / h
4		5.5 mM glucose	none	2.8 cells / h
5		10 mM galactose	none	4.2 cells / h
6		none	none	-0.4 cells / h
7	<i>EA.hy926</i>	5.5 mM glucose	10% FCS	3.5 cells / h
8		10 mM galactose	10% FCS	-3.0 cells / h
9		none	10% FCS	-0.3 cells / h
10		5.5 mM glucose	none	0.2 cells / h
11		10 mM galactose	none	-0.3 cells / h
12		none	none	-1.6 cells / h
13	<i>INS-1</i>	11 mM glucose	10% FCS	12.1 cells / h
14		10 mM galactose	10% FCS	-0.2 cells / h
15		none	10% FCS	-0.6 cells / h
16		11 mM glucose	none	5.9 cells / h
17		10 mM galactose	none	1.1 cells / h
18		none	none	-1.3 cells / h

Tab. (4): Conditions used in the experiment presented in Figures 35 and 36. The cell count slopes are calculated from the first 36 hours of the experiment and shown in Figure 36, right panel.

This was supported by the finding, that the viability of HeLa and EA.hy926 cells was elevated in galactose containing medium, if FCS was absent (Figure 35, blue dotted lines). This also appeared to be the case for the INS-1 cells, but less clearly, as viability decreased in both conditions. In presence of FCS, however, no rescue effect of galactose was observed, in fact at least in EA.hy926 cells, cell death occurrence was even increased.

3.4.5. Pancreatic β -Cells are more Susceptible to Starvation than HeLa and Endothelial Cells

Finally, the *INS-1* cells required both glucose and FCS in order to remain viable (Figure 35 C). In all the other conditions, the viability started to decrease between 8 and 12 hours after the experiment was initiated. Like with the other two cell lines, the INS-1 cells did proliferate mostly in presence of both glucose and FCS (Figure 36 B), with a slope of 12.1 cells per hour. Remarkably, those cells with glucose but without FCS were also substantially proliferating, shown by the slope of 5.9 cells per hour. This occurred mainly within the first 20 hours of the experiment, after which dead cells accumulated.

In another experiment, the glucose starvation was applied by incubation in an experimental buffer with (straight lines) or without (dotted lines) 10 mM glucose (Figure 37). In this case, glucose was not replaced by mannitol. Typically, this buffer is used during measurements of intracellular signals, e.g. the Ca^{2+} or ATP concentration in various compartments of a cell. For this canonical purpose, the buffer is generally applied to the cells for only a couple of minutes. The exact composition is shown in methods. Essentially,

apart from 10 mM glucose it contains no other nutrients like amino acids, pyruvate, or other sugars. In this buffer, even in the presence of glucose, the cells exhibited almost no cell division. For this reason, I decided to plot the cellular viability determined by morphology analysis of the Cell-IQ Analyser. The red lines reflect the fraction of viable cells, the black lines the dead cells.

Interestingly, each cell type responded differently to prolonged incubation in this buffer with or without glucose. The EA.hy926 cells (Figure 37 A) held the most obvious response to starvation. While the EC kept in glucose containing buffer were quite stable and developed almost no increase in dead cells, removal of this carbohydrate led to a steep decrease in viability after about 7 hours. At 12 hours of glucose starvation almost the entirety of cells were dead. However, until about 6 hours both conditions appeared quite similar, showing that these EC can tolerate complete lack of nutrients for several hours without drastic morphological alterations.

In HeLa cells (Figure 37 B) to the contrary, in this setup, presence of glucose only slightly mitigated the decrease in viability. In both cell conditions, cell death occurred already after about 3 hours. Subsequently, slowly the fraction of dead cells increased. Only after about 13 hours a difference of both conditions crystallized, whereafter the cell death was elevated in the glucose-free cells compared to glucose presence. Finally, after 20 hours of the experiment, 59.5% of the HeLa cells incubated with glucose appeared dead, whereas 85.9% of glucose-starved cells died.

The most unexpected finding of this experiment was found in the INS-1 cells (Figure 37 C). Similar to the HeLa cells, the difference in viability due to glucose starvation was far less prominent than for the EA.hy926 cells. First of all, the kinetics of the viability decline of both conditions were distinctly faster than at either of the other cell types, in fact so fast, that at the start of the experiment the viability was already at about 80% for both conditions. Secondly and more interestingly, the decrease in viability occurred prompter in the presence of glucose. Between about 1 hour and 5.5 hours of the experiment, significantly more cells appeared "dead" in the presence of glucose than in those lacking glucose.

Notably, in cases of EA.hy926 and HeLa cells, the Cell-IQ Analyser was taught to recognize "viable", "dead", and "dividing" cells, although the number of actually dividing cells was low. In these cell types, often a obviously dead cell is recognized as "dead", while at the start of the image series a "dividing" cell likely represents a "viable" cell. Nonetheless, due to limitations in the accuracy of the program to determine the different cell types, this classification was kept. Thus, in order to receive a more realistic number of the cell types, the "dividing" cells were added to the "viable" cells at the first part (EA.hy926 cells: until 7 hours, HeLa cells: until 10.5 hours) of experiment, afterwards the "dividing" cells were viewed as "dead". Still, the initial viability of only about 95% and

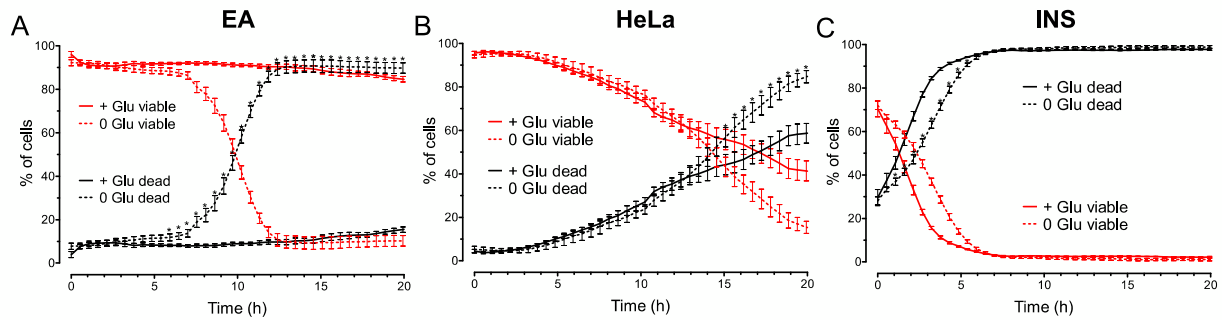


Figure (37): Viability assay of **A**: EA.hy926 cells, **B**: HeLa cells, and **C**: INS-1 cells in the course of 20 hours ($n=4$). Cells were kept in experimental buffer containing either 10 mM glucose (+ Glu, continuous line) or 10 mM mannitol (0 Glu, dotted line). Red lines represent viable cells, black lines represent dead cells. * $p < 0.05$ vs. 0 Glu

the final viability of about 6% are evidence of the limitation of the morphology analysis, which is for most cell types and conditions tested unable to determine cell types with 100% accuracy, as explained above.

In the case of INS-1 cells, the Cell-IQ Analyser was taught to only differentiate "viable" and "dead" cells, hence the final viability reached a level of about 1%.

3.4.6. Re-addition of Glucose Rescues Starved HeLa Cells and Transiently Enhances their Division Rate

As illustrated before (Figures 35, and 36, 37), glucose austerity leads to an increase in cell death. This was accompanied by a drastic reduction in cell proliferation prior to cell death occurrence, indicating a halt in cell division as a means of dealing with energetic stress. Especially in the HeLa cells, which typically have the highest division rate of the cell types used, this notion is graspable.

Therefore, the last experiment presented in this section was conducted to determine how long HeLa cells can be deprived of glucose and still continue to strive normally after read-dition. This experiment was performed in experimental buffer, as the main aim was to find a condition for intracellular Ca^{2+} and ATP measurements, that optimally modelled starvation and not starvation-induced cell death.

Accordingly, about 50% confluent HeLa cells grown on a 24-well plate, giving eight triplicate conditions, were used. One condition was experimental buffer with glucose and other nutrients, every other well was incubated with experimental buffer without glucose and amino acids, but with pyruvate and mannitol as osmolarity substitution. The next triplicate was incubated in glucose-free buffer for the entire experiment and used as a negative control.

After six different timepoints (6 hours, 8 hours, 10 hours, 12 hours, 14 hours, and 16 hours, respectively) of image acquisition, the buffer was exchanged to the normal nutrient

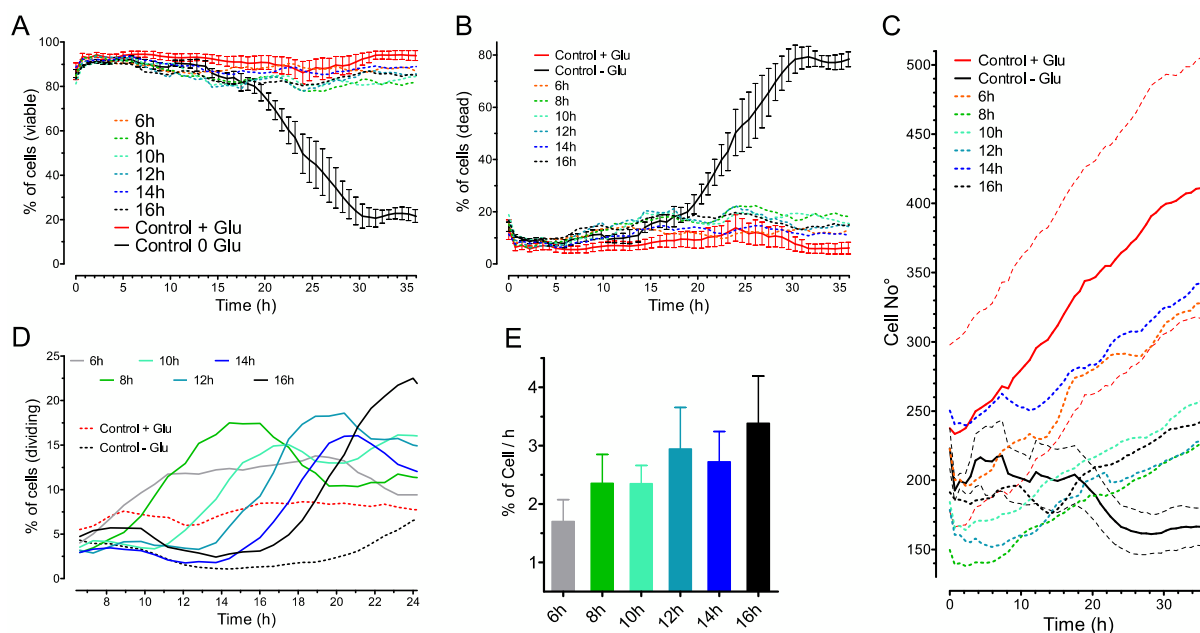


Figure (38): Starvation induced cell death of HeLa cells can be rescued by re-addition of nutrients. Cells were incubated in experimental buffer with (Control + Glu, red lines) or without nutrients (Control 0 Glu, black lines). This buffer contained no glucose or amino acids, but pyruvate. All other conditions were first kept in glucose-free buffer. After 6, 8, 10, 12, 14, or 16 hours glucose was re-added ($n=3$, the standard error is only shown for both controls). **A**: Percentage of viable cells (cells recognized as "viable" and "dividing"). **B**: Percentage of dead cells. **C**: Total number of cells. **D**: Percentage of dividing cell after buffer was exchanged. **E**: Shown is the slope of dividing cells calculated between 1 and 5 hours after the respective buffer exchange.

containing experimental buffer. Subsequently, the same positions were observed further on and finally analysed by Cell-IQ Analyser to determine the number of "viable", "dividing", and "dead" cells, respectively. As before, the percentage of viable cells in Figure 38 A represents those cells recognized as "viable" and "dividing".

In this setup, the viability (Figure 38 A, B) of the glucose-free controls (straight black line with error bars) remained almost unaffected until about 15 hours of the experiment compared to the glucose-containing controls (straight red line with error bars). Then a slow increase in cell death appeared until 20 hours. Thereafter, dead cells started to accumulate more rapidly, at 30 hours virtually all the cells perished. The final plateau of about 80% dead cells once more indicates the limitations of the morphology analysis, although the overall tendency could well be quantified.

In line with the experiments presented before, the cells incubated without glucose showed a limitation in proliferation, reflected by an almost stable total cell number (Figure 38 C, straight black line with error bars) compared to a nearly duplication of glucose-treated controls (straight red line with error bars) and almost twice as many dividing cells at each timepoint (Figure 38 D).

While no drastic change in viability was observed in the conditions with glucose re-addition

(Figure 38 A and B, coloured dotted lines), the total cell number was, expectedly intermediary between both controls. With this experiment, I unveiled, that even after 16 hours of nutrient starvation HeLa cells were able to recover. Additionally, I recognized a transient increase in cell division upon glucose addition (Figure 38 D). This occurred relatively consistent with a delay of 90 minutes. I had the impression, that the longer the time of starvation, the more cell division was ignited. Thus, I calculated the slope of dividing cells between 1 and 5 hours after the respective glucose re-addition. Although no statistically significant differences in the slopes were achieved, the tendency of more distinct cell division increase after a prolonged period of starvation can be drawn (Figure 38 E).

4. Effect of Altering the Mitochondrial Ca^{2+} Uptake Machinery

One main research aim of our laboratory is to better understand the mitochondrial Ca^{2+} regulation and to identify and characterize the proteins involved in this process (Graier et al., 2007). Accordingly, I conducted experiments to measure effects of knockdown (KD) or overexpression (oe) of some putative proteins thought to contribute to the mitochondrial Ca^{2+} uptake on cellular viability, proliferation, and migration. Namely, knockdown of Mitochondrial Ca^{2+} Uniporter (MCU, previously known as *CCDC109A*) (De Stefani et al., 2011; Baughman et al., 2011) and Mitochondrial Ca^{2+} Uptake 1 (MICU1, previously known as *CBARA1*), (Perocchi et al., 2010) as well as overexpression of Uncoupling Protein 3 (UCP3) (Trenker et al., 2007) was tested. Additionally, experiments with Annexin A5 (ANXA V), a commonly used marker to differentiate live from dead cells, that was described to localize to mitochondria (Sun et al., 1993) were performed.

4.1. Stable Knockdown of MCU does not influence Viability or Proliferation of HeLa Cells

After a downright hunt over the last five decades to identify the molecular players of mitochondrial Ca^{2+} influx, a substantial progress was made with the discovery of MCU (Raffaello et al., 2012).

Since mitochondrial Ca^{2+} is an important determinant of cell death and metabolism, I expected cells that lack MCU to have a hampered proliferation rate, to be more susceptible to starvation, and less responsive to induction of mitochondrial apoptosis. With the availability of a stable MCU knockdown HeLa cell line (MCU KD, tebu-bio) in our laboratory, I was able to test those hypotheses.

Initially, it was recognized, that the MCU KD cells morphologically do not differ much

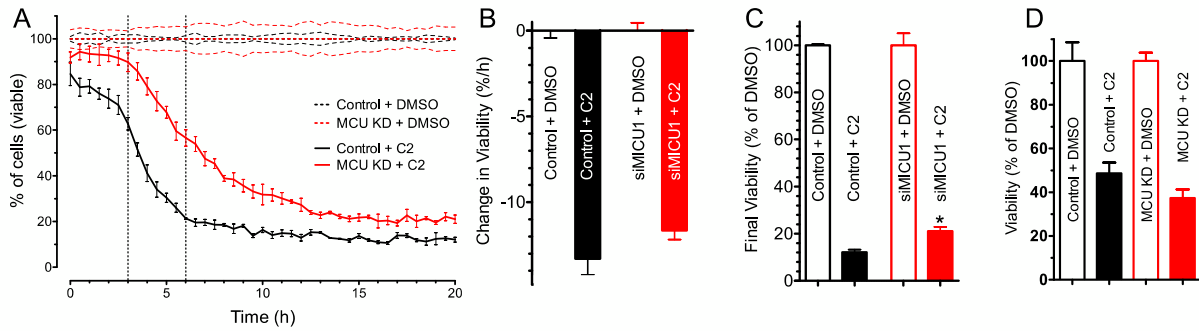


Figure (39): Viability of stable MCU knockdown HeLa cells (MCU KD, red lines and bars) or control HeLa cells (black lines and bars). Cell death was induced by 40 μ M C2-Ceramide, controls were treated with equal amount of DMSO. **A:** Morphology analysis by Cell-IQ Analyser (n=3). The number of viable cells is normalized to the respective DMSO-treated controls (dotted lines). **B:** Slope of viability between 3 and 6 hours of experiment (vertical dotted lines in A). **C:** Comparison of the final viability at 20 hours from A. *p=0.0134 vs. Control + C2. **D:** MTT assay similar to Figure 41.

from control HeLa cells (Figure 40 D and Figure 43 F).

In the first experiments presented (Figure 39), I induced apoptosis in control (black lines and bars) or MCU KD (red lines and bars) HeLa cells using 40 μ M C2-Ceramide (straight lines, filled bars) or equal amount of the solvent DMSO as control (dotted lines, unfilled bars). Viability was calculated in relation to the DMSO-treated controls of both cell strains (Figure 18). While no difference was recognized in the pace of cell death appearance (Figure 39 A and B), shown as the slope of viable cells between 3 and 6 hours after cell death induction (vertical dotted lines in A), the final percentage of viable cells after 20 hours was slightly higher in MCU KD cells compared to control HeLa cells (Figure 39 C). This was in accordance with my expectations.

However, this difference shows once again the limitation of the Cell-IQ Analyser to determine the exact numbers of various cell types. No doubt, the tendency could clearly be drawn, but at about 15 hours literally all the C2-treated cells seemingly appeared dead, while the Cell-IQ Analyser estimated a viability of about 20%. In line with this limitation, in a control MTT assay (Figure 39 D), that determines the metabolic activity of a cell population, this increased viability of MCU KD cells could not be replicated. Here, cell death was also induced by 40 μ M C2-Ceramide. 20 hours later, metabolic activity was colorimetrically determined. Thereby, no significant difference between control and MCU KD HeLa cells was seen, the controls were even slightly more viable, though not significantly (48.6% vs. 37.3%).

In another experiment (Figure 40), I measured the proliferation rate of the MCU KD HeLa (filled bars) compared to controls (unfilled bars) in presence (red bars) or absence (black bars) of 10% FCS. Additionally, a rescue attempt was induced, similar to the experiment of Figure 31, in which FCS was reapplied to serum-starved cells after 24 hours (blue bars). Due to confusingly many conditions, I decided not to plot the anyways very much similar

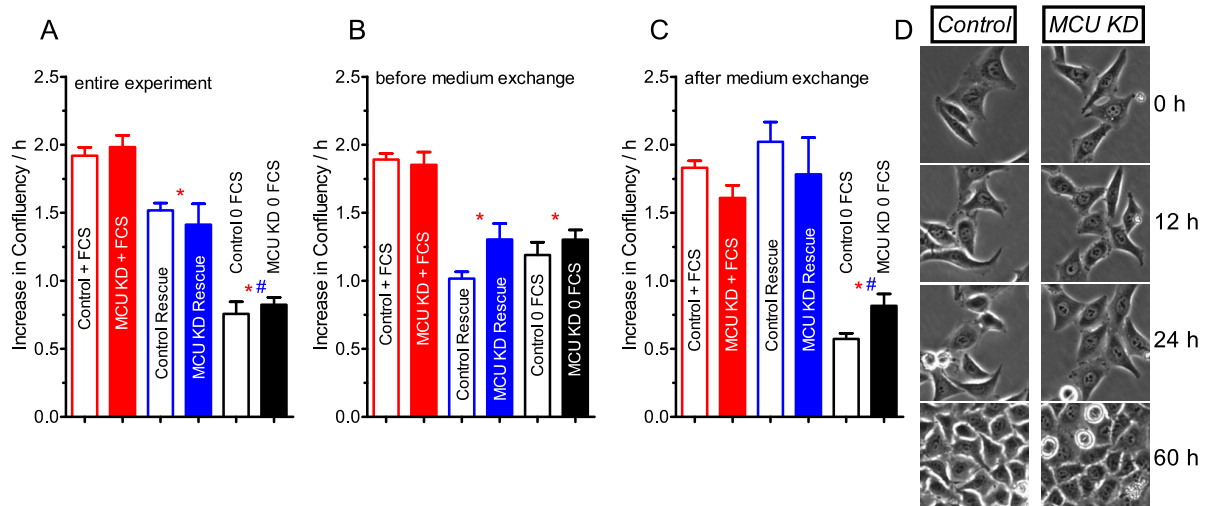


Figure (40): Proliferation of stable MCU knockdown HeLa cells (MCU KD, filled bars) or control HeLa cells (unfilled bars) determined from Figure 39. Cells were either incubated in presence (red bars) or absence (black bars) of 10% FCS. After 24 hours, a third condition was introduced by re-adding FCS (Rescue, blue bars) to serum-starved HeLa cells (similar to Figure 31). **A:** Slope of change in confluency over 48 hours. **B:** Slope of change in confluency over the first 24 hours, before FCS re-addition. **C:** Slope of change in confluency over the second 24 hours, after FCS re-addition. **D:** Representative images of Control and MCU KD HeLa cells at start, 12, 24, or 60 hours of the experiment in presence of serum. * $p < 0.05$ vs. Control or MCU KD + FCS, # $p < 0.05$ vs. Control or MCU KD Rescue.

growth curves, but rather show the growth slopes for the entire experiment (Figure 40 A, 48 hours), the time before FCS was reapplied (Figure 40 B, first day), and the time after medium exchange (Figure 40 C, second day), shown as the percentage increase in confluency per hour.

Irrespective of the period and condition considered, there was no significant difference between the growth of MCU KD and control HeLa cells. However, after a prolonged period of starvation (Figure 40 C, black bars) the MCU KD cells were slightly faster proliferating, though insignificantly. On the other hand, in serum-containing medium, the proliferation rate was slightly lower compared to control cells. This last note was confirmed by trend in another experiment (Figure 43 D)

Further, I found that after readdition of serum both HeLa strains proliferate as fast as those cells with FCS present from experiment initiation on, while for the entire experiment the slope of the rescue cells was expectedly intermediate between serum presence and starvation.

4.2. Transient Knockdown of MICU1 Makes HeLa Cells Less Susceptible to Apoptotic Cell Death

In the next presented experiment I induced apoptosis in HeLa cells with an siRNA-mediated transient knockdown of MICU1 (red bars) or scrambled siRNA transfected controls (black bars), and subsequently performed an MTT assay similar to Figure 39 D. Interestingly, I found that siMICU1 transfected HeLa cells were less susceptible to apoptotic cell death induction than control HeLa cells, with a final viability compared to DMSO-treated controls of 38.9% and 15.6%, respectively.

This is in clear contradiction to a recent report (Mallilankaraman et al., 2012).

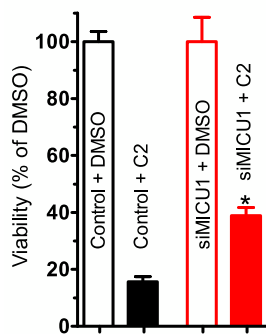


Figure (41): Viability of HeLa cells transfected with siRNA against MICU1 (siMICU1, red bars) or scrambled siRNA (Control, black bars) determined in an MTT assay. Cell death was induced by 40 μ M C2-Ceramide, controls were treated with equal amount of DMSO. After 20 hours of incubation, cell viability was determined as described. Viability was normalized to DMSO treated cells of both controls and siMICU1, respectively. * $p < 0.0001$ vs. Control + C2 (n=6).

4.3. Transient Knockdown of MICU1 Does not Influence Endothelial Cell Migration

In the next experiment, I intended to estimate the migratory potential of transiently knocked down MICU1 EA.hy926 endothelial cells. Recently, it was reported that siRNA-mediated knockdown of MICU1 in endothelial cells would result in a reduction of migration (Mallilankaraman et al., 2012). Thus, my aim was to confirm those results.

However, in a first experiment using the cell exclusion zone inserts (Figure 42 A and C) I surprisingly found that siMICU1 (red line and bar, n=2) treated EA.hy926 cells even migrated slightly, although insignificantly, faster than control cells (black line and bar, n=3), with wound closure slopes of 37.6 and 29.3 pixel per hour, respectively. Originally, both conditions were performed as triplicate on the ACLSM, but unfortunately one siMICU1 condition had to be abolished due to contamination.

Since Mallilankaraman et al. got their result from a scratch assay, I thought that maybe the wounded cells of the scratch might influence the outcome. Thus, I repeated the same experiment performing a scratch assay (Figure 42 B and D, n=1), again yielding no difference in the wound closure slopes between siMICU1 (20.6 pixel / h) and control (20.2 pixel / h).

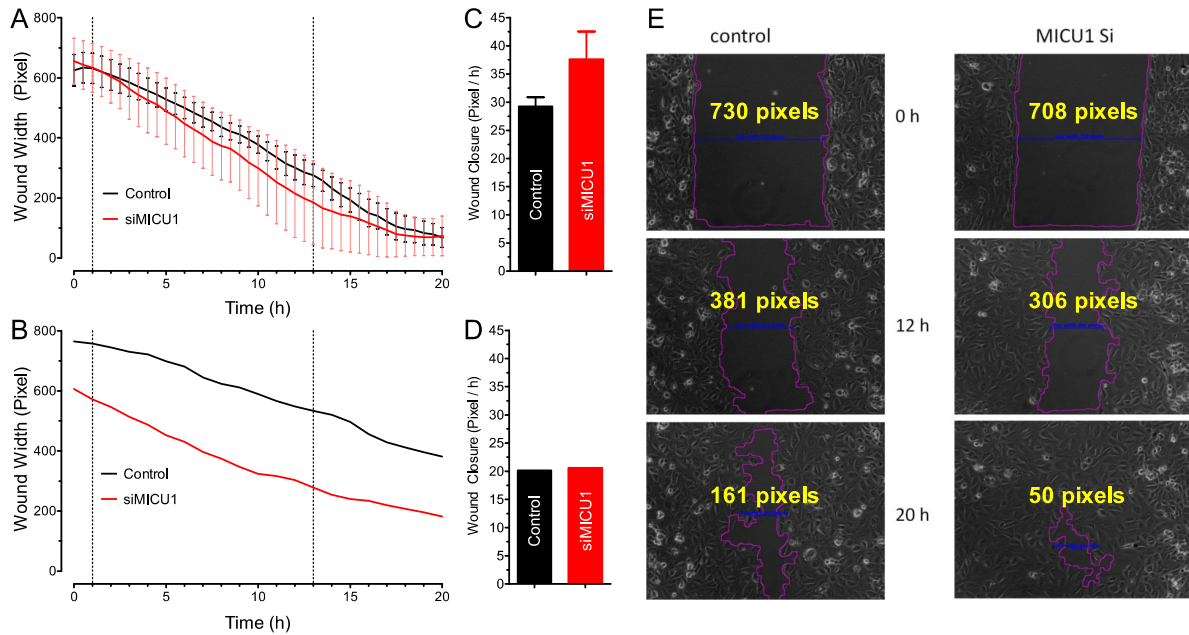


Figure (42): Migrational ability of EC transfected with either siRNA against MICU1 (red lines or bars) or scrambled siRNA (black lines or bars). **A:** Cell exclusion zone insert assay (n=3 for Control and n=2 for siMICU1). **B:** Scratch assay (n=1). **C:** Slope of wound closure in pixels / h from A between 1 h and 13 h of experiment (vertical dotted lines in A). **D:** Slope of wound closure in pixels / h from B between 1 h and 13 h of experiment (vertical dotted lines in B). **E:** Representative images from A at start (*top panel*), 12 h (*middle panel*), and 20 h (*bottom panel*).

4.4. Annexin A5 Knockdown Does not Influence Proliferation of HeLa Cells

In the last experiment of this section, I compared the proliferation rate of three HeLa cell strains, stable MCU KD, stable Annexin A5 knockdown (ANXA KD), and control HeLa cells. The cells were further transiently transfected as shown in Table 5.

The presentation of that many different conditions within one figure was a small challenge. By looking at the growth curves showing the change in confluency over 24 hours for Control HeLa cells (Figure 43 A), MCU KD (Figure 43 B), and ANXA V KD cells (Figure 43 C), a difference in the proliferation rate of further transfection with control siRNA (black), siMICU1 (blue), UCP3 overexpression (red), and siMICU1 + UCP3oe (green) is not obviously perceptible. Accordingly, I calculated the growth slopes from these curves and aligned them to the transient transfection (Figure 43 D) or the HeLa strain (Figure 43 E) and flagged significant differences within each group (color refers to compared condition). The exact value for each slope is presented in Table 5.

In any transient knockdown condition, the ANXA V KD cells (Figure 43 D, grey bars) did not differ from the control (black bars) HeLa cells. As in the case of MCU KD cells,

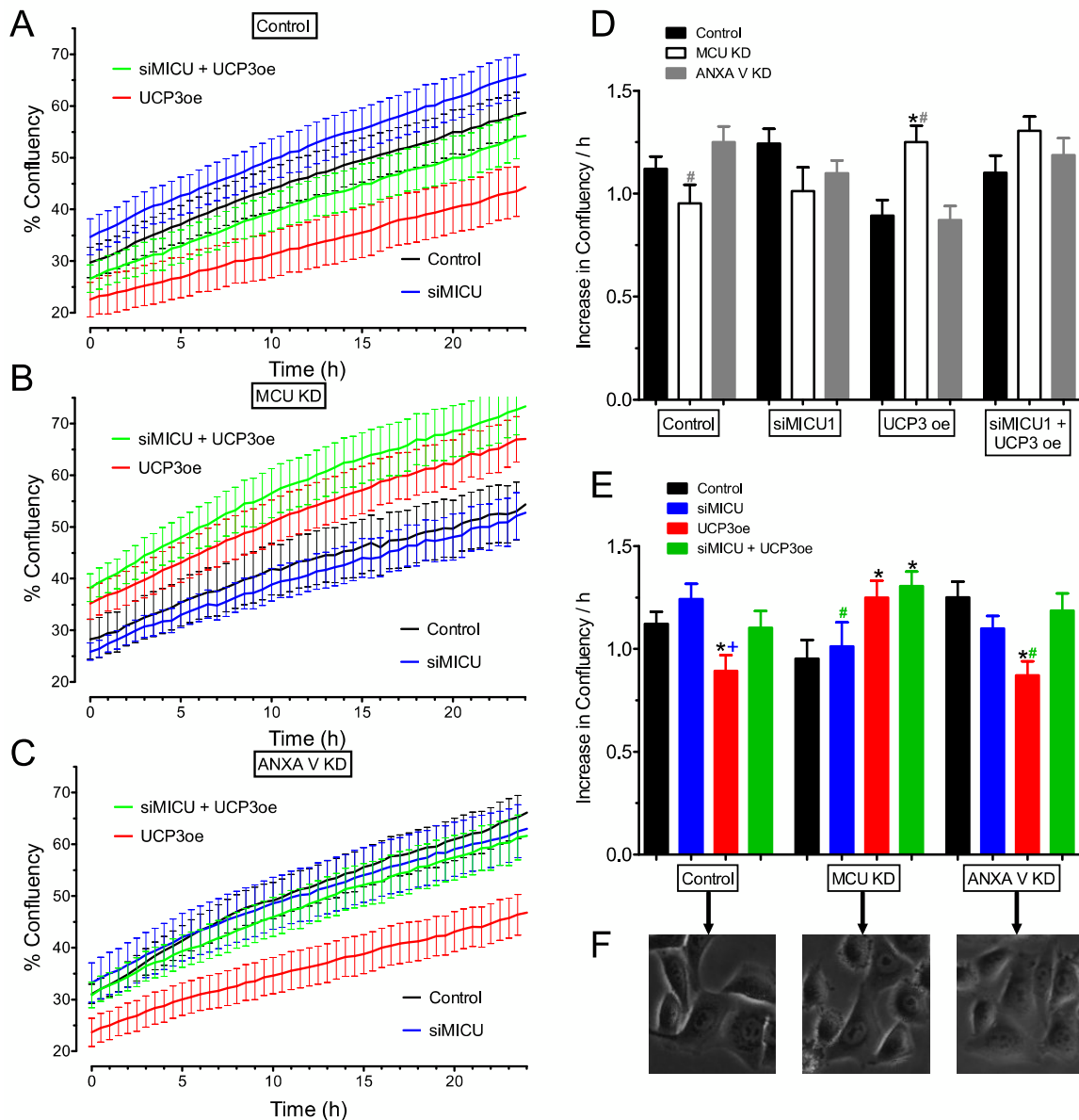


Figure (43): Proliferation of HeLa cells with stable knockdown of MCU, Annexin A V (ANXA V KD) or control cells determined by confluency measurement ($n=4$). Each HeLa cell type was further transiently transfected with siRNA against MICU1 (blue), exogenous UCP3 for overexpression (UCP3oe, red), combination of both (siMICU1 + UCP3oe, green), or scrambled siRNA (Control, black). Cells were plated directly before the experiment started onto two 24-well plates and immediately imaged in Cell-IQ. **A:** Confluency curve of control HeLa cells. **B:** Confluency curve of MCU KD HeLa cells. **C:** Confluency curve of ANXA V KD HeLa cells. **D:** Slope of the increase in confluency over the first 24 hours, aligned to the respective transient transfection condition ($*p<0.05$ vs. Control, $\#p<0.05$ vs. ANXA V KD). **E:** Slope of the increase in confluency over the first 24 hours, aligned to each HeLa cell type ($*p<0.05$ vs. Control, $+p<0.05$ vs. siMICU1, $\#p<0.05$ vs. siMICU1 + UCP3oe). **F:** Representative images of Control, MCU KD, and ANXA V KD HeLa cells to stress that no obvious morphological differences appear.

HeLa Strain	Transient Transfection	Confluency Slope
1	scrambled siRNA	1.12 % / h
2	siMICU1	1.24 % / h
3	UCP3oe	0.89 % / h
4	siMICU1 + UCP3oe	1.10 % / h
5	scrambled siRNA	0.95 % / h
6	siMICU1	1.01 % / h
7	UCP3oe	1.25 % / h
8	siMICU1 + UCP3oe	1.31 % / h
9	scrambled siRNA	1.25 % / h
10	siMICU1	1.10 % / h
11	UCP3oe	0.87 % / h
12	siMICU1 + UCP3oe	1.19 % / h

Tab. (5): Conditions used in the experiment presented in Figures 43. The confluency slopes were calculated from the 24 hours of the experiment of the curves in Figure 43 A, B, and C (n=3).

the ANXA V KD cells did not differ morphologically from control HeLa cells.

4.4.1. ANXA V KD HeLa Cells Have an Increased Proliferation Rate Compared to MCU KD HeLa Cells

Under control siRNA transfection (Figure 43 D), the ANXA V KD cells (grey) grew slightly faster than control (black), while the MCU KD cells (unfilled) were slightly slower proliferating than controls. Both differences were insignificant compared to controls, albeit in sum led to a significant difference between MCU KD and ANXA V KD cells.

4.4.2. Transient UCP3 Overexpression Increases Proliferation in Stable MCU Knockdown HeLa Cells

On the other hand, the MCU KD cells (Figure 43 D, unfilled bars) differed in some transient knockdown conditions from the control HeLa cells (black bars).

While in control siRNA and siMICU1 transient knockdowns, the MCU KD proliferation was insignificantly diminished, in the case of UCP3 overexpression the MCU KD HeLa cells proliferated significantly faster than both control and ANXA V KD cells. If MICU1 was simultaneously knocked down with UCP3oe, this clear difference vanished by an increased proliferation of the controls and ANXA V KD cells, while the MCU KD strain was unaffected in this condition (Figure 43 E, *middle panel*, red vs green bar).

5. Correlation with Intracellular Measurement Assays

In a recent work of our laboratory, we for the first time presented a method to measure ATP within the lumen of the endoplasmic reticulum (ER) specifically and dynamically using a genetically encoded *Förster* resonance energy transfer (FRET) probe (Vishnu et al., 2013). This ER ATP sensor (termed ERAT4.01) allowed us to measure the ATP content within the ER on the single cell level in real-time recordings. We unveiled that this ubiquitous cellular energy current is dynamically controlled within the lumen of the ER depending on the metabolic and energetic state of the cells. Moreover, we found a close inverse coupling between $\text{Ca}^{2+}_{\text{ER}}$ and $[\text{ATP}]_{\text{ER}}$.

In the final section of my thesis, I present several of my experiments, that led to the publication of this paper. I especially emphasized on a correlation of these intracellular measurements on the single-cell level with the proliferation of entire cell populations incubated with similar conditions.

5.1. Higher Proliferative HeLa Cells Have an Elevated Metabolic Rate and $[\text{ATP}]_{\text{ER}}$ Increase upon Ca^{2+} Mobilisation

At some days of measuring $[\text{ATP}]_{\text{ER}}$, we found, that the previously mentioned Ca^{2+} -coupled $[\text{ATP}]_{\text{ER}}$ increase was inconsistently different to other days of the same experiments. At first, we suspected that the confluency of the cells might be deterministic. When we tested this, we could not find a clear correlation between confluency of the cells and the susceptibility of the cells to increase $[\text{ATP}]_{\text{ER}}$ upon Ca^{2+} mobilisation from the ER. Then, we thought that the time elapsed after transfection might be responsible, but again we could not find a clear correlation.

Finally, we thought that instead of transfection, the decisive factor might be the time elapsed after splitting and replating the cells (Figure 44). This would be in line with reports linking cellular detachment from the culture dishes and trypsinization to modulation of metabolism (Page and Lange, 1997; Hardie et al., 2000; Huang et al., 2010). For this purpose, I firstly compared the proliferation rate of HeLa cells split 20 hours before the experiment (20hSC, green lines and bars) with those split 72 hours before the experiments (72hSC, black lines and unfilled bars) determined by the change in confluency over 40 hours. Indeed, I could successfully show, that the 20hSC were proliferating significantly faster than the 72hSC (Figure 44 A-G). To outrule an effect of the confluency, both the 20hSC and the 72hSC were plated in two different concentrations to reach about 40% (low confluency, Figure 44 B-D) or 60% confluency (high confluency, Figure 44 E-G). Both aimed confluencies were received almost perfectly. By chance, both the high and low confluency 20hSC and 72hSC reached a similar confluency 10 hours after the experiment

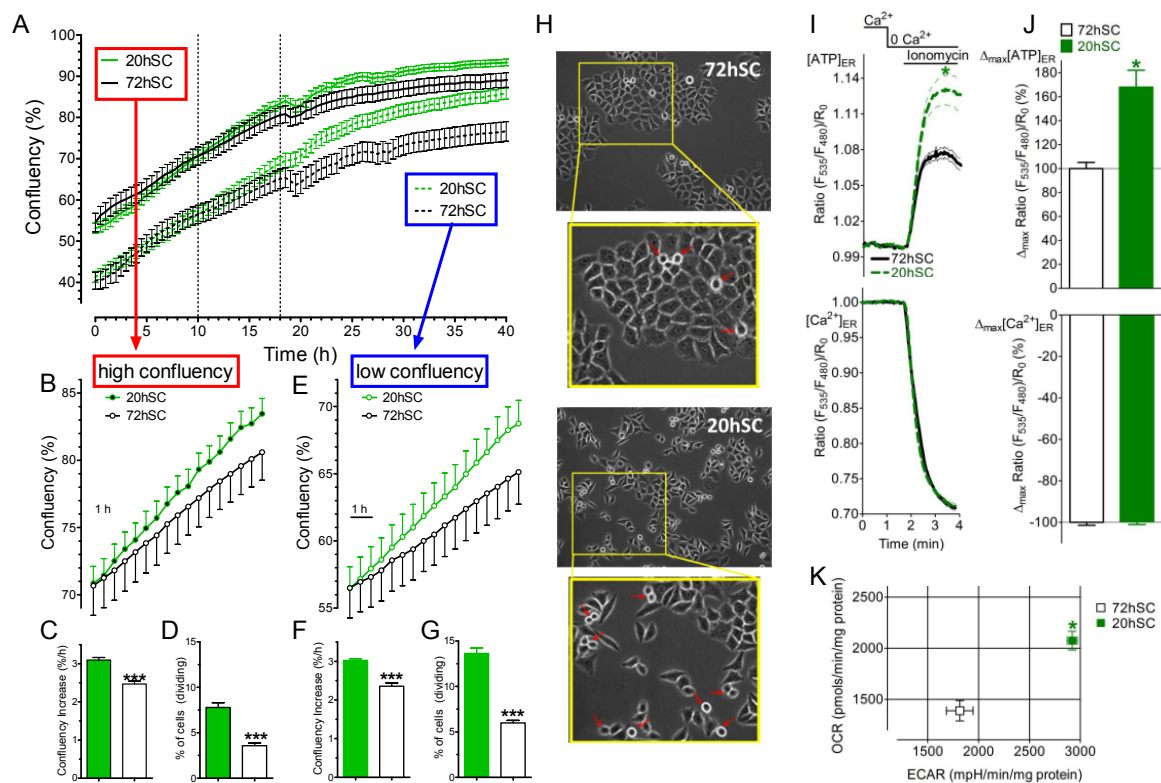


Figure (44): The pace of proliferation of HeLa cells decays with elapsed time after trypsinization and re-splitting, which correlates with a diminished Ca^{2+} -coupled $[\text{ATP}]_{\text{ER}}$ increase and lower metabolic rate. Cells were either observed 20 hours after splitting (20hSC, green lines or bars), or 72 hours after splitting (72hSC, black lines or bars) and simultaneously sequenced. **A:** Proliferation curve of 20hSC and 72hSC determined by confluency measurement of Cell-IQ Analyser over 40 hours. To exclude an effect of confluency on the growth rate, both 20hSC and 72hSC were in two different concentration. This resulted in an initial confluency of about 55% (high confluency) or about 40% (low confluency), respectively. **B:** Zoomed curve of high confluency 20hSC and 72hSC between 10 and 18 hours (vertical dotted lines in A) of the experiment, to yield the same initial confluency of about 70.5%. **C:** Slope of confluency increase during the period of B in % / h. **D:** Average fraction of dividing cells during the period of B. **E:** As B for the low confluency cells (56.5%). **F:** Slope of confluency increase during the period of E in % / h. **G:** Average fraction of dividing cells during the period of E. **H:** Representative images of 72hSC (*top two panels*) and 20hSC (*bottom two panels*). The 20hSC exhibited clearly more dividing cells (red arrows). **I:** Live-cell intracellular measurement of $[\text{ATP}]_{\text{ER}}$ (*top panel*) and $[\text{Ca}^{2+}]_{\text{ER}}$ (*bottom panel*) using FRET-based sensors ERAT4.01 and D1ER, respectively, of 72hSC (black) or 20hSC (green). Ca^{2+} release from the ER was induced by stimulation with 2 μM of the ionophore ionomycin. **J:** Maximal ionomycin-induced response of ERAT4.01 (*top panel*) and D1ER (*bottom panel*) signal. **K:** Data kindly provided by Lukas Groschner. Basal cellular metabolic profiles of 72hSC and 20hSC were analyzed on a Seahorse XF96 extracellular flux analyzer. Absolute oxygen consumption rate (OCR) and extracellular acidification rate (ECAR) were normalized to total cellular protein. As indicated the 20hSC (green square, $n=24$) has a higher metabolic rate as compared to 72hSC (white square, $n=24$). * $p < 0.05$, *** $p < 0.0001$ of 20hSC vs. 72hSC.

was started and the slopes of growth (Figure 44 C and F) and the average fraction of dividing cells (Figure 44D, G, and H) were calculated from this timepoint until 8 hours later (vertical dotted lines in A). At both high and low confluency the increase in confluency per hour of the 20hSC (C and F, 3.1 and 3.0, respectively) was significantly higher than of the 72hSC (D and G, 2.5 and 2.4, respectively). Similarly, significantly more of the 20hSC HeLa cells (7.8% and 13.6%) were dividing than in the same time frame of the 72hSC (3.6% and 6.0%).

The next step was to measure the ATP and Ca^{2+} content of the ER of those cells (Figure 44 I and J). As expected, the higher proliferative 20hSC also showed an almost doubled $[\text{ATP}]_{\text{ER}}$ increase upon Ca^{2+} release using 2 μM of the ionophore ionomycin (upper panel of I and J), as described in methods. At the same time, the release of Ca^{2+} from this organelle was not hampered (bottom panel of I and J).

Finally, the metabolic activity of the 20hSC and 72hSC HeLa cells was compared (Figure 44 K, data kindly provided by Lukas Groschner). In line with our expectations, the 20hSC clearly showed a higher rate of both oxidative phosphorylation (OXPHOS, determined as oxygen consumption rate (OCR) on Y-axis) and anaerobic glycolysis (determined as extracellular acidification rate (ECAR) on X-axis).

As indicated, this last experiment was not performed by me, but I included this data to show another useful application, the correlation between metabolic state of a cell population with its proliferation rate.

5.2. Glucose Starvation Reduces the Ca^{2+} -Coupled $[\text{ATP}]_{\text{ER}}$ Increase and is Restored after 4 Hours

Another major finding of the paper was, that glucose starvation leads to a significant diminishment of Ca^{2+} -coupled $[\text{ATP}]_{\text{ER}}$ increase in HeLa cells. This held true for any condition tested, representatively I show this by means of the 20hSC and 72hSC upon glucose starvation. In this experiment, cells were glucose starved between 2 and 8 hours prior to experiments (Figure 45).

In both 20hSC (Figure 45 A) and 72hSC (Figure 45 D) the $[\text{ATP}]_{\text{ER}}$ increase was significantly lower upon glucose starvation. Noteworthy, this was attended by a lower basal $[\text{ATP}]_{\text{ER}}$ content of both 20hSC (Figure 45 B, 79.1% of glucose presence) and 72hSC (Figure 45 E, 83.8% of glucose presence). The putatively causative Ca^{2+} release upon ionomycin treatment was not affected in case of the 20hSC (Figure 45 C), and minorly hampered in the 72hSC (Figure 45 F).

The diminishing effect of glucose starvation on the Ca^{2+} -coupled $[\text{ATP}]_{\text{ER}}$ increase was observed in every experiment. However, we recognized a variation in the strength of the signal reduction. Accordingly, we analyzed our starvation experiments again and aligned

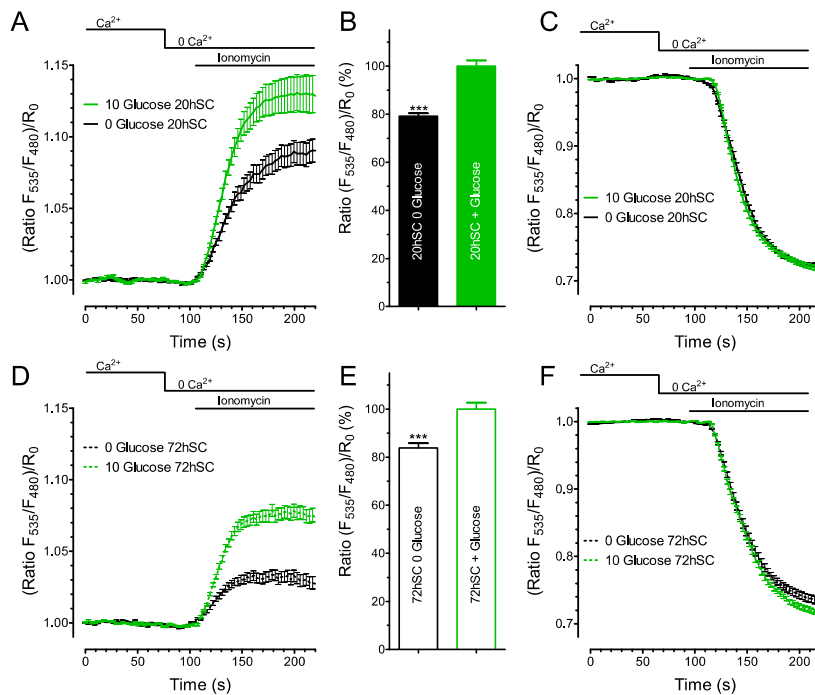


Figure (45): Glucose starvation applied to 20hSC (straight lines and filled bars) and 72hSC (dotted lines and unfilled bars) (see Figure 44). Cells were either pre-incubated in loading buffer containing 10 mM glucose (green lines and bars) or without glucose (black lines and bars). Cells were stimulated with 2 μ M ionomycin. **A:** $[ATP]_{ER}$ signal determined by ERAT4.01 of 20hSC. **B:** Basal $[ATP]_{ER}$ content in relation to 20hSC. **C:** $[Ca^{2+}]_{ER}$ signal determined by D1ER of 20hSC. **D:** As A for 72hSC. **E:** As B for 72hSC. **F:** As C for 72hSC. * $p < 0.05$, *** $p < 0.0001$ of 20hSC vs. 72hSC.

the strength of the Ca^{2+} -coupled $[ATP]_{ER}$ increase to the time of starvation (Figure 46 C, blue line, right Y-axis) in relation to the average response in non-starved cells (orange dotted line, right Y-axis).

This led to the unexpected discovery, that the signal almost immediately decreases to about 12% of non-starved cells (Figure 48 B and C), whereupon it slightly increases to about 30%. But after about 4 hours of starvation the signal recovers to about 80-90% of the non-starved level. On this plateau the strength of the signal remains until almost 10 hours.

From previous experiments (Figures 35, 38, 37), I knew, that glucose starvation does not drastically decrease the viability within this timeframe, but also, that glucose starved cells proliferate less. However, for those HeLa cells I had not conducted this experiment in this exact loading buffer. This experiment unveiled, expectedly, that glucose starvation in this setup led to a reduction in proliferation (Figure 46 A) as seen by the stable total cell count over the whole experiment. Morphologically determined viability (Figure 46 B and C, dotted lines, left Y-axis) was not reduced within the timeframe (vertical dotted line in B) of the ATP measurements upon glucose starvation.

This correlation between the Ca^{2+} -coupled $[ATP]_{ER}$ and viability over time indicates the induction of compensatory mechanisms to maintain sufficient ATP mobilisation under conditions of energetic stress as a potential means of preserving cellular viability.

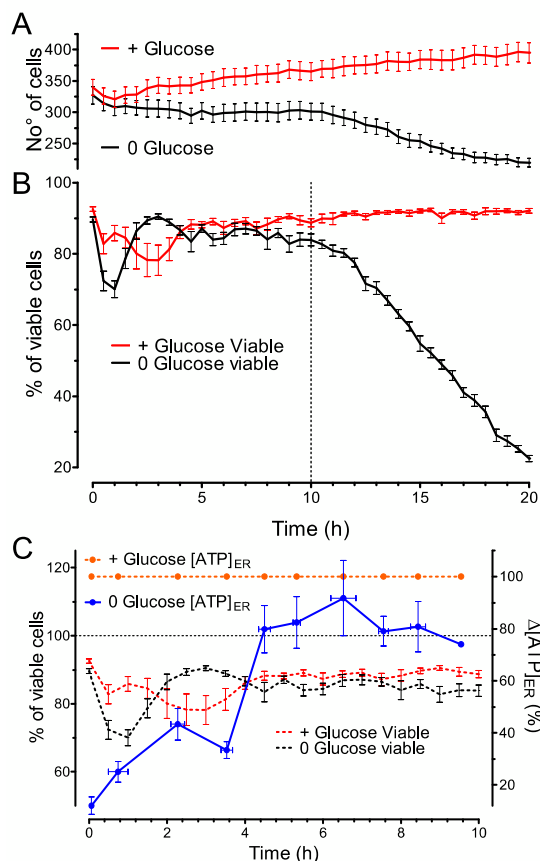


Figure (46): Glucose starvation influences $[\text{ATP}]_{\text{ER}}$ before an effect on viability observable. **A:** Total cell count of HeLa cells incubated with 10 mM glucose (+ glucose, red line) or without glucose (0 glucose, black line) estimated by Cell-IQ Analyser ($n=3$). **B:** Fraction of viable cells from A. **C:** Comparison of viability (left Y-axis, red and black dotted lines) from B for the first 10 hours (vertical dotted line in B) with Ca^{2+} -coupled $[\text{ATP}]_{\text{ER}}$ (right Y-axis) increase of glucose-starved HeLa cells. HeLa cells were measured after various starvation periods (straight blue line, 0.5 h - 9.5 h, $n=3-38$) in relation to the response of glucose-containing cells (orange dotted line). Within a couple of minutes, the signal decreased to about 20% of control, but recovered between 4 and 5 hours to almost control levels (80-90%). In the same period no change in viability could be observed.

5.3. Inhibition of AMP-activated Protein Kinase Reduces Cell Viability and the Ca^{2+} -Coupled $[\text{ATP}]_{\text{ER}}$ Increase

Cells, particularly cancer cells, have sophisticated mechanisms to cope with energy stress (Liang and Mills, 2013; Mathupala et al., 2010). One putative pathway by which cells respond to energetic deprivation is the AMP-activated protein kinase (AMPK), which regulates cellular ATP homeostasis among other processes.

To determine the role of AMPK on the proliferation (Figure 47 A) and viability (Figure 47 B and C) of the HeLa cells used in this project, I firstly attempted pharmacological activation of AMPK using 500 μM AICAR (green lines), inhibition by 10 μM Compound C (CC, red lines), or treatment with the solvent amount of DMSO (Control, black lines). Furthermore, glucose starvation (dotted lines) was applied on all three conditions, which primarily induces energetic stress, but also activates AMPK within about 4 minutes (Figure 48 A). Those experiments were performed in the normal DMSO cell culture medium. In line with the previously presented experiment (Figure 35 A), glucose starvation did not lead to an accumulation of cell death in control HeLa cells for about 20 hours (Figure 47 D). Subsequently, a steady decline in viability occurred, while the non-starved controls remained viable over the entire 40 hours of the experiment.

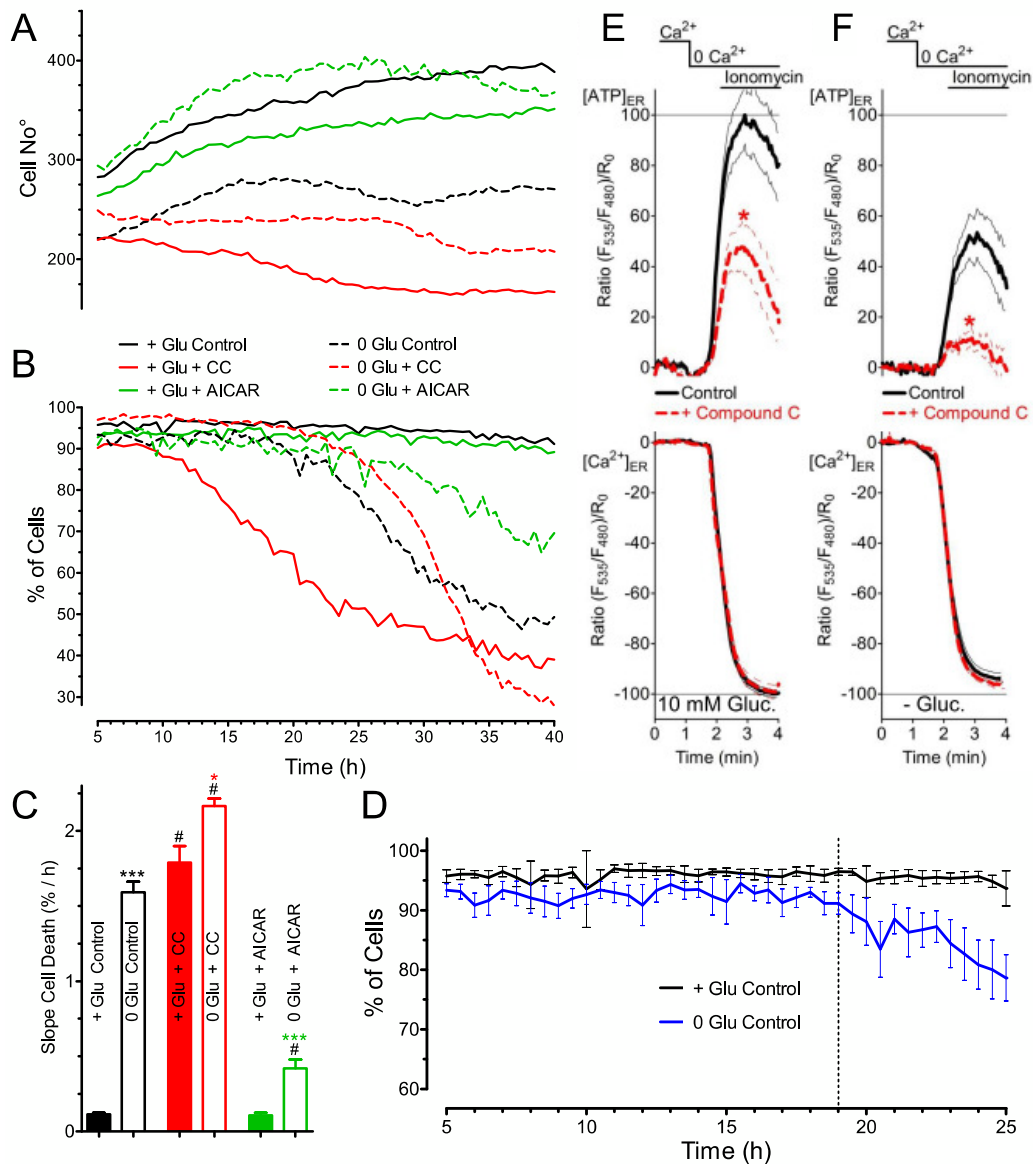


Figure (47): Pharmacological activation or inhibition of AMP-activated kinase (AMPK) by 500 μ M AICAR (green lines) or 10 μ M Compound C (CC, red lines), respectively, influences cell growth and viability compared to non-treated control HeLa cells (black lines). Cells were either incubated in loading buffer with 10 mM glucose (straight lines) or without glucose (dotted lines). **A:** Total number of cells during 40 hours ($n=3$). **B:** Fraction of viable cells from A. **C:** Slope of cell death as increase of dead cells per hour between 5 and 40 hours of the experiment. **D:** For about 19 hours (vertical dotted line) no obvious difference in viability of glucose-treated (black) or glucose-starved cells (blue) appeared. **E:** 2 μ M ionomycin-induced $[ATP]_{ER}$ ($n=31$, top panel) and $[Ca^{2+}]_{ER}$ signals ($n=14$, bottom panel) of HeLa cells treated with 10 μ M CC (red dotted line) compared to controls (black line) in presence of 10 mM glucose. **F:** as E, with glucose-starved cells ($n=23$ for $[ATP]_{ER}$, $n=13$ for $[Ca^{2+}]_{ER}$). * $p<0.05$ vs. Control, *** $p<0.0001$ vs. Control + glucose.

Since AMPK is a mediator of energy stress, I expected the AICAR-treated cells to tolerate glucose starvation better. Indeed, this was observed.

On the other hand, inhibition of AMPK by CC should theoretically lead to an decrease in viability in glucose-starved cells, those cells with glucose present should not be hampered.

	Glucose	Treatment	Cell Death Slope
1		Control	0.1 % / h
2	5.5 mM	Compound C	1.8 % / h
3		AICAR	0.1 % / h
4		Control	1.6 % / h
5	starvation	Compound C	2.2 % / h
6		AICAR	0.4 % / h

Tab. (6): Conditions used in the experiment presented in Figures 47. The cell death slopes were calculated from between 5 and 40 hours of the experiment of the curves in Figure 47 A, B and presented in C ($n=3$).

However, the opposite was the case. HeLa cells with glucose present started to die already after about 12 hours, while those incubated without glucose even started to accumulate cell death sparsely later than control cells at around 23 hours. But once cell death was ignited in those cells, the final viability reached the lowest level of all conditions, precised in the slope of cell death appearance between 5 and 40 hours of the experiment (entire presented period, Figure 47 C, Table 6). This shows, that the use of pharmacological tools

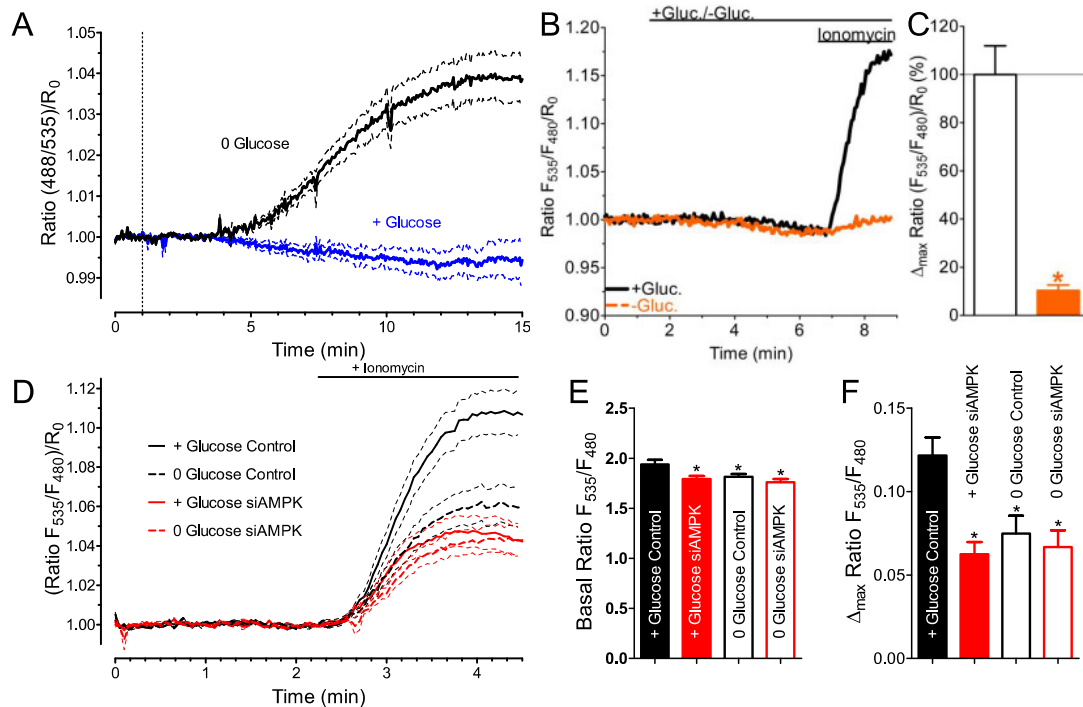


Figure (48): **A:** HeLa cells transfected with AMPK activity reporter (AMPKAR) were pre-incubated in glucose-containing loading buffer. After one minute of imaging (vertical dotted line), cells were either kept in glucose containing buffer (blue, $n=19$) or glucose-free buffer (black, $n=29$). After approximately 3 minutes, glucose starvation leads to an activation of AMPK. **B:** 2 μ M ionomycin-induced $[ATP]_{ER}$ signals of controls (+Gluc, black, $n=13$) or 4 minutes glucose starved HeLa cells (-Gluc, orange, $n=9$). **C:** Maximal response from B. **D:** HeLa cells were transfected with siRNA against AMPK (siAMPK, red) or scrambled siRNA (Control, black) and ERAT4.01. Prior to and during experiments, cells were either incubated in glucose-free buffers (0 Glucose, dotted lines) or presence of 10 mM glucose (+ Glucose, straight lines). 2 μ M ionomycin-induced $[ATP]_{ER}$ signal is shown ($n=25-31$). **E:** Basal $[ATP]_{ER}$ content from D. **F:** Maximal response from D. * $p < 0.05$ vs. Control or +Gluc.

should be addressed with caution, since unspecific bystander effects of those compounds can never be outruled and have already been proposed for CC (Emerling et al., 2007; Vucicevic et al., 2011).

The next step nevertheless was to measure the Ca^{2+} -coupled $[\text{ATP}]_{\text{ER}}$ increase in cells with CC-mediated AMPK inhibition. We found an CC-mediated diminishment of the Ca^{2+} -coupled $[\text{ATP}]_{\text{ER}}$ increase both in presence (Figure 47 E) and absence (Figure 47 F) of 10 mM glucose in the loading buffer (upper panels). Under both conditions, the Ca^{2+} release was not affected by CC.

However, as mentioned, the use of CC to specifically inhibit AMPK is debatable. We thus confirmed those results in cells with a transient siRNA-mediated AMPK knockdown (Figure 48 D and F). We again found, that glucose starvation leads to a reduction in the strength of the Ca^{2+} -coupled $[\text{ATP}]_{\text{ER}}$ increase. Further we confirmed the CC experiment to some extent and found, that AMPK knockdown (black lines and bars) significantly reduces the Ca^{2+} -coupled $[\text{ATP}]_{\text{ER}}$ increase compared to controls (black lines and bars). However, under AMPK knockdown condition, glucose starvation did not further affect the Ca^{2+} -coupled $[\text{ATP}]_{\text{ER}}$ increase. This indicates that AMPK is a crucial mediator of the Ca^{2+} -coupled $[\text{ATP}]_{\text{ER}}$ increase, as its absence somehow mimics glucose starvation in respect to the $[\text{ATP}]_{\text{ER}}$. This is supported by the fact that basal $[\text{ATP}]_{\text{ER}}$ is significantly lower in glucose starved control cells than in both conditions with AMPK knockdown (Figure 48 F).

5.4. Serum Starvation makes HeLa Cells more Susceptible to the Ca^{2+} -Coupled $[\text{ATP}]_{\text{ER}}$ Increase

As the last experiment of my diploma thesis I present an experiment, in which I correlated incubation in FCS containing cell culture medium or serum-free loading buffer with $[\text{ATP}]_{\text{ER}}$ and $[\text{Ca}^{2+}]_{\text{ER}}$ signals upon treatment with ionomycin (Figure 49). Of note, FCS presence or absence was not the only difference in both media, e.g. the cell culture medium is pH buffered by bicarbonate, while the loading buffer is pH buffered by HEPES (Figure 12).

Prior to the intracellular measurements, cells were either pre-incubated in loading buffer for up to 3 hours (vertical dotted line in Figure 49 A) or directly taken from the cell culture medium. Through this experiment, I unveiled, that the cells measured without pre-incubation in a serum-free buffer did not show a clear Ca^{2+} -coupled $[\text{ATP}]_{\text{ER}}$ increase (Figure 49 B), while the respective $[\text{Ca}^{2+}]_{\text{ER}}$ signals remained unaffected (Figure 49 C). Basal $[\text{ATP}]_{\text{ER}}$ (Figure 49 D) and $[\text{Ca}^{2+}]_{\text{ER}}$ (Figure 49 E) were not influenced.

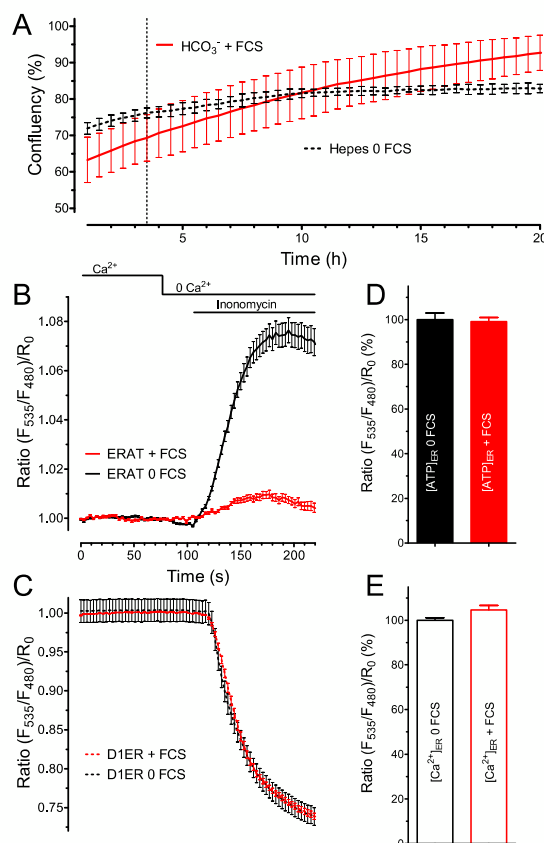


Figure (49): Pre-incubation in bicarbonate buffered medium containing 10% FCS (red straight lines or bars) or HEPES buffered medium without FCS (dotted black line) influences **A**: Cell proliferation determined by confluency analysis (also see Figure 12, $n=3$), **B**: 2 μM ionomycin-induced $[\text{ATP}]_{\text{ER}}$ increase ($n=6$, almost abolished in FCS presence), but not **C**: 2 μM ionomycin-induced $[\text{Ca}^{2+}]_{\text{ER}}$ signal ($n=3$). **D**: Basal $[\text{ATP}]_{\text{ER}}$ content in relation to 0 FCS. **E**: Basal $[\text{Ca}^{2+}]_{\text{ER}}$ content in relation to 0 FCS.

IV. Discussion

In the first part of the results I presented the Establishment of Life-Cell Imaging Assays, accompanied with a short literature research about available assays to determine viability, proliferation, and migration of cell populations. Intrinsically, this already includes some discussion, which is not explicitly labeled as such.

However, the high temporal resolution of long-term live-cell imaging compared to endpoint assays, the differences between determination of proliferation by means of confluency or cell number measurement, and the superiority of the cell exclusion zone insert assay over the scratch assay to elaborate cell migration are discussed more accurately here:

1. Long-Term Live-Cell Imaging Shows the Kinetics of Assays

The ability to perform viability, proliferation, and migration assays on microscopes over a period of hours or days can effectively increase the gained information of an experiment. First of all, the development of the observed cell populations can be viewed in real time, giving information about the kinetics of a process. To the contrary, in a classical end-point assay, e.g. an MTT assay (Mosmann, 1983) or a Boyden chamber assay (Boyden, 1962), a sample is determined at a fixed timepoint. Thus, a lot of presumably valuable data is missed, like the kinetic pattern which led to a given result, or the further development.

With live-cell imaging, I was able to detect the time point when starved cells begin to accumulate cell death. E.g. I found that the viability of glucose-starved HeLa cells begins to decrease after about 4 hours in experimental buffer (Figure 37 B), after 10 hours in loading buffer (Figure 46 B), and after about 29 hours in culture medium (Figure 35 A). In an MTT assay only one instance can be acquired, the kinetic information is lost.

Still, the determined viability of both morphological image series and MTT assay was comparable (Figure 39), though not identical. The final viability of control or MCU KD HeLa cells which were treated with C2-Ceramide to induce apoptosis was lower in the morphology analysis (12.1% and 21.0%) than in the MTT assay (48.6% and 37.3%) after 20 hours. This difference in the percentage viability of cell death-induced cells compared to non death-induced cells is likely due to the different ways of calculating viability. The MTT assay gives information about the metabolic activity. On the other hand, a cell morphologically recognized as dead might still remain some metabolic activity, which is undeterminable by image analysis.

Additionally, the MCU KD cells were significantly more viable if determined morphologically, which was not detected in the MTT assay. However, considering the stable viability of both cell groups between 12 and 20 hours, this difference in the final viability was likely

due to the recognition limitation of the morphology analysis. Therefore I calculated the slope of viability at the time of maximal cell death occurrence (between 3 and 6 hours) to compare both conditions. This unveiled no significant difference, in line with the MTT assay.

Another advantage is, that it is possible to observe the cells during the entire experiment and to review the acquired images afterwards. This turned out to be helpful in the analysis of Figure 35 and 36. In cases of both HeLa and EA.hy926 cells it appeared that three conditions remained the same viability over the whole experiment (+Glucose+FCS, +Glucose-FCS, and +Galactose-FCS). However, when I accounted the total cell count, I found that only the +Glucose+FCS (straight red line) treated cells were proliferating, while the other conditions induced a kind of growth arrest.

Another advantage is the flexibility of a long-term live-cell imaging assay, without hampering the prime goal of the experiment. In Figure 31, I found, that serum-starved HeLa cells do not change their proliferation rate for about 12 hours. Subsequently the starved cells entered a growth arrest state, but remained viable. My original plan was to stop this experiment after two days. Because nobody needed the system at this day, I decided to continue the image acquisition, in order to determine how long HeLa cells survive serum starvation. After 94 hours, the cells were still viable in a dormant state. At this point, a medium exchange would be necessary if the cells were in regular cell culture conditions. I decided to re-add FCS containing medium, to determine, if the cells could be stimulated to proliferate again, which was indeed observed (D and G).

On the other hand, long-term live-cell imaging also has some disadvantages compared to endpoint assays. These belong primarily to the rubric of resources, as the amount of gigabytes acquired during my diploma thesis indicates. Also the time required for analysis, even with the semi-automatic morphology analysis of the Cell-IQ Analyser, is substantially higher.

Nonetheless, the possible gain in information and unforeseeable results legitimate the use of long-term live-cell imaging assays, if such a system is available and one is willing to employ it.

2. Proliferation Determined by Cell Count Analysis is more Sensitive than Confluency Analysis

I compared two different analysis processes to determine the proliferation rate of cell populations, plotting either the confluency or the total cell count over time. Both values were rendered by Cell-IQ Analyser. While the cell counting (including cell type differentiation) (Toimela et al., 2008) is a specific strength of this software, cell confluency could also be determined by other softwares (Topman et al., 2011) (not tested).

The cell confluency determination does not differentiate between cell enlargement and increase in cell number, while the cell number solely considers the latter. Confluency measurement is limited to 100%, while those fully crowded cell populations might still proliferate by means of division. Accordingly, both estimations should result in a similar, but not necessarily identical proliferation rate. This is exemplified in Figure 31, where I determined the proliferation of HeLa upon serum starvation including a rescue attempt after 12 hours.

Confluency measurement determined, that both serum-containing controls and the rescue condition were proliferating significantly faster than the serum-starved controls after serum readdition, but no difference when compared against each other (Figure 31 B). To the contrary, cell number analysis showed, that the rescue condition also showed a significantly higher cell number increase than the +FCS controls, without any change compared to the FCS-free controls (Figure 31 F). This might be a consequence of a higher fraction of dividing cells, which cover less area of an image, but nonetheless count as a cell.

Another difference which attracted my attention was, that the curve of confluency (Figure 31 A) was rather steep during the first half of the experiment, while during the second half the curve flattened, especially when coming close to 90% confluency. In this extent, the cell number curve appeared as the opposite, being flat at first and increasingly rising later. This is expected, as cancer cells in ideal growth conditions should grow exponentially (Finlay et al., 1984).

As mentioned earlier, in a cell proliferation assay, the cells should ideally have an initial confluency of about 50%. At such a density, both proliferation analysis methods should render similar results, what I found for most of my proliferation experiments.

The major drawback of the cell number analysis was the resources. As explained in the establishment of morphology analysis section, the cell counting requires slight adjustments for each image series. Although it might be expected that at least the complex differentiation between different types of cells can be ignored for purely counting the cells, this is not the case. In most samples, cellular debris or other trash is recognized as an object, hence at least a subclass for trash needs to be included. Apart from a more time intense sample library creation, the time to compute the cell counting can also be multiplied compared to the simple confluency determination. Hence, the confluency analysis of cell proliferation is suited for high-throughput experiments, a property that can be accounted for the cell number analysis only with severe restrictions.

Accordingly, for the later experiments, I relied solely on the confluency analysis (Figure 40 and 43).

3. Analysis of Cell Exclusion Insert Assays is more Straightforward than of Scratch Assays

I compared two different cell migration assays, the conventional scratch wound-healing assay and a cell exclusion assay using a cell culture insert from ibidi®. The scratch assay is a popular method to determine migration (Lampugnani, 1999; Liang et al., 2007; Cory, 2011), while cell exclusion assays were relatively recently developed.

A clear disadvantage of scratching a wound by hand is that the gap size of different wells will always vary. Several attempts were introduced to gain reproducibly even gap sizes, e.g. by standardized scratches (Yarrow et al., 2004), electrical wounding (Keese et al., 2004), or inserts. As these silicon-based inserts (Figure 10) are machine-made, the gap size should expectedly be 500 μm wide. Of note, I observed differently wide gap sizes even when using inserts (Figures 23, 32, 33). Nonetheless, the variation was clearly less substantial than in case of scratch assays.

Another drawback of the scratch assay is the fact, that the cells are wounded and ultimately killed by the gap creation. This leads first of all to a high amount of cellular debris on the gap, which can be reduced but not abolished by washing the samples twice. Even cells grown in the inserts need to be washed after removal, as that remained on top of other cells, might reattach upon insert removal in the middle of the gap. This was almost abolished by washing the cells twice immediately after insert removal. Secondly, the wounded and killed cells release their interior into the medium, which will definitely influence cells in the vicinity, potentially promoting or diminishing cell migration. Arguably, this is a better model of wound-healing, as dead and altered cells would be expected in a wound. Nonetheless, those assays anyways do not reflect the conditions of an *in vivo* wound (Shaw and Martin, 2009), thus I suspect that the cell exclusion insert assay is better to determine solely the migration of cells. Thirdly, the process of scratching will inevitably damage the substrate and culture dishes, potentially inducing artifacts (Kam et al., 2008).

Another important factor is the analysis. As mentioned, cellular debris is unavoidable for both assays, it plays only a minor role in the cell exclusion insert assay. On the other hand, I could never completely remove debris in a scratch assay. This interfered substantially with the ability of the Cell-IQ Analyser to differentiate gap from cells. I did not successfully and satisfactorily analyse a scratch assay automatically, every presented graph was analysed manually. On the other hand, the cell exclusion insert assay was ideally suited for automatic analysis. With only few exceptions, I was able to analyse these assays in a short amount of time with the same settings even in cases of 24 conditions. The time required to compute the images was also very short compared to the differential cell counting processes. Those features make the cell exclusion insert assay feasible for high-

throughput analysis, which could not be performed with the scratch assay.

I already discussed the percentage bias (Results, 1.8.5). Briefly, if cell migration is shown as percentage of initial wound width, then those cells with a shorter gap seemingly migrate faster than those with a wider gap (Figures 23). Thus, I showed the decline in gap width over time and calculated the slope for a time before the cells closed the gap.

References

- Abercrombie, M. and Heaysman, J. E. (1953). Observations on the social behaviour of cells in tissue culture: I. Speed of movement of chick heart fibroblasts in relation to their mutual contacts. *Experimental cell research* 5, 111–131.
- Andrews, D. L. and Bradshaw, D. S. (2004). Virtual photons, dipole fields and energy transfer: a quantum electrodynamical approach. *European journal of physics* 25, 845.
- Atkins, G., Jain, M. and Hamik, A. (2011). Endothelial Differentiation Molecular Mechanisms of Specification and Heterogeneity. *Arterioscler., Thromb., Vasc. Biol.* 31, 1476–1484.
- Ayas, S., Cinar, G., Ozkan, A. D., Soran, Z., Ekiz, O., Kocaay, D., Tomak, A., Toren, P., Kaya, Y., Tunc, I. et al. (2013). Label-Free Nanometer-Resolution Imaging of Biological Architectures through Surface Enhanced Raman Scattering. *Scientific reports* 3, 2624.
- Baker, M. (2010). Cellular imaging: Taking a long, hard look. *Nature* 466, 1137–1140.
- Baskić, D., Popović, S., Ristić, P. and Arsenijević, N. N. (2006). Analysis of cycloheximide-induced apoptosis in human leukocytes: fluorescence microscopy using annexin V/propidium iodide versus acridin orange/ethidium bromide. *Cell biology international* 30, 924–932.
- Bast, R. C., Kufe, D. W., Pollock, R. E., Weichselbaum, R. R., Holland, J. F. and Frei, E. (2000). Holland-frei cancer medicine. BC Decker 5.
- Baughman, J., Perocchi, F., Girgis, H., Plovanich, M., Belcher-Timme, C., Sancak, Y., Bao, X., Strittmatter, L., Goldberger, O., Bogorad, R. et al. (2011). Integrative genomics identifies MCU as an essential component of the mitochondrial calcium uniporter. *Nature* 476, 341–345.
- Beemster, G. T., De Vusser, K., De Tavernier, E., De Bock, K. and Inzé, D. (2002). Variation in growth rate between Arabidopsis ecotypes is correlated with cell division and A-type cyclin-dependent kinase activity. *Plant Physiology* 129, 854–864.
- Benninger, R. K. and Piston, D. W. (2013). Two Photon Excitation Microscopy for the Study of Living Cells and Tissues. *Current Protocols in Cell Biology* 4, 4–11.
- Berridge, M. V., Herst, P. M. and Tan, A. S. (2005). Tetrazolium dyes as tools in cell biology: new insights into their cellular reduction. *Biotechnology annual review* 11, 127–152.

- Berridge, M. V. and Tan, A. S. (1993). Characterization of the cellular reduction of 3-(4, 5-dimethylthiazol-2-yl)-2, 5-diphenyltetrazolium bromide (MTT): subcellular localization, substrate dependence, and involvement of mitochondrial electron transport in MTT reduction. *Archives of Biochemistry and Biophysics* 303, 474–482.
- Betzig, E., Patterson, G. H., Sougrat, R., Lindwasser, O. W., Olenych, S., Bonifacino, J. S., Davidson, M. W., Lippincott-Schwartz, J. and Hess, H. F. (2006). Imaging intracellular fluorescent proteins at nanometer resolution. *Science* 313, 1642–1645.
- Blakytyn, R. and Jude, E. (2006). The molecular biology of chronic wounds and delayed healing in diabetes. *Diabetic Medicine* 23, 594–608.
- Bouïs, D., Hospers, G., Meijer, C., Molema, G. and Mulder, N. (2001). Endothelium in vitro: a review of human vascular endothelial cell lines for blood vessel-related research. *Angiogenesis* 4, 91–102.
- Boyden, S. (1962). The chemotactic effect of mixtures of antibody and antigen on polymorphonuclear leucocytes. *The Journal of experimental medicine* 115, 453–466.
- Bridges, E. and Harris, A. (2011). The angiogenic process as a therapeutic target in cancer. *Biochem. Pharmacol.* 81, 1183–1191.
- Caarls, W., Rieger, B., De Vries, A., ARNDT-JOVIN, D. and Jovin, T. (2011). Minimizing light exposure with the programmable array microscope. *Journal of microscopy* 241, 101–110.
- Canonica, P. G. and Bird, J. W. (1969). The use of acridine orange as a lysosomal marker in rat skeletal muscle. *The Journal of cell biology* 43, 367–371.
- Capani, F., Deerinck, T. J., Ellisman, M. H., Bushong, E., Bobik, M. and Martone, M. E. (2001). Phalloidin-Eosin Followed by Photo-oxidation A Novel Method for Localizing F-Actin at the Light and Electron Microscopic Levels. *Journal of Histochemistry & Cytochemistry* 49, 1351–1361.
- Carmeliet, P. and Jain, R. (2011). Molecular mechanisms and clinical applications of angiogenesis. *Nature* 473, 298–307.
- Castellot, J. J., Addonizio, M. L., Rosenberg, R. and Karnovsky, M. J. (1981). Cultured endothelial cells produce heparinlike inhibitor of smooth muscle cell growth. *The Journal of cell biology* 90, 372–379.
- Cavallaro, U., Tenan, M., Castelli, V., Perilli, A., Maggiano, N., Van Meir, E. G., Montesano, R., Soria, M. R. and Pepper, M. S. (2001). Response of bovine endothelial cells

- to FGF-2 and VEGF is dependent on their site of origin: Relevance to the regulation of angiogenesis. *Journal of cellular biochemistry* 82, 619–633.
- Chalfie, M., Tu, Y., Euskirchen, G., Ward, W. W. and Prasher, D. C. (1994). Green fluorescent protein as a marker for gene expression. *Science* 263, 802–805.
- Chaubey, S., Ridley, A. J. and Wells, C. M. (2011). Using the Dunn Chemotaxis Chamber to Analyze Primary Cell Migration in Real Time. In *Cell Migration* pp. 41–51. Springer.
- Chen, F. W. et al. (1996). Quantitation of DNA fragmentation in apoptosis. *Nucleic acids research* 24, 992–993.
- chipman technologies (2004). CELL-IQ ANALYSER MANUAL. chipman technologies.
- Chudakov, D. M., Lukyanov, S. and Lukyanov, K. A. (2005). Fluorescent proteins as a toolkit for *in vivo* imaging. *Trends in biotechnology* 23, 605–613.
- Comandon, J. (1909). Cinematographie, a l ultramicroscope des microbes vivantes et des particules mobiles. *Comptes rendus hebdomadaires des séances de l Académie des sciences* 149, 938–940.
- Cooper, J. A. (1987). Effects of cytochalasin and phalloidin on actin. *The Journal of Cell Biology* 105, 1473–1478.
- Cory, G. (2011). Scratch-wound assay. In *Cell Migration* pp. 25–30. Springer.
- Dahmer, S. and Scott, E. (2010). Health effects of hawthorn. *American family physician* 81, 465.
- Davidson, S. M. and Duchen, M. R. (2012). Imaging mitochondrial calcium signalling with fluorescent probes and single or two photon confocal microscopy. In *Mitochondrial Bioenergetics* pp. 219–234. Springer.
- De Stefani, D., Raffaello, A., Teardo, E., Szabò, I. and Rizzuto, R. (2011). A forty-kilodalton protein of the inner membrane is the mitochondrial calcium uniporter. *Nature* 476, 336–340.
- Deak, A. T., Groschner, L. N., Alam, M. R., Seles, E., Bondarenko, A. I., Graier, W. F. and Malli, R. (2013). The endocannabinoid N-arachidonoyl glycine (NAGly) inhibits store-operated Ca²⁺ entry by abrogating STIM1/Orai1 interaction. *Journal of cell science* 126, 879.

- Degrassi, F. and Tanzarella, C. (1988). Immunofluorescent staining of kinetochores in micronuclei: a new assay for the detection of aneuploidy. *Mutation Research/Environmental Mutagenesis and Related Subjects* 203, 339–345.
- Distler, J., Hirth, A., Kurowska-Stolarska, M., Gay, R., Gay, S. and Distler, O. (2003). Angiogenic and angiostatic factors in the molecular control of angiogenesis. *Q. J. Nucl. Med.* 47, 149–161.
- Dulbecco, R. and Freeman, G. (1959). Plaque production by the polyoma virus. *Virology* 8, 396–7.
- Eagle, H. (1959). Amino acid metabolism in mammalian cell cultures. *Science (New York, NY)* 130, 432.
- Edgell, C., McDonald, C. and Graham, J. (1983). Permanent cell line expressing human factor VIII-related antigen established by hybridization. *Proc. Natl. Acad. Sci.* 80, 3734–3737.
- Edinger, A. L. and Thompson, C. B. (2004). Death by design: apoptosis, necrosis and autophagy. *Current opinion in cell biology* 16, 663–669.
- Egner, A., Andresen, V. and Hell, S. (2002). Comparison of the axial resolution of practical Nipkow-disk confocal fluorescence microscopy with that of multifocal multiphoton microscopy: theory and experiment. *Journal of microscopy* 206, 24–32.
- Ehrlich, P. (1877). Beiträge zur Kenntniss der Anilinfärbungen und ihrer Verwendung in der mikroskopischen Technik. *Archiv für mikroskopische Anatomie* 13, 263–277.
- Emerling, B. M., Viollet, B., Tormos, K. V. and Chandel, N. S. (2007). Compound C inhibits hypoxic activation of HIF-1 independent of AMPK. *FEBS letters* 581, 5727–5731.
- Enari, M., Sakahira, H., Yokoyama, H., Okawa, K., Iwamatsu, A. and Nagata, S. (1998). A caspase-activated DNase that degrades DNA during apoptosis, and its inhibitor ICAD. *Nature* 391, 43–50.
- Enesco, M. and Leblond, C. (1962). Increase in cell number as a factor in the growth of the organs and tissues of the young male rat. *Journal of Embryology and Experimental Morphology* 10, 530–562.
- Felgner, J., Kumar, R., Sridhar, C., Wheeler, C. J., Tsai, Y. J., Border, R., Ramsey, P., Martin, M. and Felgner, P. (1994). Enhanced gene delivery and mechanism studies with a novel series of cationic lipid formulations. *J. Biol. Chem.* 269, 2550–2561.

- Finlay, G. J., Baguley, B. C. and Wilson, W. R. (1984). A semiautomated microculture method for investigating growth inhibitory effects of cytotoxic compounds on exponentially growing carcinoma cells. *Analytical biochemistry* *139*, 272–277.
- Fishman, J., Ryan, G. and Karnovsky, M. (1975). Endothelial regeneration in the rat carotid artery and the significance of endothelial denudation in the pathogenesis of myointimal thickening. *Laboratory investigation; a journal of technical methods and pathology* *32*, 339–351.
- Folkman, J. (2002). Role of angiogenesis in tumor growth and metastasis. In *Seminars in oncology* vol. 29, pp. 15–18, Elsevier.
- Folkman, J. and Shing, Y. (1992). Angiogenesis. *J. Biol. Chem.* *267*, 10931–10934.
- Förster, T. (1948). Zwischenmolekulare energiewanderung und fluoreszenz. *Annalen der Physik* *437*, 55–75.
- Fougerat, A., Smirnova, N., Gayral, S., Malet, N., Hirsch, E., Wymann, M., Perret, B., Martinez, L., Douillon, M. and Laffargue, M. (2012). Key role of PI3K γ in monocyte chemotactic protein-1-mediated amplification of PDGF-induced aortic smooth muscle cell migration. *British journal of pharmacology* *166*, 1643–1653.
- Fraisl, P., Mazzone, M., Schmidt, T. and Carmeliet, P. (2009). Regulation of angiogenesis by oxygen and metabolism. *Dev. Cell* *16*, 167–179.
- Françon, M. (1964). Polarization interference microscopes. *Applied Optics* *3*, 1033–1036.
- Friedl, P. and Wolf, K. (2010). Plasticity of cell migration: a multiscale tuning model. *The Journal of cell biology* *188*, 11–19.
- Fritschy, J.-M. and Härtig, W. (2001). Immunofluorescence. *eLS online*, 10.1038/npg.els.0001174.
- Fürst, R., Bubik, M. F., Bihari, P., Mayer, B. A., Khandoga, A. G., Hoffmann, F., Rehberg, M., Krombach, F., Zahler, S. and Vollmar, A. M. (2008). Atrial natriuretic peptide protects against histamine-induced endothelial barrier dysfunction in vivo. *Molecular pharmacology* *74*, 1–8.
- Fürst, R., Zirrgiebel, U., Totzke, F., Zahler, S., Vollmar, A. M. and Koch, E. (2010). The Crataegus extract WS[®] 1442 inhibits balloon catheter-induced intimal hyperplasia in the rat carotid artery by directly influencing PDGFR- β . *Atherosclerosis* *211*, 409–417.

- Galluzzi, L., Vitale, I., Abrams, J., Alnemri, E., Baehrecke, E., Blagosklonny, M., Dawson, T., Dawson, V., El-Deiry, W., Fulda, S. et al. (2011). Molecular definitions of cell death subroutines: recommendations of the Nomenclature Committee on Cell Death 2012. *Cell Death & Differentiation* *19*, 107–120.
- Gavrieli, Y., Sherman, Y. and Ben-Sasson, S. A. (1992). Identification of programmed cell death in situ via specific labeling of nuclear DNA fragmentation. *The Journal of cell biology* *119*, 493–501.
- Gebäck, T., Schulz, M., Koumoutsakos, P. and Detmar, M. (2009). TScratch: a novel and simple software tool for automated analysis of monolayer wound healing assays. *Biotechniques* *46*, 265–74.
- Ghiran, I. C. (2011). Introduction to Fluorescence Microscopy. In *Light Microscopy* pp. 93–136. Springer.
- Graier, W. F., Frieden, M. and Malli, R. (2007). Mitochondria and Ca²⁺ signaling: old guests, new functions. *Pflügers Archiv-European Journal of Physiology* *455*, 375–396.
- Griffiths, A. J., Wessler, S. R., Carroll, S. B. and Doebley, J. (2010). *Introduction to Genetic Analysis (Loose Leaf)*. Macmillan Higher Education.
- Grotendorst, G. R., Soma, Y., Takehara, K. and Charette, M. (1989). EGF and TGF- α are potent chemoattractants for endothelial cells and EGF-like peptides are present at sites of tissue regeneration. *Journal of cellular physiology* *139*, 617–623.
- Grynkiewicz, G., Poenie, M. and Tsien, R. Y. (1985). A new generation of Ca²⁺ indicators with greatly improved fluorescence properties. *Journal of Biological Chemistry* *260*, 3440–3450.
- Gustafsson, M. G. (2005). Nonlinear structured illumination microscopy: wide-field fluorescence imaging with theoretically unlimited resolution. *Proc. Natl. Acad. Sci. U. S. A.* *102*, 13081–13086.
- Hardie, D. G., Salt, I. P. and Davies, S. P. (2000). Analysis of the Role of the AMP-Activated Protein Kinase in the Response to Cellular Stress. *Stress Response: Methods and Protocols* *99*, 63.
- Hatten, M. E. (2002). New directions in neuronal migration. *Science* *297*, 1660–1663.
- Hell, S. W. (2010). Far-field optical nanoscopy. In *Single Molecule Spectroscopy in Chemistry, Physics and Biology* pp. 365–398. Springer.

- Hell, S. W. and Wichmann, J. (1994). Breaking the diffraction resolution limit by stimulated emission: stimulated-emission-depletion fluorescence microscopy. *Optics letters* *19*, 780–782.
- Hoebe, R., Van Oven, C., Gadella, T. W., Dhonukshe, P., Van Noorden, C. and Manders, E. (2007). Controlled light-exposure microscopy reduces photobleaching and phototoxicity in fluorescence live-cell imaging. *Nature biotechnology* *25*, 249–253.
- Hoffman, R. (1977). The modulation contrast microscope: principles and performance. *Journal of microscopy* *110*, 205–222.
- Huang, H.-L., Hsing, H.-W., Lai, T.-C., Chen, Y.-W., Lee, T.-R., Chan, H.-T., Lyu, P.-C., Wu, C.-L., Lu, Y.-C., Lin, S.-T. et al. (2010). Research Trypsin-induced proteome alteration during cell subculture in mammalian cells. *Journal of biomedical science* *17*, 36.
- Imamura, H., Nhat, K. P. H., Togawa, H., Saito, K., Iino, R., Kato-Yamada, Y., Nagai, T. and Noji, H. (2009). Visualization of ATP levels inside single living cells with fluorescence resonance energy transfer-based genetically encoded indicators. *Proceedings of the National Academy of Sciences* *106*, 15651–15656.
- Inoue, A., Sawata, S. Y., Taira, K. and Wadhwa, R. (2007). Loss-of-function screening by randomized intracellular antibodies: Identification of hnRNP-K as a potential target for metastasis. *Proceedings of the National Academy of Sciences* *104*, 8983–8988.
- Jares-Erijman, E. A. and Jovin, T. M. (2003). FRET imaging. *Nature biotechnology* *21*, 1387–1395.
- Johnson-Buck, A., Nangreave, J., Kim, D.-N., Bathe, M., Yan, H. and Walter, N. G. (2013). Super-Resolution Fingerprinting Detects Chemical Reactions and Idiosyncrasies of Single DNA Pegboards. *Nano Lett.* *13*, 728–33.
- Kam, Y., Guess, C., Estrada, L., Weidow, B. and Quaranta, V. (2008). A novel circular invasion assay mimics in vivo invasive behavior of cancer cell lines and distinguishes single-cell motility in vitro. *BMC cancer* *8*, 198.
- Kapuscinski, J. (1995). DAPI: a DNA-specific fluorescent probe. *Biotechnic & Histochemistry* *70*, 220–233.
- Kaufmann, R., Müller, P., Hausmann, M. and Cremer, C. (2011). Imaging label-free intracellular structures by localisation microscopy. *Micron* *42*, 348–352.

- Keese, C. R., Wegener, J., Walker, S. R. and Giaever, I. (2004). Electrical wound-healing assay for cells in vitro. *Proceedings of the National Academy of Sciences of the United States of America* *101*, 1554–1559.
- Kerr, J. F., Wyllie, A. H. and Currie, A. R. (1972). Apoptosis: a basic biological phenomenon with wide-ranging implications in tissue kinetics. *British journal of cancer* *26*, 239.
- Khan, M. J., Alam, M. R., Waldeck Weiermair, M., Karsten, F., Groschner, L., Riederer, M., Hallström, S., Rockenfeller, P., Konya, V., Heinemann, A. et al. (2012). Inhibition of autophagy rescues palmitic acid induced necroptosis of endothelial cells. *J. Biol. Chem.* *287*, 21110–21120.
- Kittler, R., Pelletier, L., Heninger, A.-K., Slabicki, M., Theis, M., Mirosław, L., Poser, I., Lawo, S., Grabner, H., Kozak, K. et al. (2007). Genome-scale RNAi profiling of cell division in human tissue culture cells. *Nature cell biology* *9*, 1401–1412.
- Kramer, N., Walzl, A., Unger, C., Rosner, M., Krupitza, G., Hengstschläger, M. and Dolznig, H. (2012). In vitro cell migration and invasion assays. *Mutation Research* *752*, 10–24.
- Kuhlmann, I. (1995). The prophylactic use of antibiotics in cell culture. *Cytotechnology* *19*, 95–105.
- Lampugnani, M. G. (1999). Cell migration into a wounded area in vitro. In *Adhesion Protein Protocols* pp. 177–182. Springer.
- Landecker, H. (2009). Seeing things: from microcinematography to live cell imaging. *Nature Methods* *6*, 707–709.
- Latt, S. A., Stetten, G., Juergens, L. A., Willard, H. F. and Scher, C. D. (1975). Recent developments in the detection of deoxyribonucleic acid synthesis by 33258 Hoechst fluorescence. *Journal of Histochemistry & Cytochemistry* *23*, 493–505.
- Lecoeur, H. (2002). Nuclear apoptosis detection by flow cytometry: influence of endogenous endonucleases. *Experimental cell research* *277*, 1–14.
- Lecoeur, H., de Oliveira-Pinto, L. M. and Gougeon, M.-L. (2002). Multiparametric flow cytometric analysis of biochemical and functional events associated with apoptosis and oncosis using the 7-aminoactinomycin D assay. *Journal of immunological methods* *265*, 81–96.
- Lewis, W. H. and Gregory, P. (1929). Cinematographs of living developing rabbit-eggs. *Science* *69*, 226–229.

- Lewis, W. H. and Lewis, M. R. (1939). Normal and abnormal white blood cells in tissue cultures (<http://www.youtube.com/watch?v=ezkZGAlo8RM>).
- Lewis, W. H. and Webster, L. T. (1921). Migration of lymphocytes in plasma cultures of human lymph nodes. *The Journal of experimental medicine* *33*, 261.
- Liang, C.-C., Park, A. Y. and Guan, J.-L. (2007). In vitro scratch assay: a convenient and inexpensive method for analysis of cell migration in vitro. *Nature protocols* *2*, 329–333.
- Liang, J. and Mills, G. B. (2013). AMPK: A Contextual Oncogene or Tumor Suppressor? *Cancer research* *73*, 2929–2935.
- Lindner, B. and Seydel, U. (1983). Mass spectrometric analysis of drug-induced changes in Na⁺ and K⁺ contents of single bacterial cells. *Journal of general microbiology* *129*, 51–55.
- Lukyanov, K. A. and Belousov, V. V. (2013). Genetically encoded fluorescent redox sensors. *Biochimica et Biophysica Acta (BBA)-General Subjects* *1840*, 745–756.
- Luster, A. D., Alon, R. and von Andrian, U. H. (2005). Immune cell migration in inflammation: present and future therapeutic targets. *Nature immunology* *6*, 1182–1190.
- Lyons, A. B. and Parish, C. R. (1994). Determination of lymphocyte division by flow cytometry. *Journal of immunological methods* *171*, 131–137.
- Mallilankaraman, K., Doonan, P., Cárdenas, C., Chandramoorthy, H. C., Müller, M., Miller, R., Hoffman, N. E., Gandhirajan, R. K., Molgó, J., Birnbaum, M. J. et al. (2012). MICU1 Is an Essential Gatekeeper for MCU-Mediated Mitochondrial Ca²⁺ Uptake that Regulates Cell Survival. *Cell* *151*, 630–644.
- Marrison, J., Rätty, L., Marriott, P. and O’Toole, P. (2013). Ptychography—a label free, high-contrast imaging technique for live cells using quantitative phase information. *Scientific reports* *3*.
- Mathupala, S. P., Ko, Y. H. and Pedersen, P. L. (2010). The pivotal roles of mitochondria in cancer: Warburg and beyond and encouraging prospects for effective therapies. *Biochimica et Biophysica Acta (BBA)-Bioenergetics* *1797*, 1225–1230.
- Minsky, M. (1988). Memoir on inventing the confocal scanning microscope. *Scanning* *10*, 128–138.

- Miyawaki, A., Llopis, J., Heim, R., McCaffery, J. M., Adams, J. A., Ikura, M. and Tsien, R. Y. (1997). Fluorescent indicators for Ca^{2+} ; based on green fluorescent proteins and calmodulin. *Nature* *388*, 882–887.
- Moore, G., Gerner, R. and Franklin, H. (1967). Culture of normal human leukocytes. *J.A.M.A* *199*, 519–24.
- Mosmann, T. (1983). Rapid colorimetric assay for cellular growth and survival: application to proliferation and cytotoxicity assays. *Journal of immunological methods* *65*, 55–63.
- Nahman Jr, N., Leonhart, K., Cosio, F. and Hebert, C. (1992). Effects of high glucose on cellular proliferation and fibronectin production by cultured human mesangial cells. *Kidney international* *41*, 396.
- Nakano, M., Imamura, H., Nagai, T. and Noji, H. (2011). Ca^{2+} regulation of mitochondrial ATP synthesis visualized at the single cell level. *ACS chemical biology* *6*, 709–715.
- Nguyen, D. X., Bos, P. D. and Massagué, J. (2009). Metastasis: from dissemination to organ-specific colonization. *Nature Reviews Cancer* *9*, 274–284.
- Omelchenko, T. and Hall, A. (2012). Myosin-IXA regulates collective epithelial cell migration by targeting RhoGAP activity to cell-cell junctions. *Current biology* *22*, 278–288.
- Ormö, M., Cubitt, A. B., Kallio, K., Gross, L. A., Tsien, R. Y. and Remington, S. J. (1996). Crystal structure of the *Aequorea victoria* green fluorescent protein. *Science* *273*, 1392–1395.
- Paddock, S. W. (1999). Confocal laser scanning microscopy. *Biotechniques* *27*, 992–1007.
- Page, K. and Lange, Y. (1997). Cell adhesion to fibronectin regulates membrane lipid biosynthesis through AMP-activated protein kinase. *Journal of Biological Chemistry* *272*, 19339–19342.
- Palmer, A. E., Jin, C., Reed, J. C. and Tsien, R. Y. (2004). Bcl-2-mediated alterations in endoplasmic reticulum Ca^{2+} analyzed with an improved genetically encoded fluorescent sensor. *Proceedings of the National Academy of Sciences of the United States of America* *101*, 17404–17409.
- Palmer, A. E., Qin, Y., Park, J. G. and McCombs, J. E. (2011). Design and application of genetically encoded biosensors. *Trends in biotechnology* *29*, 144–152.

- Palmer, A. E. and Tsien, R. Y. (2006). Measuring calcium signaling using genetically targetable fluorescent indicators. *Nature protocols* 1, 1057–1065.
- Pandya, N., Dhalla, N. and Santani, D. (2006). Angiogenesis—a new target for future therapy. *Vascular pharmacology* 44, 265–274.
- Patterson, G. H. and Piston, D. W. (2000). Photobleaching in two-photon excitation microscopy. *Biophysical journal* 78, 2159–2162.
- Pawley, J. B. (1995). *Handbook of biological confocal microscopy*. Springer.
- Perocchi, F., Gohil, V., Girgis, H., Bao, X., McCombs, J., Palmer, A. and Mootha, V. (2010). MICU1 encodes a mitochondrial EF hand protein required for Ca²⁺ uptake. *Nature* 467, 291–296.
- Pfleger, K. D. and Eidne, K. A. (2006). Illuminating insights into protein-protein interactions using bioluminescence resonance energy transfer (BRET). *Nature Methods* 3, 165–174.
- Pisanti, S., Borselli, C., Oliviero, O., Laezza, C., Gazzero, P. and Bifulco, M. (2007). Antiangiogenic activity of the endocannabinoid anandamide: Correlation to its tumor-suppressor efficacy. *J. Cell. Physiol.* 211, 495–503.
- Proskuryakov, S. Y., Konoplyannikov, A. G. and Gabai, V. L. (2003). Necrosis: a specific form of programmed cell death? *Experimental cell research* 283, 1–16.
- Raffaello, A., De Stefani, D. and Rizzuto, R. (2012). The mitochondrial Ca²⁺ uniporter. *Cell calcium* 52, 16–21.
- Rao, S., Chun, C., Fan, J., Kofron, J. M., Yang, M. B., Hegde, R. S., Ferrara, N., Copenhagen, D. R. and Lang, R. A. (2013). A direct and melanopsin-dependent fetal light response regulates mouse eye development. *Nature* 494, 243–6.
- Ries, J. (1909). Kinematographie der Befruchtung und Zellteilung. *Archiv für mikroskopische Anatomie* 74, 1–31.
- Riss, T. L., Sittampalam, G. S., Gal-Edd, N., Arkin, M., Auld, D., Austin, C., Bejcek, B., Glicksman, M., Inglese, J., Lemmon, V., Li, Z. et al. (2013). *Cell Viability Assays*. online.
- Rosenberger, H. (1929). Micro-Cinematography in Medical Research. *Journal of Dental Research* 9, 343–352.
- Rust, M. J., Bates, M. and Zhuang, X. (2006). Sub diffraction limit imaging by stochastic optical reconstruction microscopy. *Nature methods* 3, 793–796.

- Sawano, A., Hama, H., Saito, N. and Miyawaki, A. (2002). Multicolor Imaging of Ca^{2+} and Protein Kinase C Signals Using Novel Epifluorescence Microscopy. *Biophysical journal* 82, 1076–1085.
- Schnittger, A., Schöbinger, U., Bouyer, D., Weinl, C., Stierhof, Y.-D. and Hülkamp, M. (2002). Ectopic D-type cyclin expression induces not only DNA replication but also cell division in *Arabidopsis* trichomes. *Proceedings of the National Academy of Sciences* 99, 6410–6415.
- Schwartz, L. M., Smith, S. W., Jones, M. and Osborne, B. A. (1993). Do all programmed cell deaths occur via apoptosis? *Proceedings of the National Academy of Sciences* 90, 980–984.
- Shaw, T. J. and Martin, P. (2009). Wound repair at a glance. *Journal of cell science* 122, 3209–3213.
- Shimomura, O., Johnson, F. H. and Saiga, Y. (1962). Extraction, purification and properties of aequorin, a bioluminescent protein from the luminous hydromedusan, *Aequorea*. *Journal of cellular and comparative physiology* 59, 223–239.
- Skelin, M., Rupnik, M. and Cencic, A. (2010). Pancreatic beta cell lines and their applications in diabetes mellitus research. *Altex* 27, 105–113.
- Skloot, R. (2010). *The immortal life of Henrietta Lacks*. Random House Digital, Inc.
- Spiering, D., Bravo-Cordero, J. J., Moshfegh, Y., Miskolci, V. and Hodgson, L. (2013). Quantitative Ratiometric Imaging of FRET-Biosensors in Living Cells. *Methods in cell biology* 114, 593.
- Stanley, J. C., Dohm, G. L., McManus, B. and Newsholme, E. A. (1984). Activities of glucokinase and hexokinase in mammalian and avian livers. *Biochem. J* 224, 667–671.
- Sun, J., Bird, C. H., Salem, H. H. and Bird, P. (1993). Association of annexin V with mitochondria. *FEBS letters* 329, 79–83.
- Talbot, F. A. (1913). *Practical Cinematography and its Applications*. William Heinemann.
- Tamai, T. K., Young, L. C., Cox, C. A. and Whitmore, D. (2012). Light acts on the zebrafish circadian clock to suppress rhythmic mitosis and cell proliferation. *Journal of Biological Rhythms* 27, 226–236.
- Temple, S. and Raff, M. C. (1986). Clonal analysis of oligodendrocyte development in culture: evidence for a developmental clock that counts cell divisions. *Cell* 44, 773–779.

- Teng, X., Degterev, A., Jagtap, P., Xing, X., Choi, S., Denu, R., Yuan, J. and Cuny, G. D. (2005). Structure–activity relationship study of novel necroptosis inhibitors. *Bioorganic & medicinal chemistry letters* 15, 5039–5044.
- Toimela, T., TÄHTI, H. and YLIKOMI, T. (2008). Comparison of an automated pattern analysis machine vision time-lapse system with traditional endpoint measurements in the analysis of cell growth and cytotoxicity. *ATLA. Alternatives to laboratory animals* 36, 313–325.
- Tomari, Y. and Zamore, P. D. (2005). Perspective: machines for RNAi. *Genes & development* 19, 517–529.
- Topman, G., Sharabani-Yosef, O. and Gefen, A. (2011). A method for quick, low-cost automated confluency measurements. *Microscopy and Microanalysis* 17, 915.
- Traganos, F., Darzynkiewicz, Z., Sharpless, T. and Melamed, M. (1977). Simultaneous staining of ribonucleic and deoxyribonucleic acids in unfixed cells using acridine orange in a flow cytofluorometric system. *Journal of Histochemistry & Cytochemistry* 25, 46–56.
- Trenker, M., Malli, R., Fertschai, I., Levak-Frank, S. and Graier, W. F. (2007). Uncoupling proteins 2 and 3 are fundamental for mitochondrial Ca²⁺ uniport. *Nature cell biology* 9, 445–452.
- Tsien, R. Y. (1998). The green fluorescent protein. *Annual review of biochemistry* 67, 509–544.
- Tsou, P., Zheng, B., Hsu, C.-H., Sasaki, A. T. and Cantley, L. C. (2011). A fluorescent reporter of AMPK activity and cellular energy stress. *Cell metabolism* 13, 476–486.
- Tsujimoto, Y. and Shimizu, S. (2005). Another way to die: autophagic programmed cell death. *Cell Death & Differentiation* 12, 1528–1534.
- Vicente-Manzanares, M. and Horwitz, A. R. (2011). Cell migration: an overview. In *Cell Migration* pp. 1–24. Springer.
- Vishnu, N., Khan, M. J., Karsten, F., Groschner, L. N., Waldeck-Weiermair, M., Rost, R., Hallström, S., Imamura, H., Graier, W. F. and Malli, R. (2013). ATP Increases within the Lumen of the Endoplasmic Reticulum Upon Intracellular Ca²⁺-Release. *Mol. Biol. Cell* 24, mbc–E13.
- Vucicevic, L., Misirkic, M., Kristina, J., Vilimanovich, U., Sudar, E., Isenovic, E., Prica, M., Harhaji-Trajkovic, L., Kravic-Stevovic, T., Vladimir, B. et al. (2011). Compound

C induces protective autophagy in cancer cells through AMPK inhibition-independent blockade of Akt/mTOR pathway. *Autophagy* 7, 40–50.

Wainwright, M. (2010). Dyes, trypanosomiasis and DNA: a historical and critical review. *Biotechnic & Histochemistry* 85, 341–354.

Waldeck-Weiermair, M., Alam, M. R., Khan, M. J., Deak, A. T., Vishnu, N., Karsten, F., Imamura, H., Graier, W. F. and Malli, R. (2012). Spatiotemporal Correlations between Cytosolic and Mitochondrial Ca²⁺ Signals Using a Novel Red-Shifted Mitochondrial Targeted Cameleon. *PloS one* 7, e45917.

Waldeck-Weiermair, M., Deak, A. T., Groschner, L. N., Alam, M. R., Jean-Quartier, C., Malli, R. and Graier, W. F. (2013). Molecularly distinct routes of mitochondrial Ca²⁺ uptake are activated depending on the activity of the sarco/endoplasmic reticulum Ca²⁺ ATPase (SERCA). *Journal of Biological Chemistry* 288, 15367–15379.

Waldeck-Weiermair, M., Jean-Quartier, C., Rost, R., Khan, M., Vishnu, N., Bondarenko, A., Imamura, H., Malli, R. and Graier, W. (2011). The leucine zipper EF hand-containing transmembrane protein 1 (LETM1) and uncoupling proteins-2 and 3 (UCP2/3) contribute to two distinct mitochondrial Ca²⁺ uptake pathways. *J. Biol. Chem.* 286, 28444–28455.

Waldeck-Weiermair, M., Zoratti, C., Osibow, K., Balenga, N., Goessnitzer, E., Waldhoer, M., Malli, R. and Graier, W. (2008). Integrin clustering enables anandamide-induced Ca²⁺ signaling in endothelial cells via GPR55 by protection against CB1-receptor-triggered repression. *J. Cell Sci.* 121, 1704–1717.

Walker, A. F., Marakis, G., Morris, A. P. and Robinson, P. A. (2002). Promising hypotensive effect of hawthorn extract: A randomized double-blind pilot study of mild, essential hypertension. *Phytotherapy Research* 16, 48–54.

Warashina, A. (1999). Light-evoked recovery from wortmannin-induced inhibition of catecholamine secretion and synaptic transmission. *Archives of biochemistry and biophysics* 367, 303–310.

Willer, E. A., Malli, R., Bondarenko, A. I., Zahler, S., Vollmar, A. M., Graier, W. F. and Fürst, R. (2012). The vascular barrier-protecting hawthorn extract WS® 1442 raises endothelial calcium levels by inhibition of SERCA and activation of the IP₃ pathway. *Journal of Molecular and Cellular Cardiology* 53, 567–77.

Williamson, R. (1970). Properties of rapidly labelled deoxyribonucleic acid fragments isolated from the cytoplasm of primary cultures of embryonic mouse liver cells. *Journal of molecular biology* 51, 157–168.

- Wu, C.-S., Wu, P.-H., Fang, A.-H. and Lan, C.-C. (2012). FK506 inhibits the enhancing effects of transforming growth factor (TGF)- β 1 on collagen expression and TGF- β /Smad signalling in keloid fibroblasts: implication for new therapeutic approach. *British Journal of Dermatology* 167, 532–541.
- Wylie, A., Kerr, J. and Currie, A. (1980). Cell death: the significance of apoptosis. *Int. Rev. Cytol* 68, 251–306.
- Yarrow, J. C., Perlman, Z. E., Westwood, N. J. and Mitchison, T. J. (2004). A high-throughput cell migration assay using scratch wound healing, a comparison of image-based readout methods. *BMC biotechnology* 4, 21.
- York, A. G., Chandris, P., Dalle Nogare, D., Head, J., Wawrzusin, P., Fischer, R. S., Chitnis, A. and Shroff, H. (2013). Instant super resolution imaging in live cells and embryos via analog image processing. *Nat. Methods* 10, 1122–1126.
- Zernike, F. (1942). Phase contrast, a new method for the microscopic observation of transparent objects part II. *Physica* 9, 974–986.
- Zernike, F. (1955). How I discovered phase contrast. *Science* 121, 345–349.
- Zhang, S., Cao, Z., Tian, H., Shen, G., Ma, Y., Xie, H., Liu, Y., Zhao, C., Deng, S., Yang, Y. et al. (2011). SKLB1002, a novel potent inhibitor of VEGF receptor 2 signaling, inhibits angiogenesis and tumor growth in vivo. *Clinical Cancer Research* 17, 4439–4450.
- Zhang, T., Du, J., Liu, L., Chen, X., Yang, F. and Jin, Q. (2012). Inhibitory effects and underlying mechanism of 7-hydroxyflavone phosphate ester in HeLa cells. *PloS one* 7, e36652.
- Zicha, D., Dunn, G. A. and Brown, A. F. (1991). A new direct-viewing chemotaxis chamber. *Journal of cell science* 99, 769–775.
- Zigmond, S. H. (1988). [6] Orientation chamber in chemotaxis. *Methods in enzymology* 162, 65–72.

Addendum

Scheme of Experiments

Date	Experiment	System	TP ¹	Figure
Tests				
2011 07 07	first live cell imaging, Histamine effect	NIPKOW	20 sec	F. <i>x</i>
2011 07 18	Staurosporine (apoptosis) vs. H ₂ O ₂ (necrosis)	NIPKOW	min	F. <i>x</i>
2011 07 27	Woundhealing (WH) insert test	NIPKOW	2 min	F. <i>x</i>
2011 07 28	ibidi 8-well slide test	NIPKOW	10 min	
2011 08 17	porcine aortal EC (PAEC) test	NIPKOW	5 min	F. <i>x</i>
2011 08 19	various concentrations of CellTracker Red and Green	NIPKOW	20 min	F. <i>x</i>
2011 08 31	PAA 8-well slide (with WH insert and CellTracker)	NIPKOW	? min	F. <i>x</i>
2011 10 28	WH scratch test	NIPKOW	? min	F. <i>x</i>
2011 11 19	CO ₂ incubator test	NIPKOW	20 sec	F. <i>x</i>
2012 05 30	confluency test 8-well slide	NIPKOW	10 min	F. <i>x</i>
Lipotoxicity				
2011 07 11	BSA [500 μM] vs. PA [500 μM]	NIPKOW	2 min	n.u.
2011 07 12	BSA vs. PA	NIPKOW	2 min	F. <i>x</i>
2011 07 14	BSA vs. PA	NIPKOW	2 min	F. <i>x</i>
2011 07 19	PA ± WM [10 μM] / ± baf [100 nM]	NIPKOW	2 min	F. <i>x</i>
2011 07 30	BSA vs. PA ± WM	NIPKOW	3 min	F. 19
2011 08 01	BSA vs. PA ± WM	NIPKOW	5 min	F. <i>x</i>
2011 08 04	BSA/PA ± WM / ± baf / ± 3-MA	NIPKOW	6 min	F. <i>x</i>
2012 06 23	HeLa cells transfected with NLS-GFP ² , to potentially visualize occurrence of multi-nucleated cells upon treatment with BSA [100 μM], PA [100 μM], OA [100 μM], PA + OA [100 μM] each	CellIQ	min	F. <i>x</i>

¹Timepoint, temporal difference between subsequent images of the image series

²fluorescently labeled DNA

2012 08 02	WH insert, EA cells transfected with siRNA against CYLD and scrambled siRNA as control, BSA [100 μ M], PA [100 μ M], OA [100 μ M], PA + OA [100 μ M] each, PA + OA [200 μ M] each	CellIQ	16.8 min	F. <i>x</i>
2012 09 28	EA cells transfected with siRNA against CYLD, scrambled siRNA, and non-transfected cells, attachment process	NIPKOW	10 min	F. <i>x</i>
2012 09 29	EA cells transfected with siRNA against CYLD, scrambled siRNA, and non-transfected cells, WH insert	NIPKOW	10 min	F. <i>x</i>
2012 10 05	EA cells transfected with siRNA against CYLD, scrambled siRNA, and non-transfected cells, attachment process	NIPKOW	10 min	F. <i>x</i>
2012 10 06	EA cells transfected with siRNA against CYLD, scrambled siRNA, and non-transfected cells, WH insert, BSA [300 μ M], PA [300 μ M]	NIPKOW	10 min	F. <i>x</i>
Wortmannin-induced vacuoles				
2011 08 03	EA cells - FCS, \pm WM [1 μ M]	NIPKOW	2 min	F. 27
2011 11 26	HeLa cells - FCS, \pm WM [10 μ M]	NIPKOW	1 min	F. <i>x</i>
2011 11 27	HeLa cells - FCS, WM [1 μ M] vs. WM [100 nM]	NIPKOW	2 min	F. <i>x</i>
2011 11 29 2011 12 03	HeLa cells + FCS, \pm WM [10 μ M] with control images from cell culture room	NIPKOW, cell culture microscope	1 min	F. <i>x</i>
2011 12 04	EA cells + FCS, \pm WM [10 μ M] with control images from cell culture room	NIPKOW, cell culture microscope	1 min	F. <i>x</i>
2011 12 05	EA cells + FCS, WM [1 μ M] vs. WM [100 nM]	NIPKOW	1 min	F. <i>x</i>
2011 12 10	HUVEC + FCS, \pm WM [10 μ M]	NIPKOW	1 min	F. 26
2011 12 10	EA + FCS, WM [10 μ M] vs \pm WM [1 μ M]	NIPKOW	1 min	F. <i>x</i>
2011 12 11	HUVEC + FCS, \pm WM [10 μ M], with incubator controls	NIPKOW	2 min	F. <i>x</i>
2011 12 16 2011 12 17	HeLa cells - FCS, transfected with (1) D1ER ³ + mtDsRed ⁴ , (2) YFP-LC-3 ⁵ + mtDsRed, (3) cyto-Venus-YFP ⁶ + mtDsRed; to see if origin of membranes WM-induced vacuoles can be determined; images before and after WM [10 μ M] treatment	NIPKOW		F. <i>x</i>

³ER-selective Ca²⁺ FRET-based sensor, here used to show ER structure

⁴mitochondria marker

⁵Microtubule-associated proteins 1A/1B light chain 3A, a marker of autophagic activity

⁶cytosolic marker protein

2011 12 22	HeLa cells -FCS, loaded with Acridine Orange (AO) ⁷ ± WM [10µM]; to see if vacuoles are acidic; sequences with 100x, and 1000x magnification	NIPKOW	30 sec (1000x), 1 min (100x)	F. <i>x</i>
2012 01 10	EA cells 1000x magnification sequence	NIPKOW	30 sec	F. <i>x</i>
2012 01 10	EA cells transfected with mtDsRed and D1ER, ± WM [10µM]	NIPKOW	2 min	F. <i>x</i>
2012 01 11	as 2011 12 22, but with EA cells; 1000x sequence without AO	NIPKOW	5 sec	F. <i>x</i>
2012 01 12	HeLa cells, WM [10µM] and WM [30µM], sequences 50 min, 90 min, and 150 min after WM treatment, respectively.	NIPKOW	1 min (100x), 20 sec (1000x)	F. <i>x</i>
2012 01 17	HeLa cells - FCS, ± WM [10µM]	NIPKOW	20 sec	F. <i>x</i>
2012 01 18	HeLa cells - FCS, + WM [30µM], sparse light	NIPKOW	min	F. <i>x</i>
2012 01 25	EA cells, time-course of light-dependency	NIPKOW	20 sec	F. <i>x</i>
2012 01 26	EA cells, stained with CellTracker Red and MitoTracker Green, or AO, + WM [10µM]	NIPKOW		F. <i>x</i>
2012 01 27	EA cells - FCS, + AO, ± WM [10µM]	cell culture microscope		F. <i>x</i>
2012 03 03	EA cells, ± FCS, ± WM [10µM] or [50µM]	NIPKOW	min	F. <i>x</i>
2012 03 04	EA cells transfected with YFP-LC-3	NIPKOW		F. <i>x</i>
2012 03 05	EA cells, ± FCS, ± WM [10µM]	NIPKOW, cell culture microscope	2 min	F. <i>x</i>
2012 03 08	EA cells, SB202190 compound-induced [5µM] vacuoles	NIPKOW	? min	F. <i>x</i>
2012 03 08	EA cells, vacuole formation comparison between WM [10µM], SB202190 [5µM], and 3-MA [10 mM]	cell culture microscope		F. <i>x</i>
WS 1442				
2011 07 13	WS + Histamine	NIPKOW	2 min	n.u.
2011 07 21	control vs. WS	NIPKOW	2 min	F. <i>x</i>
2011 07 24	[10 µg/ml] vs. [100 µg/ml]	NIPKOW	2 min	F. <i>x</i>
2011 07 25	WS ± WM	NIPKOW	2 min	F. <i>x</i>
2011 12 09	human umbilical vein EC (HUVEC) ± [100 µg/ml]	NIPKOW	1 min	F. <i>x</i>

⁷fluorescent nucleic acid-selective cationic dye, when excited at 502 nm light, it emits 525 nm light (green), permeable, unless in acidic compartments, such as lysosomes, where it becomes protonated and thus sequestered, which changes its spectrum to excitation 460 nm(blue) and emission (orange)

2012 01 12	light-induced toxicity on EA cells	NIPKOW	5 min	F. 28
2012 01 25	as above, \pm WM	NIPKOW	5 min	F. 28
2012 01 28	light-induced toxicity on EA cells	NIPKOW	5 min	F. 28
2012 01 29	light-induced toxicity on HeLa cells	NIPKOW	10 min	F. <i>x</i>
Growth Factors				
2011 10 04	FCS, EGF [30 ng/ml]; influence on cell growth and morphology	NIPKOW	15 min	F. 29
2011 10 06	FCS, VEGF [50 ng/ml], EGF [15 ng/ml], FGF-b [25 ng/ml], IGF-1 [20 ng/ml], VEGF [25 ng/ml] + EGF [5 ng/ml], ECGS [50 ng/ml], control; influence on cell growth and morphology	NIPKOW	15 min	F. <i>x</i>
2011 10 16	FCS, VEGF [100 ng/ml], EGF [30 ng/ml], FGF-b [50 ng/ml], VEGF [30 ng/ml] + EGF [10 ng/ml] + FGF [20 ng/ml], FCS + VEGF [50 ng/ml], FCS + EGF [15 ng/ml]	NIPKOW	15 min	F. 30
Woundhealing				
2011 07 28	\pm FCS	NIPKOW	2 min	F. <i>x</i>
2011 07 31	+ FCS	NIPKOW	2 min	F. <i>x</i>
2011 08 02	\pm AEA [2 μ M]	NIPKOW	2 min	F. <i>x</i>
2011 08 18	various confluencies in WH inserts on ibidi 8-well dish, CellTracker staining	NIPKOW	min	F. <i>x</i>
2011 08 22	\pm AEA [2 μ M]	NIPKOW	10 min	F. <i>x</i>
2011 08 24	ibidi 8-well-dish, \pm FCS, \pm ECGS ⁸ [50 ng/ml], \pm VEGF [50 μ g/ml], each \pm AEA [1 μ M]	NIPKOW	15 min	F. <i>x</i>
2011 08 30	ibidi 8-well-dish, \pm FCS, \pm EGF [5 ng/ml] or [10 ng/ml], each \pm AEA [1 μ M]	NIPKOW	min	F. 23
2011 08 31	PAA 2-well dish, + CellTracker Red and Green	NIPKOW	10 min	F. <i>x</i>
2011 09 11	\pm CellTracker Red and Green	NIPKOW	10 min	F. <i>x</i>
2011 10 05	scratch FCS vs. EGF [30 ng/ml]	NIPKOW	10 min	F. <i>x</i>
2011 10 22	\pm AEA [10 μ M]	NIPKOW	2 min	F. <i>x</i>
2011 10 23	\pm AEA [10 μ M]	NIPKOW	90 sec	F. <i>x</i>
2011 11 15 2011 11 17	\pm LPI [3 μ M]	NIPKOW	4 min	F. <i>x</i>
2012 04 21	light influence on WH (insert)	NIPKOW	10 min	F. 14
2012 04 22	light influence on WH (scratch)	NIPKOW	10 min	F. <i>x</i>
2012 04 23	light influence on WH (insert)	NIPKOW	10 min	F. <i>x</i>

⁸= Endothelial Cell Growth Supplement

2012 04 28	light influence, reduced light, insert	NIPKOW	30 min	F. <i>x</i>
2012 04 29	light influence, reduced light, scratch	NIPKOW	20 min	F. <i>x</i>
2012 05 05	± WM [10 µM], insert	NIPKOW	30 min	F. <i>x</i>
2012 05 06	± WM [10 µM], scratch	NIPKOW	30 min	F. <i>x</i>
2012 05 08 2012 05 12	intense light, ± WM [10 µM], insert	NIPKOW	10 min	F. <i>x</i>
2012 05 23	HUVEC in WH insert	NIPKOW	10 min	F. <i>x</i>
2012 05 24	HUVEC scratch	NIPKOW	10 min	F. <i>x</i>
2012 05 30 2012 05 31	± AEA [10µM] or [1µM]	NIPKOW	10 min	F. <i>x</i>
2012 06 05	± FCS [10 %] and [20%], insert	NIPKOW	10 min	F. <i>x</i>
2012 06 06	± FCS	NIPKOW, scratch	10 min	F. <i>x</i>
2012 06 09	PAA 4-well dish, light effect	NIPKOW	10 min	F. <i>x</i>
2012 06 11	± CellTracker Red [10 µM]	NIPKOW	10 min	F. <i>x</i>
2012 06 16	± CellTracker Red [5 µM]	NIPKOW	10 min	F. <i>x</i>
2012 06 21	BSA [100 µM], PA [100 µM], OA [100 µM], PA + OA [100 µM] each	CellIQ	24 min	F. <i>x</i>
2012 07 26	WH insert and WH scratch, BSA [200 µM], PA [200 µM], OA [200 µM], OA + PA [200 µM each], OA + PA [100 µM each],	CellIQ	19 min	F. <i>x</i>
2012 10 10	PAEC scratch, passage 1 (P1) cells in DMEM	NIPKOW	10 min	F. <i>x</i>
2012 10 17	PAEC scratch, P1 cells vs P2 cells in DMEM	NIPKOW	10 min	F. <i>x</i>
2012 10 24	PAEC scratch, P1 cells vs P3 cells in DMEM	NIPKOW	10 min	F. <i>x</i>
2012 11 15	insert, EA cells transfected with siRNA against MICU1 and control siRNA	NIPKOW	10 min	F. 42
2012 11 25	scratch, EA cells transfected with siRNA against MICU1 and control siRNA	NIPKOW	30 min	F. 42
2012 12 01	PAEC scratch, P1 cells in DMEM or MEM	NIPKOW	30 min	F. 34
2012 12 02	scratch, EA cells transfected with siRNA against MICU1 and control siRNA	NIPKOW	30 min	F. <i>x</i>
2012 11 25	scratch, EA cells transfected with siRNA against MICU1 and control siRNA	NIPKOW	30 min	F. <i>x</i>
2012 12 05	PAEC scratch, P1 cells vs P2 cells in DMEM or MEM	NIPKOW	30 min	F. <i>x</i>
2012 12 12	PAEC scratch, P1 cells vs P3 cells in DMEM or MEM	NIPKOW	30 min	F. <i>x</i>
2012 12 14	scratch, EA cells transfected with siRNA against MICU1 and control siRNA	NIPKOW	30 min	F. 42

2012 12 15	insert, EA cells transfected with siRNA against MICU1 and control siRNA	NIPKOW	30 min	F. 42
Nanoparticles				
2012 07 03	EA cells, NP ⁹ [250 µg/ml], [125 µg/ml], [62.5 µg/ml], [31.25 µg/ml], each ± FCS	CellIQ	12.2 min	F. <i>x</i>
2012 07 07	EA cells, control, NP [250 µg/ml], [125 µg/ml], [50 µg/ml], each ± FCS, ± GFP (505 nm) excitation	CellIQ	5.8 min	F. <i>x</i>
2012 07 09	WH insert, control, NP [250 µg/ml], [125 µg/ml], ± GFP excitation	CellIQ	11.6 min	F. <i>x</i>
2012 07 10	HeLa cells, control, NP [250 µg/ml], [125 µg/ml], [50 µg/ml], each ± FCS, ± GFP excitation	CellIQ	42.8 min	F. <i>x</i>
2012 07 11	EA cells, control, NP [125 µg/ml], ± WM [1 µM], to see if NP are internalized into WM-induced vacuoles	NIPKOW	20 min	F. <i>x</i>
2012 07 17	WH insert, ± non-flourescent NP [250 µg/ml], ± GFP excitation	CellIQ	31 min	F. <i>x</i>
Serum and Nutrient Deprivation				
2012 07 14	EA, HeLa, INS cells, effect of nutrient starvation (± Glucose, ± Galactose), each ± WM [1 µM], ± FCS	CellIQ	118 min	F. 35
2012 07 19	EA, HeLa, INS cells, ± Glucose, - FCS	CellIQ	min	F. 37
2012 07 29	HeLa cells, ± Glucose, - FCS, medium change at 6 hours, 8 h, 10 h, 12 h, 14 h, or 16 h to Glucose-containing medium	CellIQ	42.6 min	F. 38
2012 10 30	EA cells, EA cells in WH insert, ± FCS, ± Glucose, medium change at 6 h, 7 h, 8h, 9h to Glucose- and FCS-containing medium	CellIQ	5.2 min	F. 32
2012 12 17	HeLa transfected with ER AT1.03, proliferation assay of serum-starved cells vs control	NIPKOW	15 min	F. <i>x</i>
2013 01 13	HeLa transfected with ER AT1.03, proliferation assay of serum-starved cells vs control	CellIQ	15 min	F. <i>x</i>
2013 01 16	non-transfected HeLa, proliferation assay of serum-starved cells vs control	CellIQ	20 min	F. 31
2013 01 26	non-transfected HeLa, proliferation assay of serum-starved cells vs control	CellIQ	20 min	F. 31
2013 02 16	Tebu HeLa with stable MCU knockdown vs Tebu control HeLa, proliferation assay	CellIQ	30 min	F. 39, 40

⁹FlouSpheres[©] carboxylate, 0.04 µm, yellow-green (505/515), azide-free

2013 02 21	HeLa cells, full medium vs loading buffer vs experiment buffer	CellIQ	30 min	F. 12, 49
2013 02 28	two HeLa cell strains, loading buffer \pm glucose	CellIQ	30 min	F. 46
2013 03 07	EA cells, WH with 0%, 5%, 10%, 20% FCS	CellIQ	30 min	F. 32
2013 03 17	HeLa cells, \pm Glucose, Control vs Compound C vs AICAR vs STO-609	CellIQ	30 min	F. 47
2013 03 21	HeLa cells, \pm FCS, \pm Glucose, Control vs Compound C vs AICAR vs STO-609	CellIQ	30 min	F. <i>x</i>
2013 04 15	freshly split vs previously split HeLa cells	CellIQ	30 min	F. 44
Confluency Measurement				
2012 10 24	HeLa cells transfected with ER-ATP, D1-ER, or D3-cpv, plated with various concentrations to reach various confluencies, to estimate confluency and cell number in each well	NIPKOW		F. ??
2013 01 23	Tebu HeLa with stable MCU knockdown vs Tebu control HeLa, proliferation assay	CellIQ	30 min	F. <i>x</i>
2013 06 28	Tebu HeLa with stable MCU knockdown vs Tebu HeLa with stable ANXA IV knockdown vs Tebu control HeLa, Control vs siMICU1 vs UCP3 overexpression vs siMICU1 + UCP3 oe, proliferation assay	CellIQ	30 min	F. 43
Viability assays				
2012 11 20	HeLa siRNA against MICU1 vs control, apoptosis induced with C2-Ceramide [40 μ M] or staurosporine [100 nM] or [200 nM]	MTT assay		F. 41
2013 02 14	Tebu HeLa with stable MCU knockdown vs Tebu control HeLa, C2-Ceramide [40 μ M] to induce apoptosis vs control (1 μ l DMSO)	CellIQ	30 min	F. <i>x</i>
2013 02 16	Tebu HeLa with stable MCU knockdown vs Tebu control HeLa, C2-Ceramide [40 μ M] to induce apoptosis vs control (1 μ l DMSO)	CellIQ	30 min	F. 39
2013 03 09	Tebu HeLa with stable MCU knockdown vs Tebu control HeLa, apoptosis induced with C2-Ceramide [40 μ M]	MTT assay		F. 39
Ca²⁺ and ATP measurements				
2012 03 15	INS cells transfected with D1-GO ¹⁰ or D3-cpv ¹¹ , to compare the characteristics of both sensors	NIPKOW	1 sec	F. <i>x</i>
2012 03 16	as above	iTill	1 sec	F. <i>x</i>

¹⁰FRET = Förster resonance energy Ca²⁺ sensor with GFP as donor and OFP as acceptor

¹¹FRET Ca²⁺ sensor with CFP as donor and YFP as acceptor

2012 03 21	as above	iTill	1 sec	F. <i>x</i>
2012 03 30	as above	NIPKOW	1 sec	F. <i>x</i>
2012 07 06	EA cells, Fura-2 measurement, \pm NP [500 μ g/ml], [250 μ g/ml], [50 μ g/ml]	old NIP-KOW	1 sec	F. <i>x</i>
2012 07 20	EA cells, Fura-2 measurement, \pm non-flourescent NP [500 μ g/ml]	old NIP-KOW	1 sec	F. <i>x</i>
2012 07 25	EA cells transfected with mtDsRed or ER-RFP, \pm NP [250 μ g/ml], flou-4 measurement	old NIP-KOW	1 sec	F. <i>x</i>
2013 01 28	INS cells transfected with ER AT1.03 or D1ER, upon Carbachol / ATP stimulation	Rig 4	3 s	F. <i>x</i>
2013 01 30	INS cells transfected with ER AT1.03 and plant ANT1-mCherry or mtDsRed, upon ionomycin stimulation	Rig 4	3 s	F. <i>x</i>
2013 02 14	two HeLa cell strains, both transfected with ER AT1.03 or D1ER, upon ionomycin stimulation	Rig 4	3 s	F. <i>x</i>
2013 02 15	two HeLa cell strains, both transfected with ER AT1.03 or D1ER, upon ionomycin stimulation	Rig 4	3 s	F. <i>x</i>
2013 02 18	HeLa cells, transfected with ER AT1.03 or D1ER, upon ionomycin stimulation, pre-incubated in loading buffer or FM	Rig 4	3 s	F. 49
2013 02 21	as above, \pm FCS	Rig 4	3 s	F. 49
2013 02 22	as above, with varied confluency	Rig 4	3 s	F. <i>x</i>
2013 03 01	as above, pre-incubated \pm glucose	Rig 4	3 s	F. 46
2013 03 05	HeLa cells, ER AT1.03, freshly split vs previously split, pre-incubated \pm glucose	Rig 4	3 s	F. 44
2013 03 07	HeLa cells, ER AT1.03, freshly split vs previously split, pre-incubated \pm FCS	Rig 4	3 s	F. <i>x</i>
2013 03 07	HeLa cells, ER AT1.03 or D1ER, freshly split, pre-incubated \pm glucose, \pm Compound C	Rig 4	3 s	F. 44
2013 03 12	HeLa cells, ER AT1.03, pre-incubated \pm glucose, \pm Compound C for 20 min - 8 h	Rig 4	3 s	F. 47
2013 03 12	INS-1 cells, ER AT1.03, \pm Compound C in 10 mM glucose	Rig 4	3 s	F. <i>x</i>
2013 03 14	HeLa cells, ER AT1.03, \pm siAMPK	Rig 4	3 s	F. 48
2013 03 15	HeLa cells, ER AT1.03 or D1ER, \pm glucose, \pm 3-MA	Rig 4	3 s	F. 46
2013 03 19	HeLa cells, ER AT1.03 or D1ER, pre-incubated \pm glucose	Rig 4	3 s	F. 46
2013 03 21	HeLa cells, ER AT1.03 or D1ER, \pm STO-609	Rig 4	3 s	F. <i>x</i>

2013 03 28	INS-1 cells, ER AT1.03 or D1ER, \pm Compound C, \pm 3-MA	Rig 4	3 s	F. <i>x</i>
2013 03 29	HeLa cells, AMPKAR, activation of AMPK by glucose withdrawal or Ca^{2+} stimulation	Rig 4	3 s	F. 48
2013 03 30	HeLa cells, AMPKAR or ER AT1.03, Control vs Compound C vs STO-609	Rig 4	3 s	F. 47
2013 05 01	HeLa cells, ER AT1.03 or D1ER, \pm glucose, \pm bafilomycin A	Rig 4	3 s	F. 46
2013 05 04	HeLa cells, ER AT1.03 or AMPKAR, \pm siAMPK, \pm glucose	Rig 4	3 s	F. 48
2013 05 06	HeLa cells, AMPKAR or 4mtD3cpv, \pm glucose	Rig 4	3 s	F. 48
2013 05 08	HeLa cells, AMPKAR, switch from buffer with glucose to buffer \pm glucose	Rig 4	3 s	F. 48
2013 05 15	HeLa cells, AMPKAR or 4mtD3cpv, \pm siAMPK, \pm glucose	Rig 4	3 s	F. <i>x</i>
2013 05 16	C8 cells, \pm glucose	Rig 4	3 s	F. <i>x</i>
2013 05 17	HeLa cells, 4mtAT1.03 or 4mtD3cpv, \pm siAMPK, \pm glucose	Rig 4	3 s	F. 46
2013 05 18	HeLa cells, ER AT1.03, \pm glucose, \pm 2-DG	Rig 4	3 s	F. 46
2013 05 28	C8 cells, \pm glucose	Rig 4	3 s	F. <i>x</i>
2013 05 30	HeLa cells, \pm siAMPK, \pm glucose, Fura-2 measurement	Rig 4	3 s	F. <i>x</i>
2013 06 05	HeLa cells, \pm siAMPK, pre-loaded with TMRM to measure mitochondrial membrane potential	Rig 4	3 s	F. <i>x</i>
2013 06 06	HeLa cells, pre-loaded with JC-1 \pm glucose, Fura-2 measurement	Rig 2	3 s	F. <i>x</i>
2013 06 11	HeLa cells, 4mtD1GO, pre-loaded with Fura-2, \pm glucose	iTill	2 s	F. <i>x</i>

Publications

1. Vishnu, N., Khan, M. J., **Karsten, F.**^{*}, Groschner, L. N., Waldeck-Weiermair, M., Rost, R., Hallström, S., Imamura, H., Graier, W. F., Malli, R. (2013). *ATP Increases within the Lumen of the Endoplasmic Reticulum Upon Intracellular Ca²⁺-Release*. Mol. Biol. Cell. *In press*.

^{*} contributed equally with first author

2. Waldeck-Weiermair, M., Alam, M. R., Khan, M. J., Deak, A. T., Vishnu, N., **Karsten, F.**, Imamura, H., Graier, W. F., Malli, R. (2012). *Spatiotemporal Correlations between Cytosolic and Mitochondrial Ca²⁺ Signals Using a Novel Red-Shifted Mitochondrial Targeted Cameleon*. PLoS One 7(9):e45917.

3. Khan, M. J., Alam, M. R., Waldeck-Weiermair, M., **Karsten, F.**, Groschner, L. N., Riederer, M., Hallström, S., Rockenfeller, P., Konya, V., Heinemann, A., Madeo, F., Graier, W. F., Malli, R. (2012). *Inhibition of Autophagy Rescues Palmitic Acid-induced Necroptosis of Endothelial Cells*. J. Biol. Chem. 287(25):21110-20.

Presentations

1. **Plenary Presentation** at the 1st International Student Congress at the Medical University of Graz on July, 6, 2013. Title: *Cancer Cells Exhibit Distinct Subcellular ATP Pools Depending on their Proliferation Rate*.

2. **Poster Presentation** at the Gordon Research Conference: Calcium Signaling in June 2013. Title: *Development of a Novel Red-Shifted Mitochondrial-targeted Cameleon to Measure Cytosolic and Mitochondrial Ca²⁺ Signals Simultaneously*.

Prize

Best Plenary Presentation at the 1st International Student Congress at the Medical University of Graz on July, 6, 2013.